Harvesting Energy from Non-ideal Vibrations

by

Samuel C. Chang

B.S., National Taiwan University (2007)
S.M., Massachusetts Institute of Technology (2010)

Submitted to the Department of Electrical Engineering and Computer Science
in partial fulfillment of the requirements for the degree of

Doctor of Philosophy in Electrical Engineering and Computer Science

at the

MASSACHUSETTS INSTITUTE OF TECHNOLOGY

June 2013

Author .....
Department of Electrical Engineering and Computer Science
May 20, 2013

Certified by .....
Jeffrey H. Lang
Professor of Electrical Engineering and Computer Science
Thesis Supervisor

Accepted by .....
Leslie Kolodziejski
Chairman, Department Committee on Graduate Students

Harvesting Energy from Non-ideal Vibrations

by

Samuel C. Chang

Submitted to the Department of Electrical Engineering and Computer Science
on May 20, 2013, in partial fulfillment of the
requirements for the degree of
Doctor of Philosophy in Electrical Engineering and Computer Science

Abstract

Energy harvesting has drawn significant interest for its potential to power autonomous low-power applications. Vibration energy harvesting is particularly well suited to industrial condition sensing, environmental monitoring and household environments where low-level vibrations are commonly found. While significant progress has been made in making vibration harvesters more efficient, most designs are still based on a single constant vibration frequency. However, most vibration sources do not have a constant frequency nor a single harmonic. Therefore, the inability to deal with non-ideal vibration sources has become a major technological obstacle for vibration energy harvesters to be widely applicable.

To advance the state of vibration energy harvesting, this thesis presents a design methodology that is capable of dealing with two major non-ideal vibration characteristics: single harmonic frequency shifting and multi-frequency/broadband excitation. This methodology includes a broad-band impedance matching theory and a power electronics architecture to implement that theory.

The generalized impedance matching theory extends the well known single frequency impedance matching model to a multi-frequency impedance matching model. By connecting LC tank circuits to the harvester output, additional resonant frequencies are created thereby enabling the energy harvesting system to effectively harvest energy from multi-harmonic vibration sources. However, the required inductors in the LC tank circuits are often too large (>10 H) to be implemented with discrete components. The power electronics proposed here addresses this issue by synthesizing the tank circuits with a power factor correction (PFC) circuit. This circuit mainly consists of an H-bridge, which contains four FETs, and a control loop that turns the FETs on and off at the right time such that the load voltage and current display the characteristics of the multiple tank circuits. By using this proposed power electronics, we demonstrate dual-frequency energy harvesting from a single mechanically resonant harvester. Simulation and experimental results match well and demonstrate that the proposed power electronics is capable of implementing higher order multi-resonant energy harvesting systems.

In conclusion, this thesis presents both a theoretical foundation and a power elec-

tronics architecture that enables simultaneous effective multi-frequency energy harvesting with a single mechanically resonant harvester. The tunability of the power electronics also provides the possibility of dynamic real-time tuning which is useful to track non-stationary vibration sources.

Thesis Supervisor: Jeffrey H. Lang
Title: Professor of Electrical Engineering and Computer Science

Acknowledgments

This thesis was supported by the following four funding sources: the Air Force Research Laboratory as part of the DARPA HI-MEMS Program under Contract FA8650-07-C-7704, the Schlumberger-Doll Research Center through the MIT Energy Initiative, the MIT Teaching Assistant financial support and last but not least, the MIT EECS bridge fund. This thesis would not have been able to be finished without the timely support of these funds, and for that, I am truly grateful and forever in debt.

I would first like to thank my thesis committee members Prof. Anantha Chandrakasan, Prof. David Perreault and Dr. Dennis Buss. Thank you all for spending time in giving me valuable insights into low power integrated circuits, power electronics and harvester physics. I would especially like to thank Dr. Dennis Buss for his persisting effort in understanding the fundamental physics of piezoelectric harvesters. His passion and insightful suggestions really solidified the fundamentals of this thesis.

Second, I would like to thank my collaborators Dr. Jahir Pabon and Dr. Murat Ocalan at Schlumberger-Doll Research. Their backgrounds in mechanical engineering really complimented this interdiscipline thesis of electrical and mechanical engineering. The one year collaboration helped move the research in light-speed compared to before. I would especially like to thank Dr. Jahir Pabon for going above and beyond his duties of helping me extend funding support for another six months. I am truly grateful.

I also owe a huge intellectual debt to numerous individuals working at the Laboratory for Electronic and Electromagnetic Systems for their help during the development of this thesis. Wei Li, Jiankang Wang, David Giuliano, Uzoma Orji, Seoungbum Lim, Matthew D'Assaro, Wardah Inam, Samantha Gunter, Mohammad Araghchini, Stephen Hou and Richard Zhang provided unwavering support whenever I ran into difficulties and above all, make LEES a fun place to work.

Without my buddies at MIT, life would be completely different. Thank you Albert for being like a brother to me and giving me honest advices which really helped me become a better person. And, of course having tons of fun hanging out and doing

stupid things. Thank you Wilt and Kunle for both being awesome roommates, great listeners and supporting me when I needed you guys the most. Thank you Jen Lee, Jackie Lee, VGOD Chang and Kay Hsi for making my life at MIT so much more colorful. I especially like to thank the Chou and Tsao family for helping me get acclaimed to Boston when I first arrived and welcoming me to your homes. Even though they were short meetings, they truly helped me find Boston as a home and helped me through my first year at MIT. I would also like to thank Patrick Lin and his family and Cherilyn Hu and her family from church for being my mentor and opening your home to me. Thank you Patrick and Auntie Cherilyn! Last, I would like to thank Jingjing for being there for me and being ultra-supportive throughout the writing of this thesis. Thank you dear.

I would also like to thank Prof. Chenming Hu, Prof. Philip Wong, Prof. Liang-Gee Chen and Dr. Chih-chi Cheng for their guidance and support throughout my undergraduate and graduate years. Thank you Prof. Hu for enlightening me the value of a graduate education and the important things in life. I still remember to this day of your encouragement to me of not trying to catch the next big wave but to truly become a expert in a field I am passionate about. Thank you Prof. Hu. I would like to thank Prof. Wong for always being super encouraging during my summer internship at Stanford. That summer really taught me the ability to do independent research and solve problems which no one has solved before. This gave me the confidence and passion of doing more research and earning a Ph.D. degree. I would like to thank Prof. Liang-Gee Chen for guiding me throughout my undergraduate years at NTU and encouraging me to study abroad. Your selfless encouragements and insightful suggestions truly shaped how I think as a researcher and as a person today. Last but not least, I would like to thank Dr. Chih-chi Cheng for being my mentor from NTU to MIT. Your strive for excellence continues to inspire me to this day. Thank you for answering all my naive questions on IC design throughout the years. For all of this, I truly thank all of you.

My parents, Peter and Carol Chang, provided much guidance and moral support during my educational career and allowed me to reach where I am today. Their care

and understanding go way beyond the norm, and I am forever grateful. Your prayers gave me strength and helped me overcome all the challenges at school and in life. This thesis belongs to them as much as it does to me. I would also like to thank my brother Michael Chang for opening his home whenever I felt burned out and giving me timely career suggestions when I needed them the most. If not for him, I would never have been able to come to MIT. Thanks Mike!

Professor Jeffrey Lang deserves my deepest gratitude. Throughout this research, he provided countless suggestions for overcoming difficult theoretical and experimental barriers. Without these critical insights, this thesis would not exist. I will never forget all the time he spent with me both during and after research meetings, even when he already had many other businesses to attend to. Furthermore, he never hesitated to remind me to rest when I had exams in the courses I was taking. Thank you so much for being patient when progresses were slow and above all, for being a great role model for me in research and in life. I cannot possibly repay all your kindness and care. Thank you Professor Lang.

Last, I would like to thank God for everything. If it was not the miracle that gave me birth and the protection and guidance throughout my life, I would not have any of these things in my life. Thank you Lord.

Contents

List of Figures

List of Tables

Chapter 1

Introduction

Energy harvesting is the conversion of ambient energy into usable electrical energy. For centuries, it has been widely applied in the form of wind and water mills, turbine generators, and recently, in solar and wind power plants. More recently, micro-scale energy harvesting systems (10 μW - 10 mW) have garnered significant research interest due to the rapid development of CMOS technology and the advent of distributed low-power applications.

Over the past few decades, CMOS technology has continuously scaled according to Moore's law, which predicts that the number of transistors on integrated circuits (IC) doubles approximately every two years. In addition, with the demanding need from hand-held power and wireless sensor applications, ultra-low-power (ULP) ICs have burgeoned over the past few years. For the first time, the electric power generated by micro-scale energy harvesters seems adequate to power ULP circuits and wireless sensors.

Micro-scale energy harvesting scavenges energy from ambient sources such as sunlight, heat, vibration, etc. These energy sources become increasingly important in environments where battery replacement cannot be easily achieved, e.g. the Alaskan oil pipline [8] and tire pressure sensors. While solar power is the most widely available source of energy, many industrial and wireless sensor applications are not situated in environments where sufficient sunlight or high intensity lighting is available. For the applications mentioned above, the presence of ambient vibrations makes it possible

to scavenge mechanical energy. Some other applications for vibration energy harvesting include wave power harvesting[1] and moth flight control system powering [3]. In summary, its minimal maintenance characteristic and ability to be employed in hostile and inaccessible environments makes vibration energy a highly attractive power source.

In most environments, the vibration acceleration can be as low as 1 $m \cdot s^{-2}$ and the vibration frequency could be single digit Hz to 100's of Hz such as the 60-120 Hz vibration of machines. These low vibration levels equate to vibration amplitudes that are on the order of a few microns and the most common way to convert this kinetic energy is to use an inertial generator that resonates with the vibration frequency. Three energy conversion mechanisms, often coupled with resonators, are commonly pursued for vibration energy harvesting applications: electromagnetic [9, 10, 11], piezoelectric [8, 12, 13, 14] and electrostatic [4, 15, 16].

Over the past few years, while many researchers have implemented various techniques to harvest vibration energy efficiently and effectively, most designs have been high quality factor systems based on a single resonance frequency. From a spectrum point of view, most harvesters are thereby only suitable for single harmonic, fixed vibration frequency applications. However, most ambient vibration sources often display mutli-harmonic and frequency shifting characteristics, such as the window vibration example shown in Figure 1-1. While, multi-harmonic vibrations does not interfere with the power extraction for single resonance harvesters, it does present a significant amount of untapped vibration energy. Vibration frequency shifting on the other hand, will completely neutralize the harvesters' ability to extract energy if the vibration frequency moves beyond the harvesters resonant bandwidth. The non-ideal vibration characteristic and untapped potential of multi-frequency energy extraction have become major technological obstacles for vibration energy harvesters to generate sufficient energy and hence to be widely applicable in powering wireless systems for daily use. This thesis will address both issues by building accurate mathematical models, developing new control algorithms and implementing these algorithms in

[1] www.pelamiswave.com/

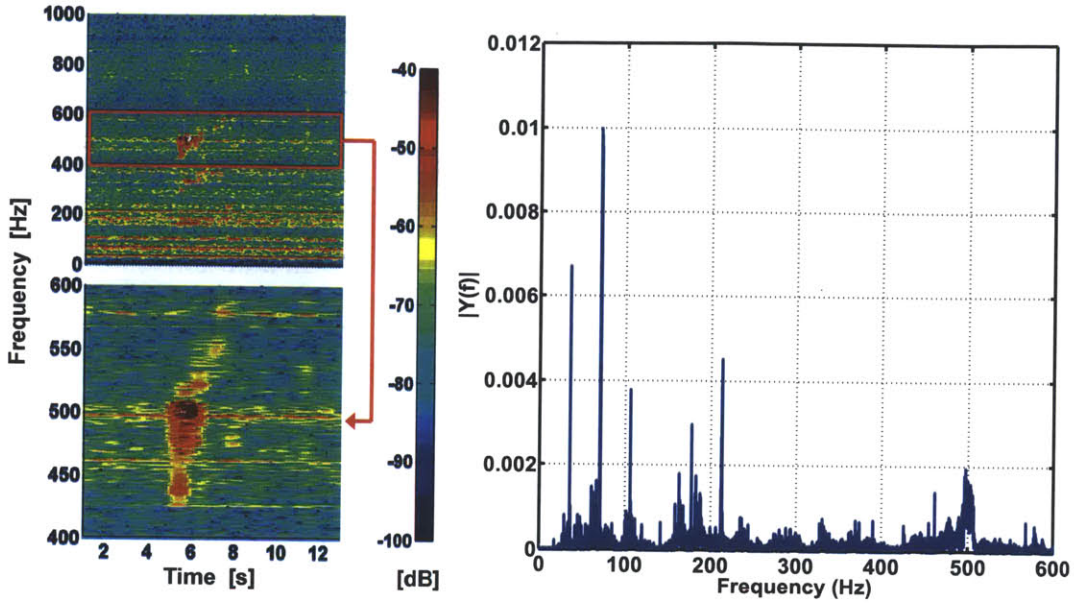

(a) (b)

Figure 1-1: Non-ideal vibration conditions recorded off of an office window: (a) Spectrogram, and (b) Fourier transform of the window vibration.

power electronics.

1.1 Thesis Objective and Contributions

The objective of this research is to enhance the energy scavenging capabilities of today's vibration energy harvesters with tunable electrical loads synthesized with power electronics. The issue of multi-harmonic vibrations and moving vibration frequencies are specifically addressed. While, the idea of tuning the resonant frequency of energy harvesters with reactive electrical loads, namely inductors and capacitors, is well known [17], the research conducted in this thesis is the first to propose the idea of multi-frequency harvesting and demonstrate it both theoretically and experimentally [18].

In the process of achieving mutli-frequency vibration harvesting, two major research breakthroughs are made. First, a complete theoretical analysis of optimal multi-frequency energy harvesting is developed. It considers the electromechanical dynamics and the electrical load design methodology for harvesting energy from multi-

frequency vibrations. Second, a power electronics framework based on power factor correction circuits [19, 20] is built to synthesize the required complex electrical load impedances. The need to synthesize the load impedance with power electronics is because these complex load impedances often included large reactive components that are too energy inefficient, if built with passive components. In addition, these passive reactive components are not tunable which as a result takes out the dynamic tunability of the energy harvesting system. To demonstrate the idea, a printed circuit board that enables dual-frequency harvesting from a single resonance piezoelectric harvester is designed, fabricated, and tested. The framework could be expanded to electromagnetic and electrostatic harvesters and be used for multi-frequency harvesting beyond two frequencies.

1.2 Thesis Organization

This chapter served both as an introduction to the world of energy harvesting as well as an overview of this thesis. The major technical challenges for vibration energy harvesting include increasing the extracted power from the ambient vibration source such and dealing with non-ideal vibration characteristics such as frequency shifts. This thesis addresses these two challenges by electrically tuning the harvester with power electronics. Both a theoretical model and a experimental demonstration is developed in the process.

The road map of this thesis starts with an introduction to the previous research conducted in the area of vibration energy harvesting and to the state of the art methods of dealing with non-ideal vibrations. These are illustrated in Chapter 2. In Chapter 3, the theoretical model for harvester electrical loading is thoroughly discussed. The theory begins with single resonant frequency tuning and gradually expands to N-frequency energy harvesting. Chapter 4 outlines the design and simulation of the power electronics framework used to synthesize the required electrical load. A thorough efficiency evaluation and benefits of IC integration is also explored. Chapter 5 gives the details of the shaker table calibration, automated data collection

setup and piezoelectric harvester characterization. Experimental demonstrations of the power electronics is shown in Chapter 6. The experimental results are compared with the SPICE and MATLAB simulations and the experimental errors are investigated. Finally, Chapter 7 summarizes the thesis and its conclusions, and presents possible direction of future work in this area of research.

Chapter 2

Background

In the past decade, significant research results have been made on vibration energy harvesting. This section will serve as a background introduction to these important work that have been done by other researchers in this area. The chapter begins with a general introduction to energy harvesting and why vibration energy harvesting specifically has garnered significant research interest. Next, the three major vibration energy harvesting methods - electromagnetic, electrostatic and piezoelectric are introduced. In the final part of this chapter, we shift our focus to the previous work done on addressing the issue of harvesting energy from non-ideal vibrations and harvester interface circuits.

2.1 Energy Harvesting

Over the past few decades, CMOS technology has continuously scaled following Moore's Law, which observed that over the history of computing hardware, the number of transistors on integrated circuits doubles approximately every two years. The continued scaling of transistors has also made integrated circuits more energy efficient in performing the same task. Ultra-low power microprocessors such as the MSP430[1] developed by Texas Instruments consumes less than 1μW of power during standby mode. These and other ultra-low power chips enabled the rapid development

[1] www.ti.com/msp430

Table 2.1: Comparison of power scavenging and energy sources [1]

	1-year Power Density ($\mu W/cm^3$)	10-year Power Density ($\mu W/cm^3$)
Solar (Outdoors)	15,000 (Sunny)	15,000 (Sunny)
	150 (Cloudy)	150 (Cloudy)
Solar (Indoors)	6 (Office)	6 (Office)
Vibration (Piezoelectric)	250	250
Vibration (Electrostatic)	50	50
Acoustic Noise	0.003 (75 dB)	0.003 (75 dB)
	0.96 (100 dB)	0.96 (100 dB)
Temperature Gradient	15 (10°C Gradient)	15 (10°C Gradient)
Shoe Inserts	330	330
Batteries (Non-rechargeable Lithium)	45	3.5
Batteries (Rechargeable Lithium)	7	0
Hydrocarbon Fuel (Micro Heat Engine)	333	33
Fuel Cells (Methanol)	280	28

of hand-held products and wireless sensors.

While integrated circuits have advanced rapidly in the 30 years, the development in battery technology has not seen similar progress. As a consequence, the power source has become a major technology bottleneck for wireless sensors and hand-held devices. In addition, batteries have a limited lifetime and must be replaced periodically. Replacing batteries in large terrains such as the Alaskan oil pipeline or inaccessible environments such as oil well drills can be even more costly. Therefore, researchers began investigating the possibility of creating a device that can harvest ambient energy directly from the environment and eliminate the need for a battery. Possible ambient energy sources which researchers looked into include solar, thermal, vibration, etc. A broad survey of these potential energy sources is shown in Table 2.1 [1]. The data shows that for short lifetimes, batteries are a reasonable solution. However, for longer lifetimes, harvesting energy from the environment becomes more attractive. According to Roundy's estimation, the power density of a piezoelectric based energy harvester is approximately 250 $\mu W/cm^3$, only second to solar power which is 15,000 $\mu W/cm^3$. In environments where sunlight or intense indoor lighting is not available, vibration energy harvesting can be the most attractive option. A more careful comparison of vibration energy conversion to solar power and battery power is shown in Figure 2-1.

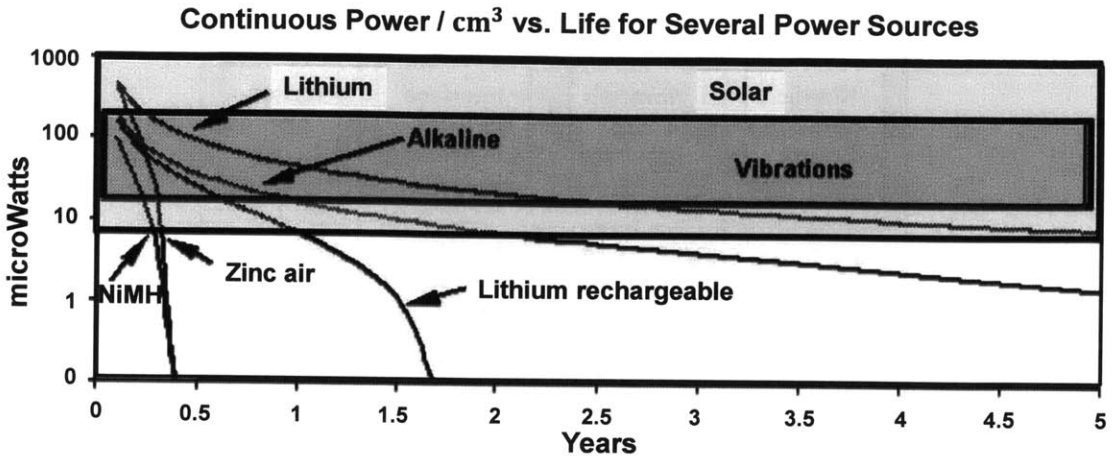

Figure 2-1: Comparison of power from vibrations, solar, and various battery chemistries [1].

The gray boxes represent the lifetime and power range of solar power and vibration based power generation. From Figure 2-1, it can be observed that if the projected lifetime of the sensor node is only a few years, batteries are the obvious choice of power. If adequate light energy is available in the environment in which the node will operate, solar cells offer an attractive solution. However, if the projected lifetime of the sensor is more than a few years or sufficient light energy is not available, vibration energy conversion becomes a strong candidate. As mentioned in Chapter 1, low level mechanical vibrations are available in many environments, and therefore have a potentially wider application domain than some of the sources listed in Table 2.1.

2.2 Harvester Mechanical Structure

Vibration energy harvesting involves the creation of a physical structure that can couple to kinetic energy from small vibrations and convert it into storable electric energy. Due to the growing demand of autonomous sensors that must function without the need for human intervention, interest in this topic has burgeoned in recent years. Applications on the market today include shaker flashlights, ocean wave energy har-

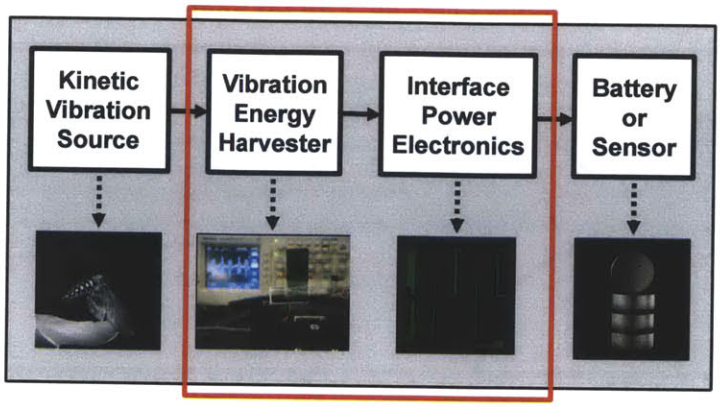

Figure 2-2: Energy flow from the vibration source via the energy harvesting system delivered to the end application. The vibration energy harvesting system is highlighted in the red box.

vesting buoys, wireless sensor node energy harvesters[2], etc. These applications can be categorized by the mechanical structure or the energy conversion mechanism. In this section, we will introduce the two kinds of mechanical structures often found in today's energy harvesters. The next section will then look into the three kinds of harvester energy conversion methods.

A vibration energy harvester is a two-port (electrical and mechanical) device and the mechanical port has two terminals. It is the relative motion of the two terminals against the force of the internal energy converter that converts energy. As shown in Figure 2-3, there are two ways to connect the terminals and force relative motion - the proof mass structure and the strain-coupled structure. For both structures, we use vibration harvesters that harvest energy from wave power. The decision on which of the two structures to use depends on whether the vibration source offers both mechanical terminals of a relative strains source or not. If not, the proof mass structure is used to provide the second terminal of the source. In reality, the proof mass structure is the more common structure found in vibration harvesters since most harvesters scavenge energy from flat surfaces and hence require an additional proof mass to convert the energy. As a note, the piezoelectric harvester used in this thesis also has a proof mass structure.

[2]www.perpetuum.com

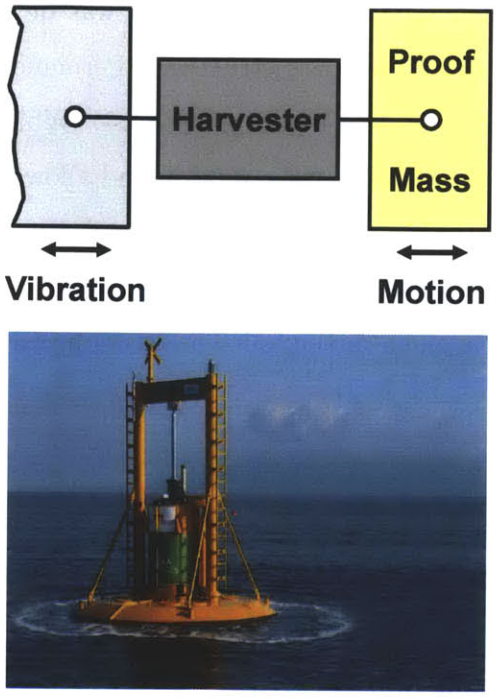

(a)

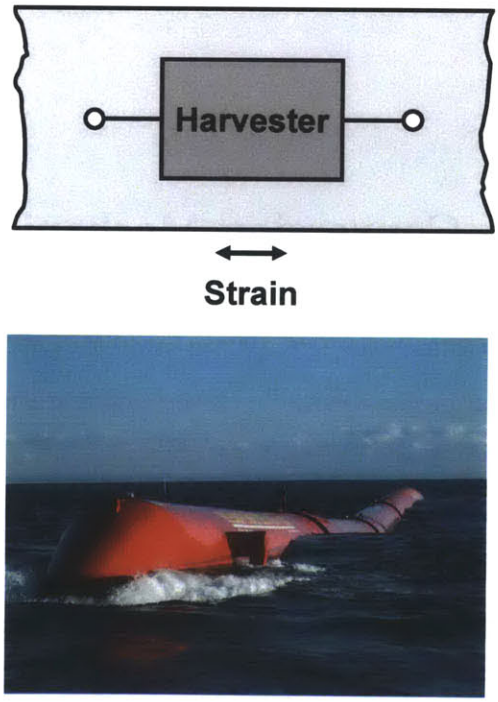

(b)

Figure 2-3: Two kinds of mechanical structure for vibration energy harvesters: (a) the proof mass structure, and (b) the strain-coupled structure.

The harvester example shown in Figure 2-3(a) was developed by Ocean Power Technologies[3] and uses the proof mass structure. Permanent magnets are built on a spring inside the barrel and acts like a proof mass. While the wave goes up and down, the spring resonates with the wave motion and allows the permanent magnets to move across coil wires inside the harvester. The relative motion between the coil and magnet generates electrical power. More details on this electromagnetic energy conversion phenomenon is given in the following section.

The Pelamis machine, as shown in Figure 2-3(b), is developed by Pelamis Wave Power[4]. It is made up of five tube sections linked by universal joints which allow flexing in two directions. The machine floats semi-submerged on the surface of the water and inherently faces into the direction of the waves. As waves pass down the length of the machine and the sections bend in the water, the movement is converted into electricity via hydraulic power take-off systems housed inside each joint of the machine tubes, and power is transmitted to shore using standard subsea cables and equipment.

2.3 Harvester Conversion Mechanism

In this section we will introduce the three main strategies of energy conversion for vibration energy harvesters: electromagnetic (EM), electrostatic (ES), and piezoelectric (PE). There has been significant research progress in each area and each conversion method has its unique advantages. In the following subsections, the conversion physics and advantages of each approach are given in detail. As a note, a PE harvester was used as a demonstration testbench for the control algorithm and power electronics developed in this thesis. EM and ES harvesters can also be used along with the power electronics.

[3]http://www.oceanpowertechnologies.com/
[4]www.pelamiswave.com/

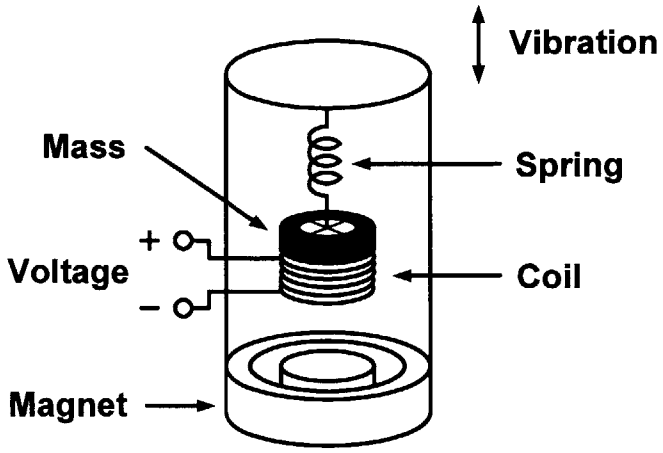

Figure 2-4: Mechanical schematic of a typical electromagnetic energy harvester [2].

2.3.1 Electromagnetic Energy Harvesting

Electromagnetic (EM) energy harvesting seeks to convert vibrational kinetic energy through a voltage induced across coils of wire, which then can deliver power to an appropriate load. This is typically done by moving a permanent magnet pass the coil. Either the permanent magnet, such as that made from Neodymium Iron Boron, or the coil is attached to spring suspension that is vibrationally actuated; the other one remains fixed. In either scenario, the coil will cut through magnetic flux as the cantilever beam vibrates, creating an induced voltage in accordance with Faraday's law. The energy conversion concept used in EM harvesters is basically similar to the mechanism used in large-scale generators and is well demonstrated by Amirtharajah and Chandrakasan [2] as shown in Figure 2-4. Figure 2-5 depicts the coil and magnet configuration of a more advanced multi-pole, multi-phase EM energy harvester developed by Chang et al. [3].

2.3.2 Eletrostatic Energy Harvesting

Electrostatic (ES) energy harvesting couples vibration energy into the system by having it perform work on charges via the electric field between parallel plate capacitors [21]. In a typical scenario, charges are injected onto capacitor plates when they are

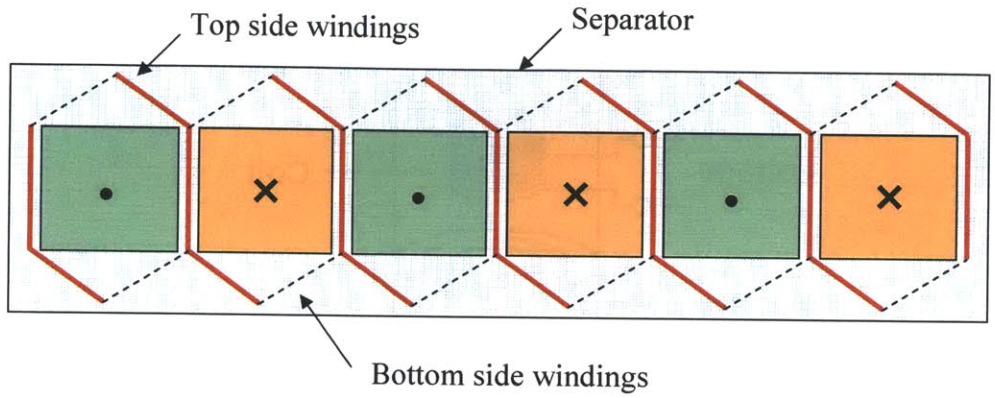

(a)

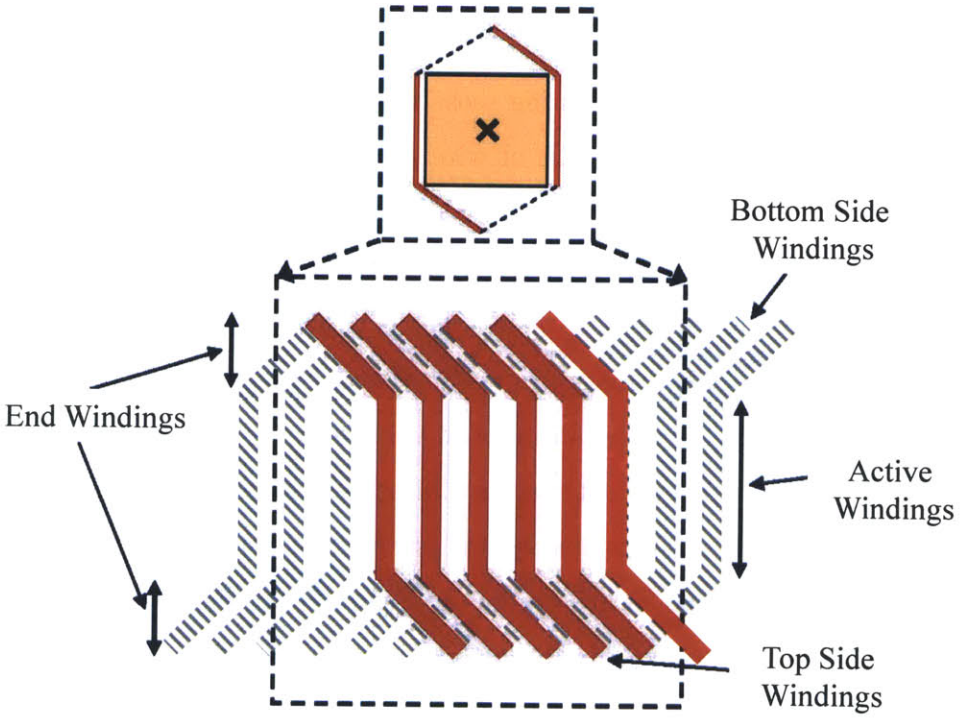

(b)

Figure 2-5: Configuration of a multi-pole eletromagnetic harvester with multi-phase coil arrangements [3]. (a) Illustration of a multi-pole magnet arrangement, and (b) winding pattern over a single pole for a six-phase winding arrangement.

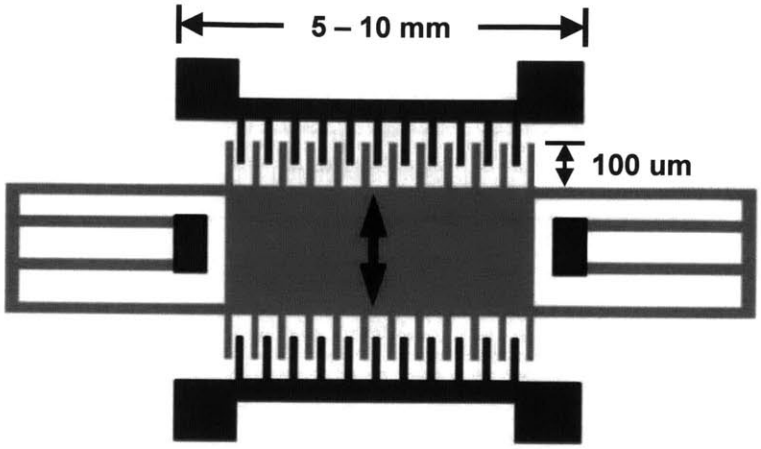

(a)

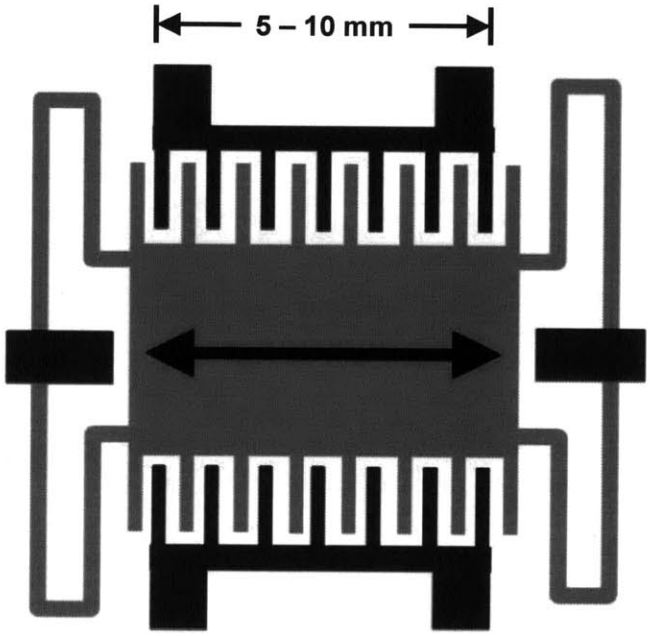

(b)

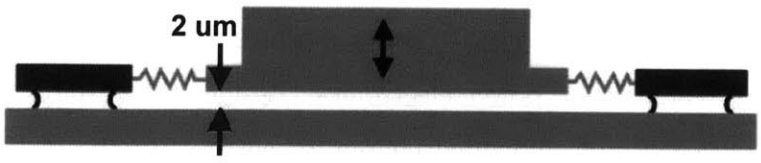

(c)

Figure 2-6: Three possible topologies for MEMS-scale electrostatic energy harvester: (a) in-plane overlap type, (b) in-plane gap closing type, (c) out-of-plane gap closing type [1]

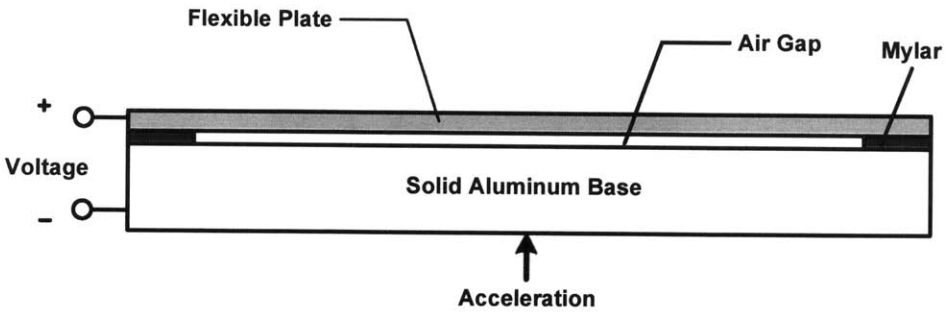

(a)

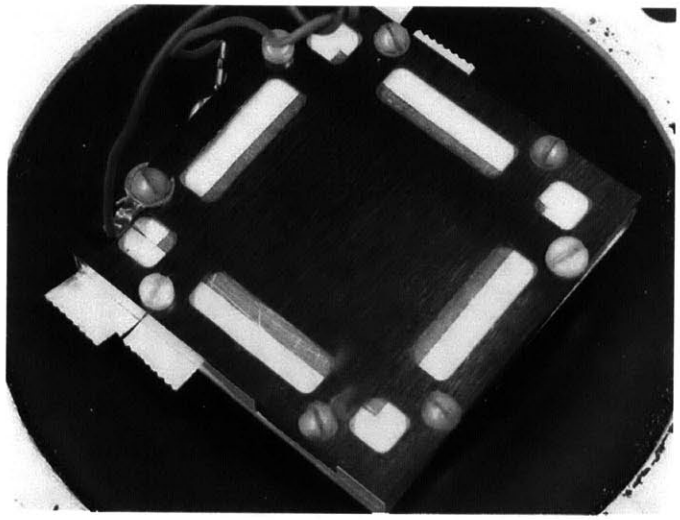

(b)

Figure 2-7: Electrostatic variable capacitor prototype: (a) Side view (not to scale), and (b) actual spring steel variable capacitor prototype [4]

closest together, meaning that the capacitance is at its maximum. Because charges of opposite polarity reside on the separate plates, the plates are attached to each other. Therefore, as vibration energy separates the two plates, it performs positive work on the charges, which are then drained from the plates when the capacitor voltage is highest, and harvested using power electronics. Besides the variable capacitor, one can also employ a layer of embedded charge, or electret, in the dielectric to carry out electric energy harvesting [22]. Such a distribution of permanent charges induces a voltage on the capacitor plates, polarizing them. As external vibration moves the capacitor plates and alters the capacitance, charge transport along the plates delivers power to the load.

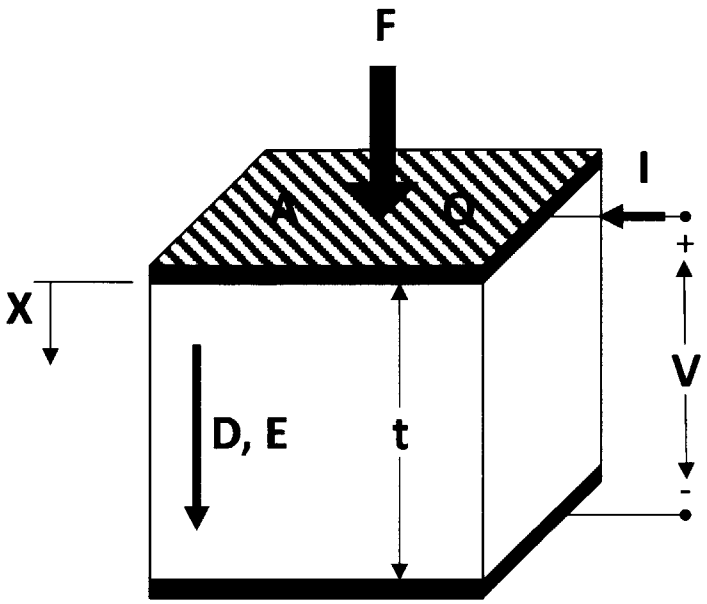

Figure 2-8: Schematic side view of piezoelectric harvester with a width of t and area of A.

2.3.3 Piezoelectric Energy Harvesting

A piezoelectric material is a material that has the capability of transducing mechanical stress or strain into electric field and charge and vice versa. The constitutive equations of a piezoelectric are commonly expressed as

$$\delta = \frac{\sigma}{Y} + dE \tag{2.1}$$

$$D = \varepsilon E + d\sigma \tag{2.2}$$

where the parameters are defined as in Table 2.2. To get a more direct physical idea of the piezoelectric dynamics, Equations 2.1 and 2.2 can be rewritten in terms of macro-variables defined by

Table 2.2: Piezoelectric Parameters

Parameter	Definition	Units
δ	Mechanical Strain	[m/m]
σ	Mechanical Stress	[N/m^2]
Y	Young's Modulus	[N/m^2]
d	Piezoelectric Coefficienct	[m/V]
E	Electric Field	[V/m]
D	Electrical Displacement	[coul/m^2]
ε	Dielectric Constant	[coul/V-m]

$$F = -A \cdot \sigma \tag{2.3}$$

$$X = \delta \cdot t \tag{2.4}$$

$$Q = D \cdot A \tag{2.5}$$

$$v = E \cdot t \tag{2.6}$$

where F is the total force applied to the piezoelectric material, X is the piezoelectric displacement, Q is the charge on the piezoelectric capacitor and v is the applied electrical voltage; see Figure 2-8. Equations 2.1 and 2.2 can now be expressed as

$$F = -\frac{AY}{t}X + \frac{AY}{t}dv \tag{2.7}$$

$$Q = \frac{A\varepsilon}{t}(1-\kappa^2)v + \frac{AY}{t}dX \tag{2.8}$$

where κ is defined as

$$\kappa^2 = d^2\frac{Y}{\varepsilon} \tag{2.9}$$

To further simplify Equations 2.7 and 2.8, we define a proportionality constant G_p such that

$$G_p = \frac{AY}{t}d \tag{2.10}$$

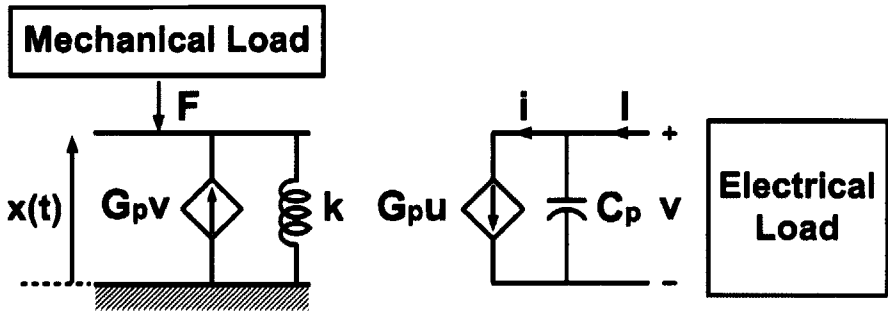

Figure 2-9: Electromechanical model for piezoelectric harvester.

Substituting Equation 2.10 into Equations 2.7 and 2.8 and differentiating Equation 2.8 with respect to time, we get

$$F = -\frac{AY}{t}X + G_p \cdot v \tag{2.11}$$

$$I = \frac{A\varepsilon}{t}(1-\kappa^2)\frac{dv}{dt} + G_p \cdot u \tag{2.12}$$

where $I = \frac{dQ}{dt}$. Expressing Equation 2.11 and 2.12 in terms of the spring constant $k = \frac{AY}{t}$ and parasitic capacitance $C_p = \frac{A\varepsilon}{t}(1-\kappa^2)$,

$$F = -kX + G_p \cdot v \tag{2.13}$$

$$I = C_p\frac{dv}{dt} + G_p \cdot u \tag{2.14}$$

Equations 2.13 and 2.14 are summarized by Figure 2-9. Observing the equations above, we can note that the terms $G_p \cdot v$ and $G_p \cdot u$ are the electromechanical energy conversion terms and can be expressed as

$$f = G_p \cdot v \tag{2.15}$$

$$i = G_p \cdot u \tag{2.16}$$

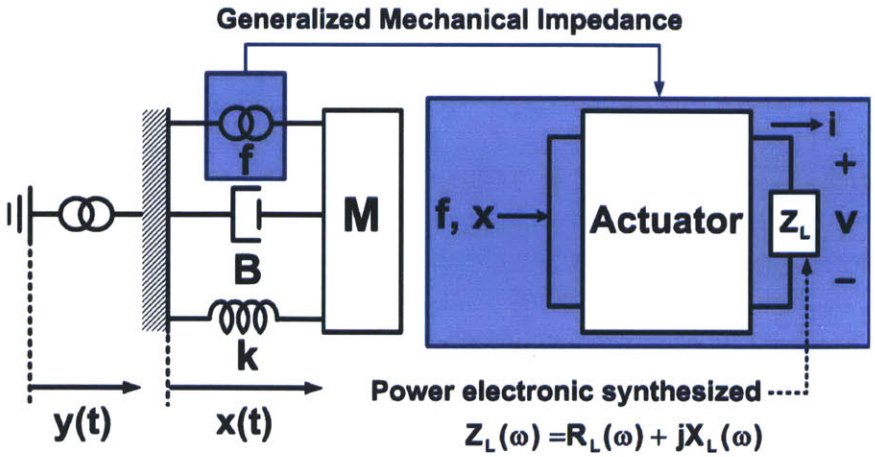

Figure 2-10: Electromechanical model of a energy harvester with general impedance Z_L.

where f and i are the force components due to energy confersion. If we multiply the Equations 2.15 and 2.16 by each other, we can find the relationship $f \cdot u = v \cdot i$ which verifies energy conservation.

This simplified model for PE harvesters as shown in Equations 2.15 and 2.16 is used throughout the rest of this thesis and described in more detail in Chapter 3. As for the latest development in PE harvesters, numerous research groups have focused on piezoelectric energy harvesting [12] due to its potential of achieving the highest converted power per unit volume. Piezoelectric materials, such as quartz and barium titanate, contain permanently polarized structures that produce an electric field when the materials deform as a result of an imposed mechanical strain. Kymissis *et al* employed a unimorph strip made from piezoceramic composite material and a stave made from a multilayer laminate of PVDF foil inside sport sneakers to harvest the parasitic kinetic energy generated during walking [12]. An input signal of 1 Hz, similar in frequency to a person walking briskly, produced 20 mW peak power for the PVDF and 80 mW for the unimorph; this translates to roughly 1-2 mJ per step.

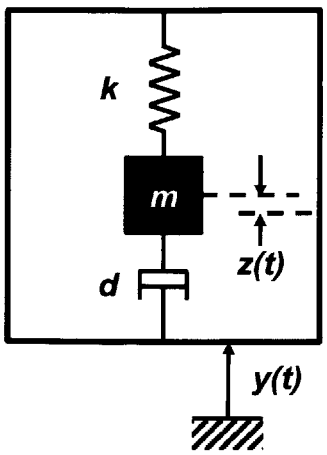

Figure 2-11: Simplified generator mechanical dynamics.

2.4 Vibration Energy Harvesting from Non-ideal Sources

2.4.1 Increasing Operating Frequency Range

Most harvesters are modeled as single degree-of-freedom second-order spring-mass-damper systems (Figure 2-11) as first described by Williams and Yates [23]. In order to maximize the output power, the energy harvester is designed to maximize the coupling between the mechanical energy source and the transduction mechanism. With some mathematical analysis [23], the net power going into the damper d is

$$P = \frac{m\xi_T Y^2 (\frac{\omega}{\omega_r})^3 \omega^3}{[1-(\frac{\omega}{\omega_r})^2]^2 + [2\xi_T \frac{\omega}{\omega_r}]^2} \tag{2.17}$$

where m is the inertial mass, ξ_T is the total damping factor which includes both internal and external electrical damping, Y and ω are respectively the maximum amplitude and the angular frequency of the vibration source, and ω_r is the resonant frequency of the generator. From Equation 2.17, it can be observed that the power is maximized at the resonant frequecy ($\omega = \omega_r$) and can be expressed as

$$P_{MAX} = \frac{mY^2\omega^3}{4\xi_T} \tag{2.18}$$

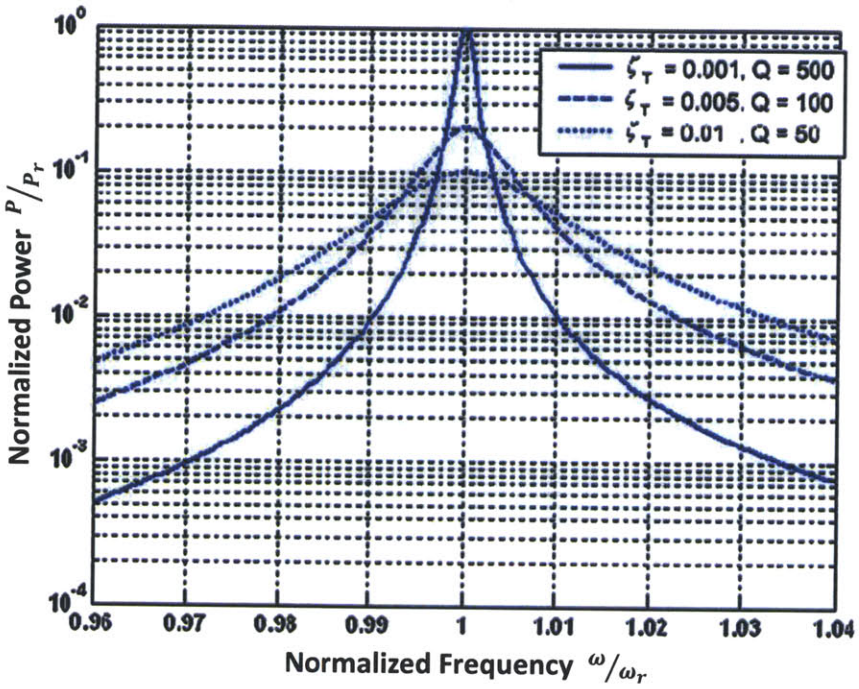

Figure 2-12: Power spectrum of a energy harvester with various damping factors and Q-factors [5].

Figure 2-12 shows the power spectrum of the generator with various damping factors ξ_T and quality factors Q. which are defined by

$$\xi_T = \frac{m \cdot \omega_r}{Q} \tag{2.19}$$

The output power is normalized with the output power at the resonant frequency ω_r and the vibration frequency is normalized with the resonant frequency ω_r. It can be seen that the maximum power is generated when the frequency of the vibration source is equal to the resonant frequency of the generator and that the power drops off significantly when these two frequencies are off by even a few percent. In applications such as moving vehicles and human motion where the vibration frequency changes, the efficiency of generators with one fixed resonant frequency is dramatically reduced since such generators will not always be excited at resonance. To date, there are generally two approaches to solving this problem: tuning the resonant frequency of a single generator, and widening the bandwidth of the generator.

Resonant Frequency Tuning

One method to deal with a varying vibration harmonic is to adjust, or tune, the resonant frequency of a single generator such that it matches the vibration frequency of the ambient source. This can be achieved by changing the mechanical characteristics of the resonator or the electrical load. Maximum power can then be generated at various frequencies without reducing the Q-factor and with high efficiency per unit volume.

Mechanical tuning can be achieved by changing the dimensions of the structure [24], the position of the center of gravity [25] and the spring stiffness [26, 27, 28, 29, 30, 31, 32]. However, the first two methods are less suitable for *in situ* tuning (tuning while the generator is mounted on the vibration source and operating) and requires additional mechanisms that burn power themselves. Adjusting the spring stiffness, on the other hand, permits *in situ* tuning. One commonly used method is to soften the spring stiffness. The principle is to apply a compensating spring in parallel with the mechanical spring. Therefore, the effective spring constant of such a device, k_{eff} , becomes

$$k_{eff} = k + k_a \tag{2.20}$$

where k is the mechanical spring constant and k_a is the compensating spring constant. The modified vibration frequency then becomes

$$f_r = \frac{1}{2\pi}\sqrt{\frac{k_{eff}}{m}} = \frac{1}{2\pi}\sqrt{\frac{k + k_a}{m}} \tag{2.21}$$

The negative spring k_a can be applied electrostatically [26, 27, 28], piezoelectrically [29], magnetically [30] or thermally [31, 32]. Most of the references discuss tunable resonators for applications such as vibration measurements [28] and not energy harvesters, but the principles are identical. The only difference is that the additional inertial mass present in an energy harvester will reduce the tuning effectiveness and increase the power required to tune. It should be noted that these tuning mechanisms all consume power and could often times be larger than the actual harvested energy.

Resonant frequency tuning by adjusting the electrical load has also been shown to be practically feasible. The basic principle of electrical tuning is to change the electrical loading by adjusting the electrical impedance, which causes the power spectrum of the generator to shift. This method consumes little energy as it does not involve any change in mechanical properties. The only energy consumed is in the electronic switches and control unit, which is typically far less than that consumed by mechanical tuning methods. In addition, it is much easier to implement than mechanical methods. This approach can also be combined with power conditioning which is present in any case. More details on electrical load tuning are given in Chapter 3 and the power electronics implementation can be found in Chapter 4.

Electrical tuning of piezoelectric harvesters generally incorporates a bimorph structure as shown in Figure 2-8. The resonant frequency of such a generator can be tuned by varying the capacitive load [33]. The tuning effectiveness with this method is quite low and cannot achieve a large tuning range. An extra closed loop system must also be introduced to control the tuning process.

Resonant frequency tuning by using inductors and capacitors has been explored and modeled by Cammarano *et al* [17]. Their model states that by tuning the resistive load of the back-end power electronics, one can effectively increase the output power at off resonance frequencies as shown in Figure 2-13. The output power is normalized with the output power at the resonant frequency ω_r and the vibration frequency is normalized with the resonant frequency ω_r. In this thesis, a similar model is developed and is shown to produce similar results. However, important challenges such as power electronics implementation of complex impedances and multi-harmonic vibrations have not been studied in [17]. These challenges will be addressed in this thesis.

Resonant Bandwidth Enhancement

The second approach to dealing with a varying harmonic is to widen the bandwidth of the generator which brings out the trade-off between the system bandwidth and the quality-factor (Q). From Equations 2.18 and 2.19, we can find that a wider bandwidth

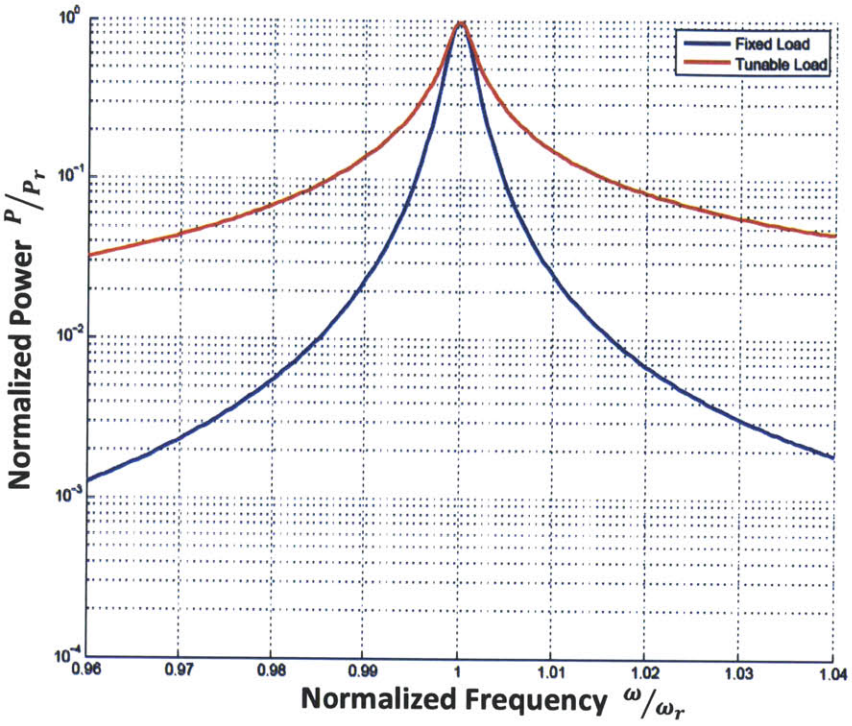

Figure 2-13: Power Spectrum of a energy harvester with tunable load and fixed load

means a lower Q and lower peak output power for a single resonator. A common solution to this trade-off is to design an array of small generators [34, 35, 36], each of which works at a different frequency. Thus, the assembled generator has a wide operational frequency range while the Q-factor does not decrease. This phenomenon is shown in Figure 2-14. However, this assembled generator must be carefully designed so that each individual generator does not affect the others. From a practical point of view, this is a great waste of valuable mass resources since most of the harvester mass is dormant at any one time. This point can be further strengthened by examining Equation 2.18 where the output power is proportional to the harvester mass. If only a fraction of the mass is utilized at a given time, the output power would also be a fraction of the optimal output power when the entire mass is utilized.

Another method used to increase the bandwidth of the generator is by applying an amplitude limiter. The theory behind this method is complex and details can be found in [37]. The drawbacks are that this method causes the maximum output power

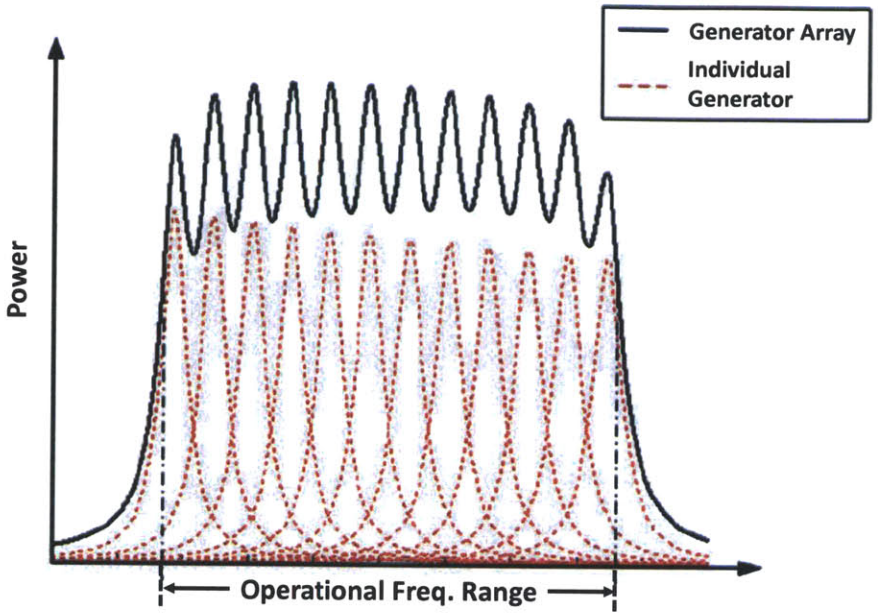

Figure 2-14: Power spectrum of a generator array

to drop by limiting the vibration amplitude and the repeating mechanical contact between the cantilever and the mechanical stopper may result in earlier fatigue-induced failure in the cantilever beam. Experimental measurements showed that the up-sweep bandwidth was 240% wider than that of the architecture without a stopper at the half-power level, but the maximum output voltage was 30% less.

Using coupled oscillators can also increase the operational bandwidth of the generator [38]. The proposed generator employs a pair of coupled oscillators that consist of two springs, two masses and two dampers. It can achieve flat response over a wide frequency range. However, the maximum output power of a coupled oscillator generator is significantly lower than that of a generator with a single mass.

Finally, nonlinear [39, 40, 41] and bi-stable [42] structured generators are also potential solutions to increase the operational frequency range of vibration-based microgenerators. The theory of vibration energy harvesting using nonlinear generators was investigated by Ramlan *et al* [43]. Instead of using a conventional second-order model as shown in Equation 2.17, nonlinear generators were modeled using Duffing's equation according to

$$m\frac{d^2z(t)}{dt^2} + b\frac{dz(t)}{dt} + kz(t) + k_n[z(t)]^3 = -m\frac{d^2y(t)}{dt^2} \tag{2.22}$$

where the spring force is the combination of the linear force, $kz(t)$, and the nonlinear force, $k_n[z(t)]^3$. Such devices have a hardening spring which has the effect of shifting the resonant frequency. Numerical and analytical studies showed that a device with a hardening spring has a larger bandwidth over which power can be harvested due to the shift in the resonance frequency. Nonlinear generators can be conveniently realized by using a magnetic spring instead of a conventional spring. Spreemann *et al* [39] reported a tunable electromagnetic vibration energy harvester with a magnetic spring, which combined a tuning mechanism with the nonlinear structure. Burrow *et al* [40] reported another nonlinear generator consisting of a linear spring with the nonlinearity caused by the addition of magnetic reluctance forces.

In summary, for vibration energy harvesting, possible strategies to increase the operation frequency range include the following:

- changing spring stiffness;
- straining the structure;
- adjusting reactive electric load;
- using a generator array;
- employing nonlinear and bi-stable structures.

The last decade has seen great improvement of vibration based micro-generators in powering wireless sensor networks by continuous effort of research groups and companies all around the world. The development of strategies to increase the operational frequency range of vibration-based micro-generators will bring these energy sources to much wider application.

2.4.2 Multi-harmonic and Broadband Excitation

Multi-harmonic and broadband excitation is another vibration characteristic where significant amount of energy is untapped. In the energy harvesting area, it is common to analyze devices or report device performance under the simpler and far more idealized case of sinusoidal excitations. This allows for clean and unambiguous specification of operating conditions that are easy to realize experimentally and are conveniently used to compare results between researchers. The purpose of an idealized signal is to capture the essence of a variety of real-world signals. Many of these may be far from sinusoidal and may have substantial bandwidths. Recent experimental works acknowledge this and report results on the excitation of energy harvester prototypes by broadband random vibrations made by random noise generators [44].

Theoretical investigation and SPICE simulation of the properties of energy harvesters subject to broadband excitation has also been done [45, 46]. Halvoersen *et al* established closed-form expressions for output power, proof mass displacement variance, and optimal load for linear energy harvesters driven by broadband excitations. Energy harvesters behave qualitatively quite differently when exposed to broadband instead of sinusoidal excitations. Experimental results [47] of broadband excitations on nonlinear spring based energy harvesters show that considerable bandwidth enhancements can be achieved by use of nonlinear springs without relying on mechanical stopper impacts, resonance tuning, or large electromechanical coupling.

Models and experiments of broadband excitation acting on energy harvesters have given us a much better understanding in this area. However, there still remains a question: what is the optimal conversion method? Various approaches such as nonlinear springs have proven to enhance harvester performance, but none have been proved to be the optimal solution. A significant portion of this thesis will focus on developing the theory and model of finding the optimal conversion method for energy harvesters under broadband excitation. A hardware implementation, integrated circuits if possible, will then be developed to solidify the model.

2.5 Energy Harvesting Interfacing Circuits

The stellar advances in CMOS process technologies and circuit techniques have reduced the power consumption of circuits far enough to enable a new class of self-powered systems. To minimize power consumption of the electronic devices, significant research has targeted the load circuits like radios and DSP's where process scaling coupled with circuit technique like voltage scaling and parallelism have reduced power consumption of circuits dramatically to less than 10 mW. However, these advancements in power reduction do not lead to an equivalent improvement in operating lifetime. This is because the intermediate energy management circuits are traditionally not efficient and have become a key bottleneck in low power systems.

One of the major challenges in these interfacing circuits is the low startup voltage. Ramadass *et al* [48] presented a mechanically assisted startup circuit that enables operation of a thermoelectric energy harvester from input voltages as low as 35 mV. Carlson *et al* [49] also presented a low-power boost converter that operates from input voltages ranging from 20 mV to 250 mV while supplying a regulated 1 V output. It demonstrated an efficiency that was 15% higher than the state-of-the-art for voltage conversion ratios above 20. It was achieved by utilizing a technique allowing synchronous rectification in the discontinuous conduction mode.

Another area of challenge is the rectification of the harvester output voltage since the voltage levels are much lower than the transistor threshold voltage. Ramadass *et al* [7] designed a bias-flip rectifier circuit that could improve the power extraction capability from piezoelectric harvesters over conventional full-bridge rectifiers and voltage doublers by greater than 4X. The inductor used within the bias-flip rectifier was also shared efficiently with a multitude of switching DC-DC converters within the system which ultimately reduced the overall component count.

In the past few years, significant breakthrough has been made in energy harvesting interfacing low power circuit design. However, few have addressed the non-ideal vibration conditions mentioned in the previous section. In this thesis, an integrated circuit will be designed to handle a certain scope of non-ideal vibrations. The scope

will depend on the optimal control model and the final application of the energy harvesting system.

2.6 Chapter Summary

This chapter served both as an introduction to the world of energy harvesting as well as motivation for the rest of this thesis. The chapter started out with the reason energy harvesting research has burgeoned in recent years and specifically speaking, why vibration energy harvesting has garnered significant interest. Within vibration energy harvesting, there are three major energy conversion methods: electromagnetic, electrostatic and piezoelectric. Details of the conversion physics are also given in this chapter. Taking the piezoelectric harvester for an example, this thesis proposed a simplified model which describes the electromechanical conversion physics as the following

$$f = G_p \cdot v \tag{2.23}$$

$$G_p \cdot u = i \tag{2.24}$$

This simplified model is derived from the basic coupling coefficient and physical parameters of the piezoelectric and can be found in Section 2.3.3. It should be emphasized that Equations 2.23 and 2.24 are only a part of the physics and the spring constant k and parasitic capacitance C_p will be a absorbed into the mechanics and electrics as shown in Figure 2-10. In the second half of this chapter, an overview of the challenges and previous works by other researchers on harvesting energy from non-ideal sources is given. This serves as a starting foundation of previous knowledge for this thesis. Since this thesis will take an electrical circuit approach to address the challenges in energy harvesting, previous works on harvester interfacing circuits are given in the final part of this chapter.

In the following chapter, we will take a look at the theory of optimal energy

transfer by finding the optimally matched electrical impedance. The chapter will start out with the well known spring-mass-damper model under single frequency vibration and expand to simultaneous multi-frequency vibrations at the end. This theory will then be implemented in power electronics described in Chapter 4 and verified experimentally in Chapter 5 and 6.

Chapter 3

Harvester Electrical Loading

The concept of electrically tuning the resonant frequency of a vibration harvester first arose in response to the vibration frequency shift non-ideality commonly found in ambient vibration sources. As mentioned in the previous chapter, other tuning methods such as spring stiffness adjustment, generator arrays and non-linear spring structures have also proven capable of increasing the operational frequency range. However, electrical tuning normally consumes much less energy than mechanical stiffening methods since the only energy consumed is in the electronic switches and control unit. In addition, it is easier to implement and provides dynamic tunability. More advanced power electronics implementations also embed power conditioning (AC/DC) and reduces the need for an additional voltage rectifier.

Previous research from other groups have demonstrated tuning with passive components [17] and also with a more complex power electronics synthesized load [20]. Both of these works focused on tuning the mechanical resonant frequency such that it can match the vibration frequency when the latter shifts. This thesis will build on these works and expand the application boundaries of electrical tuning to multi-frequency energy harvesting. As mentioned in Chapter 1, multi-frequency or multi-harmonic vibrations are commonly observed due to the power supply frequency and machines that surround our daily lives. While other harmonics do not interfere with the vibration at the mechanical resonant frequency, they do present untapped energy that could have otherwise been utilized. An easy solution is to build an array of har-

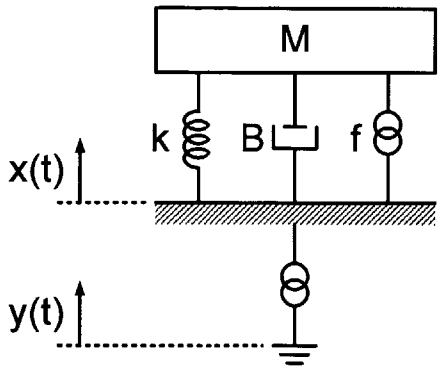

Figure 3-1: Spring-mass-damper model.

vesters, each resonating at one of the harmonics [34, 35, 36]. This method is feasible when mass and volume is not limited, but in most applications, the volume and mass which the harvester can work with is limited, and therefore this method is wasteful of valuable mass resources. To our knowledge, the research conducted in this thesis is the first to explore the idea of multi-frequency harvesting by electrically tuning a single resonant harvester.

This chapter serves as the theoretical basis of the entire thesis. It begins with an introduction to the electromechanical coupling theory of general single resonance vibration harvesters and then discusses the idea of electrical impedance matching to deliver the maximum amount of power to the load. The electrical impedance matching theory is then extended to dual-frequency, triple-frequency and finally N-frequency energy harvesting.

3.1 Spring-mass-damper Model

The spring-mass-damper model [23], as shown in Figure 3-1, is the most common mechanical model for vibration energy harvesters. The ambient vibration from the environment can be modeled as a sinusoidal vibration source $y(t)$ relative to the inertial ground.

Assuming the vibration source to be a surface such as a table or window, there will only be one terminal connected to the harvester. Therefore, a proof mass M is

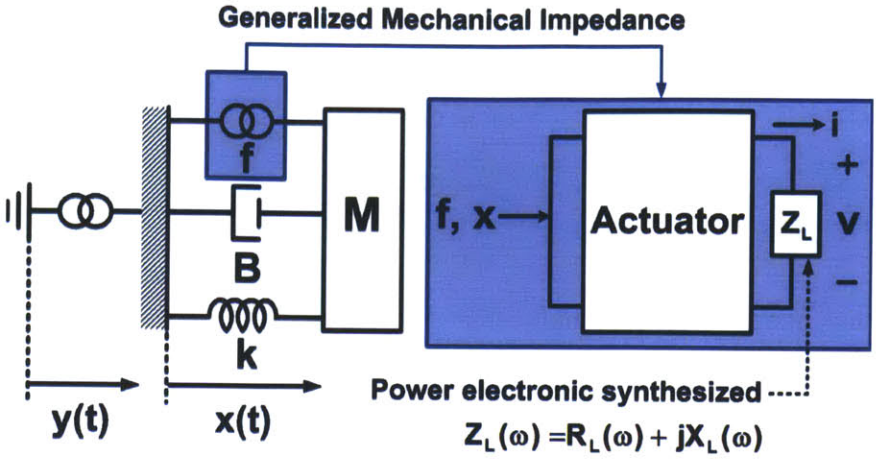

Figure 3-2: Electrically tuned load creates the desired mechanical loading through an electrical impedance synthesized with power electronics. The actuator is lossless and storageles.

required at the other terminal to push against the vibration surface terminal, and a suspension (spring) is required. The spring has a spring constant k and the suspension has a damping coefficient B. The harvester has a mechanical structure as shown in Figure 2-3(a).

The proof mass vibration can be modeled as a sinusoidal $x(t)$ relative to the vibration surface. The electromechanical coupling effect can be easily understood with Figure 3-2, where the energy conversion relationship between the electrical side and the mechanical side can be described as

$$v \cdot i = f \cdot \frac{dx}{dt} \tag{3.1}$$

v and i are respectively the electrical load voltage and current. Z_L is the load impedance. This relationship assumes the actuator is lossless and storageless and is valid for all vibration energy harvesting methods. However, depending on the harvester physics, each energy conversion method has a different electromechanical coupling model. For a PE harvester,

$$f = G_p \cdot v \tag{3.2}$$

$$i = G_p \frac{dx}{dt} \tag{3.3}$$

On the other hand, for an EM harvester

$$f = G_m \cdot i \tag{3.4}$$

$$v = G_m \frac{dx}{dt} \tag{3.5}$$

The proportionality constants G_p and G_m are defined here to simplify the equation derivations, however, it should be noted that they are determined by the coupling coefficient and the physical dimensions of the harvester.

With the electromechanical coupling understood, let us now revisit the spring-mass-damper model of Figure 3-1 and from that we can derive the governing differential equation

$$M\frac{d^2}{dt^2}(x+y) = -kx - B\frac{dx}{dt} + f \tag{3.6}$$

With some reorganization, Equation 3.6 can be expressed as

$$M\frac{d^2x}{dt^2} + B\frac{dx}{dt} + kx = -M\frac{d^2y}{dt^2} + f \tag{3.7}$$

Here we will use a PE harvester for example, but it should be noted that an EM harvester can also be similarly analyzed yielding similar results. Using the results from Equations 3.1, 3.2 and 3.3, we get

$$f = G_p \cdot v \tag{3.8}$$

$$= -G_p \cdot Z_L(\omega) \cdot i \tag{3.9}$$

$$= -G_p^2 \cdot Z_L(\omega) \cdot \frac{dx}{dt} \tag{3.10}$$

where $Z_L(\omega)$ is the complex load impedance and includes C_p in the case of a piezoelectric harvester; $Z_L(\omega)$ would include winding inductances in the case of an electromagnetic harvester. This result can then be substituted into Equation 3.7 where we assume

$$x(t) = Xe^{j\omega t} \tag{3.11}$$

$$y(t) = Ye^{j\omega t} \tag{3.12}$$

$$\tag{3.13}$$

Under the assumption of sinusoidal steady state, the substitution of Equation 3.8 through 3.13 into 3.7 yields

$$(k - M\omega^2 + j\omega(B + G_p^2 Z_L)) \cdot X = M\omega^2 \cdot Y \tag{3.14}$$

In order to find the power delivered to the resistive load, $Z_L(\omega)$ is expressed as the sum of the resistance $R_L(\omega)$ and reactance $X_L(\omega)$.

$$Z_L(\omega) = R_L(\omega) + jX_L(\omega) \tag{3.15}$$

To clarify, the resistance $R_L(\omega)$ is not a real lossy resistor, but a proxy for an energy conversion and storage process. The power into $R_L(\omega)$ is the useful harvested work. From Equation 3.14, the displacement amplitude X can be expressed as

$$X = \frac{M\omega^2 Y}{(k - M\omega^2 - \omega G_p^2 X_L) + j\omega(B + G_p^2 R_L)} \tag{3.16}$$

Since the output power delivered to the electrical load is

$$P = \frac{1}{2} R_L \omega^2 G_p^2 |X|^2 \tag{3.17}$$

Substitution of Equation 3.16 into Equation 3.17 yields

$$P = \frac{1}{2} \frac{R_L \omega^6 G_p^2 M^2 Y^2}{(k - M\omega^2 - \omega G_p^2 X_L)^2 + \omega^2 (B + G_p^2 R_L)^2} \tag{3.18}$$

This is the general output power solution for a vibration energy harvester using the spring-mass-damper model. From Equation 3.18, it can be found that in order to maximize the output power, X_L and R_L should be chosen such that

$$X_L(\omega) = \frac{k - M\omega^2}{\omega G_p^2} \tag{3.19}$$

$$R_L = \frac{B}{G_p^2} \tag{3.20}$$

From Equations 3.19 and 3.20, we can see that while $X_L(\omega)$ is frequency dependent, R_L is a fixed value. From a physical perspective, $X_L(\omega)$ forms a resonant energy exchange so that the spring and the mass cancel out at any frequency. R_L on the other hand is the matched load for maximum power transfer. At this new resonance, the maximum power can be expressed as

$$P = \frac{M^2 \omega^4 |Y|^2}{8B} \tag{3.21}$$

It should be noted that Equations 3.19 and 3.20, at this point of the discussion, need only be satisfied at the specific ω of the vibration source.

3.2 Harvester Equivalent Circuit Model

Continuing our discussion from the previous section, the optimal load impedance is determined by satisfying Equations 3.19 and 3.20. To gain more intuition from a circuit point of view, the mechanical spring-mass-damper model is transformed into

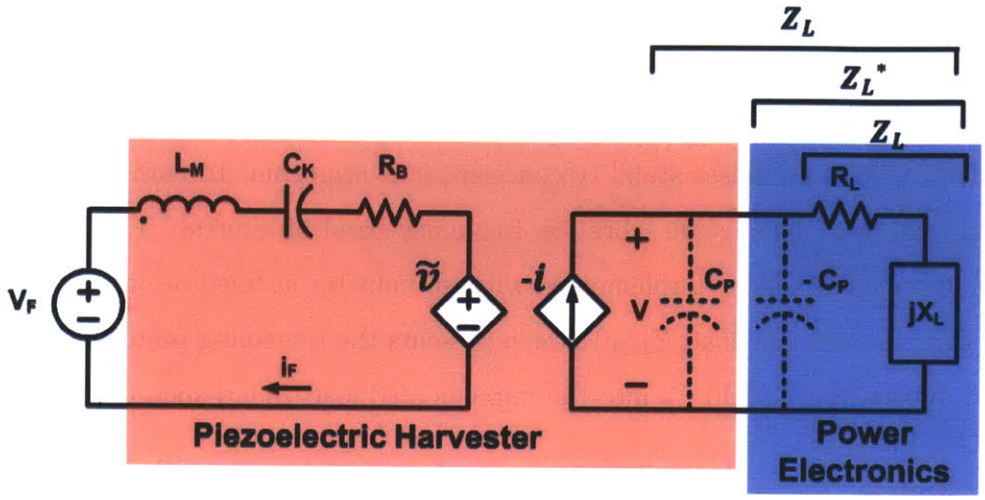

Figure 3-3: Equivalent circuit of a piezoelectric harvester loaded with a generalized impedance.

the equivalent circuit model [50] shown in Figure 3-3. Here we again use a piezoelectric harvester as an example. The first subsection to follow goes into detail on how the parasitic capacitance is included in the general matching impedance. The second subsection addresses the equivalent circuit model.

3.2.1 Piezoelectric Harvester Parasitic Capacitance

As discussed in Section 2.3.3, the piezoelectric harvester contains a parallel parasitic capacitance at the electrical output. This can be shown in Figure 3-3 where the red box represents the piezoelectric harvester equivalent circuit model and the blue box represents the electrical load which would be implemented in power electronics in this thesis. Details of the equivalent circuit model and the power electronics will be given in the following subsection, and in Chapter 4, respectively. In this section, we focus on dealing with the parasitic capacitance C_p.

From Equation 2.14 in the previous chapter, we note that C_p will greatly affect the output electrical characteristics of the harvester. In order to simplify the expressions for finding the matched load for a piezoelectric harvester, the optimal matching impedance shown in Equations 3.19 and 3.20 implicitly includes C_p. There are essen-

tially two approaches to handling this inclusion. The first is to implement a $-C_p$ in parallel with the external load so as to cancel C_p. The power electronics implementation of a $-C_p$ has been demonstrated by Toh et al [20]. Even though a broadband negative capacitance raises stability concerns, it is important to realize that $-C_p$ is needed only over the specific vibration frequency band of interest. The capacitance cancellation could also be implemented with an inductor at fixed resonant frequency. With C_p cancelled, the load $Z_L(\omega)$ now represents the remaining matched load. The second approach is to fold C_p into the implemented load $Z_L(\omega)$ such that

$$Z_L^* = \frac{-1}{j\omega C_p} || Z_L \tag{3.22}$$

where it is Z_L^* that is actually implemented in power electronics as indicated in the blue box shown in Figure 3-3. In this case,

$$Z_L^* = \frac{R_L + jX_L}{1 - j\omega C_p(R_L + jX_L)} = \frac{R_L + jX_L}{1 + \omega C_p X_L - j\omega R_L C_p} \tag{3.23}$$

This too could have stability concerns but need not be implemented in broad band. Rather it need be implemented only at the specific resonant frequency of the harvester.

3.2.2 Piezoelectric Harvester Equivalent Circuit Model

This section now proceeds under the assumption that C_p is "removed" as discussed in Section 3.2.1. To develop an equivalent electrical model, the piezoelectric coupling is modeled as an equivalent transformer, as shown in Figure 3-3. The closed circuit on the left represents the spring-mass-damper mechanical model where the mass is expressed as an equivalent inductance L_M, the spring is expressed as an equivalent capacitance C_K and the damper is expressed as an equivalent resistance R_B. In this model, voltage represents force and current represents velocity.

To get a sense of how the spring-mass-damper model translates to the equivalent circuit model, we write out the differential equations for both models. For the spring-mass-damper model, Equation 3.7 is rewritten here for ease of comparison as

$$M\frac{d^2x}{dt^2} + B\frac{dx}{dt} + kx = -M\frac{d^2y}{dt^2} + f \tag{3.24}$$

Now let us define a the relationship between velocity and current, and the relationship between force and voltage, as

$$i_F \equiv -J_i \cdot \frac{dx}{dt} \tag{3.25}$$

$$V_F \equiv J_v \cdot M\frac{d^2y}{dt^2} \tag{3.26}$$

where V_F and i_F are the equivalent mechanical voltage and current seen in Figure 3-3, while J_i and J_v are the current and voltage scales from velocity and force. J_i and J_v have the units of $[A \cdot s/_m]$ and $[^V/_N]$. Following substitutions of Equations 3.25 and 3.26, Equation 3.24 can be rewritten as

$$-(\frac{M}{J_i}) \cdot \frac{di_F}{dt} - (\frac{B}{J_i}) \cdot i_F - \frac{k}{J_i}\int i_F\,dt \; = -\frac{v_F}{J_v} + f \tag{3.27}$$

Multiplying both sides of Equation 3.27 by $(-J_v)$ yields

$$(M\frac{J_v}{J_i}) \cdot \frac{di_F}{dt} + (B\frac{J_v}{J_i}) \cdot i_F + k\frac{J_v}{J_i}\int i_F\,dt \; = v_F - J_v \cdot f \tag{3.28}$$

Equation 3.28 can then be reorganized as

$$L_M\frac{di_F}{dt} + R_B \cdot i_F + \frac{1}{C_K}\int i_F\,dt \; = v_F - \tilde{v} \tag{3.29}$$

where the following variables are defined as

$$L_M \equiv M \cdot \frac{J_v}{J_i} \tag{3.30}$$

$$R_B \equiv B \cdot \frac{J_v}{J_i} \tag{3.31}$$

$$C_K \equiv \frac{1}{k} \cdot \frac{J_i}{J_v} \tag{3.32}$$

$$\tilde{v} \equiv J_v \cdot f = J_v \cdot G_p v \tag{3.33}$$

The equivalent circuit model can be more easily understood from Figure 3-3. Analyzing the left-half closed circuit in the equivalent circuit model in Figure 3-3, and assuming sinusoidal steady state, it can be shown that

$$i_F = \frac{V_F - G_p J_v V}{j\omega L_M + \dfrac{1}{j\omega C_K} + R_B} \tag{3.34}$$

$$= \frac{j\omega C_K (V_F - G_p J_v V)}{1 - \omega^2 L_M C_K + j\omega R_B C_K} \tag{3.35}$$

$$i_F \cdot (1 - \omega^2 L_M C_K + j\omega R_B C_K) = j\omega C_K (V_F - G_p J_v V) \tag{3.36}$$

The output voltage V can be expressed as

$$V = Z_L \cdot (-i) \tag{3.37}$$

$$= Z_L \cdot \frac{G_p}{J_i} i_F \tag{3.38}$$

Substituting Equation 3.38 into Equation 3.36 with some further reorganization, the equivalent proof mass velocity i_F can be shown to be

$$i_F = \frac{j\omega C_K V_F}{1 - \omega^2 L_M C_K + j\omega C_K (R_B + Z_L \tilde{G_p}^2)} \tag{3.39}$$

where

$$\tilde{G_p}^2 = G_p^2 \cdot \frac{J_v}{J_i} \tag{3.40}$$

Expanding Z_L into $(R_L + jX_L)$, i_F can then be expressed as

$$i_F = \frac{j\omega C_K V_F}{(1 - \omega^2 L_M C_K - \omega C_K \tilde{G_p}^2 X_L) + j\omega(R_B + \tilde{G_p}^2 R_L)C_K} \tag{3.41}$$

The output power P_L delivered to the resistive load R_L can then be derived as follow

$$P_L = \frac{1}{2}|i|^2 R_L \tag{3.42}$$

$$= \frac{1}{2}\tilde{G_p}^2 |i_F|^2 R_L \tag{3.43}$$

$$= \frac{\frac{1}{2}\tilde{G_p}^2 R_L \omega^2 C_K^2 |V_F|^2}{(1 - \omega^2 L_M C_K - \omega C_K \tilde{G_p}^2 X_L)^2 + \omega^2 (R_B + \tilde{G_p}^2 R_L)^2 C_K^2} \tag{3.44}$$

$$= \frac{\frac{1}{2}\tilde{G_p}^2 R_L |V_F|^2}{(\frac{1}{\omega C_K} - \omega L_M - \tilde{G_p}^2 X_L)^2 + (R_B + \tilde{G_p}^2 R_L)^2} \tag{3.45}$$

where Equation 3.45 is maximized at

$$X_L = \frac{1}{\tilde{G_p}^2}(\frac{1}{\omega C_k} - \omega L_M) \tag{3.46}$$

$$R_L = \frac{R_B}{\tilde{G_p}^2} \tag{3.47}$$

At this matching condition, the maximum power can be expressed as

$$P_L = \frac{|V_F|^2}{8R_B} \tag{3.48}$$

$$= \frac{M^2 \omega^4 |Y|^2}{8B} \tag{3.49}$$

The maximum output power derived from the equivalent circuit model shown in Equation 3.49 is identical to the result in Equation 3.21 which confirms that the equivalent circuit model and the spring-mass-damper model are consistent.

In addition to the real power being delivered to R_L, the reactive power delivered to X_L can be expressed as

$$P_{XL} = \frac{1}{2}|i|^2 X_L \tag{3.50}$$

$$= \frac{1}{2}\tilde{G_p}^2 |i_F|^2 X_L \tag{3.51}$$

$$= \frac{\frac{1}{2}\tilde{G_p}^2 X_L \omega^2 C_K^2 |V_F|^2}{(1-\omega^2 L_M C_K - \omega C_K \tilde{G_p}^2 X_L)^2 + \omega^2 (R_B + \tilde{G_p}^2 R_L)^2 C_K^2} \tag{3.52}$$

$$= \frac{\frac{1}{2}\tilde{G_p}^2 X_L |V_F|^2}{(\frac{1}{\omega C_K} - \omega L_M - \tilde{G_p}^2 X_L)^2 + (R_B + \tilde{G_p}^2 R_L)^2} \tag{3.53}$$

While it cannot be directly observed quantitatively the amount of reactive power being exchanged purely from the expression shown in Equation 3.53, we will compute it in the following section with different X_L configurations.

3.3 General Matching Condition

From the result shown in Equation 3.49, we can find the theoretical maximum output power the harvester can deliver to the resistive load at a given frequency. In addition, the required resistance and reactance are given in Equations 3.47 and 3.46 respectively at each frequency.

By further analyzing the optimal load resistance R_L given in Equation 3.47, we can find that it only depends on the mechanical damping R_B and the conversion ratio G. Both R_B and G are constant physical parameters of a given harvester. Therefore, the optimal load resistance is independent of frequency, meaning that regardless of the vibration frequency and number of harmonics, the optimal load resistance remains

constant. This is an important result for harvester impedance matching.

On the other hand, the optimal load reactance X_L, as expected, is frequency dependent and is determined by the equivalent spring-mass and the conversion ratio as shown in Equation 3.46. From another perspective, X_L makes certain that the resonance condition is satisfied at all frequency and provides the possibility of tuning the resonant frequency and creating additional resonances. Further details of the design of the load reactance X_L are given in this section. The road toward multi-frequency harvesting starts out with single resonant frequency tuning and gradually evolves toward dual-frequency harvesting, triple-frequency harvesting and finally N-frequency harvesting.

3.3.1 Single Resonant Frequency Tuning

From previous work by Cammarano *et al.* [17], we know that the resonant frequency of a vibration harvester can be electrically tuned by loading the harvester with reactive components such as inductors and capacitors. The additional inductor and capacitor changes the load reactance X_L and effectively changes the roots of Equation 3.46, which determine the resonant frequency. Here we take a load inductor as an example to study the phenomenon of frequency tuning with reactive components. With no reactive loading, the original resonant frequency ω_{RES} can be found from Equation 3.46 as

$$\omega_{RES} = \sqrt{\frac{1}{L_M C_K}} \tag{3.54}$$

With an inductive load $X_L = \omega L_L$, the resonant frequency then becomes

$$\omega'_{RES} = \sqrt{\frac{1}{C_K(L_M + G_p^2 L_L)}} \tag{3.55}$$

indicating that an inductive load lowers the resonant frequency. As one would expect, a capacitive load would have an opposite effect and increase the resonant frequency. This frequency shifting phenomenon with reactive components is shown in the MATLAB simulations (Appendix A.1.1) results in Figure 3-4. The blue curve in the top

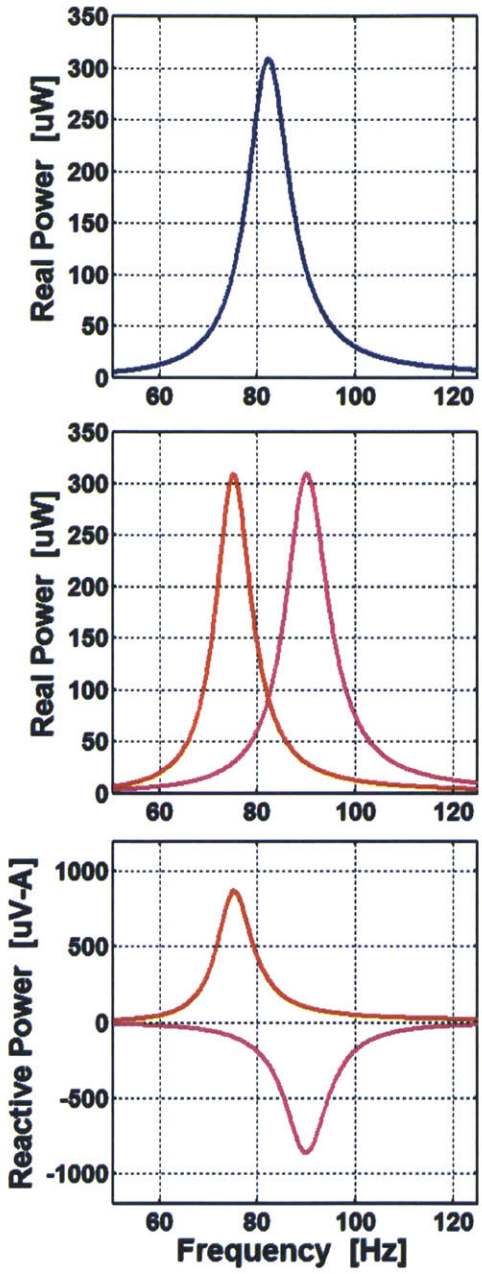

Figure 3-4: Resonant frequency shifting with reactive components. The blue curve at the top indicates the frequency response of the harvester loaded with the resistive matched 43.6 kΩ resistor. The bottom two figures indicate the real (middle) and reactive (bottom) power in the circuit with additional reactive loads. With an additional capacitor (14.4 nF) in series with R_L, the blue curve shifts to the purple curve and with an additional inductor (260 H) in series with R_L, it shifts to the red curve. In both cases, the non-zero reactive power appear. While the reactive power is not consumed in ideal reactive components, it causes losses when using real reactive components. The plot assumes constant acceleration through the frequency sweep.

Table 3.1: Piezoelectric Harvester Parameter

	Value	Units
Effective Mass M	2.2e-3	[kg]
Spring Constant k	18592	[N/m]
Damping Factor B	0.08	[N·s/m]
Conversion Ratio G	1.3e-3	[N/V]

two figures indicates the frequency response of the harvester loaded with the resistive matched 43.6 kΩ resistor. The bottom two figures indicate the real (bottom-left) and reactive (bottom-right) power in the circuits with reactive loads. With an additional capacitor (14.4 nF) in series with R_L, the blue curve shifts to the purple curve and with an additional inductor (260 H) in series with R_L, it shifts to the red curve. While the reactive power is not consumed in ideal reactive components, it should be noted that power losses exist when using reactive components.

Examining the reactive component sizes, one can notice that while the capacitor size (14.4 nF) can be implemented with off-the-shelf discrete components, the inductor size (260 H) presents a serious challenge to be built in a low-loss fashion. Another point worth noticing is the substantial frequency shift in Figure 3-4 compared to the window vibration spectrogram shown in Figure 1-1. This thesis addresses this issue with a power-switching circuit that changes the load current and voltage characteristics such that the load may appear as a large inductance or a more complex load. The simulation done in Figure 3-4 is based on the electrical characteristics of the Mide V25W piezoelectric harvester provided by Mide Technology[1]. Detailed modeling and characterization of the harvester is given in Chapter 5. Physical parameters of the piezoelectric harvester are shown in Table 3.1.

3.3.2 Multi-resonant Frequency

At the time of this thesis, there has yet to be any previous work on harvesting energy from simultaneous multi-frequency vibrations. The motivation of exploring into this area stems from the multi-frequency or multi-harmonic vibration characteristic commonly found in vibrations created by machinery and consumer electronics. As

[1] www.mide.com

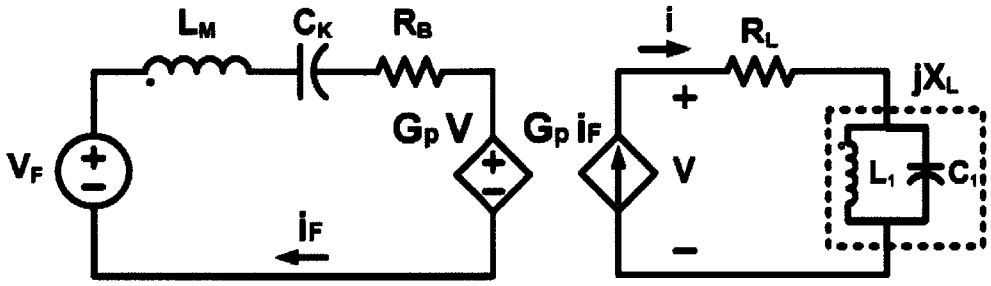

Figure 3-5: Equivalent circuit of a dual-resonance vibration energy harvester.

shown in the vibration spectrogram in Figure 1-1, each red line represents a target harmonic frequency where energy can be extracted. This section builds on the general matching conditions given in Equations 3.46 and 3.47, and gradually expands it from dual-resonance to triple-resonance to N-resonance energy harvesting.

Dual-resonant Frequency

Most vibration energy harvesters, disregarding non-linear or bi-stable structured designs, resonate at a single frequency with a high quality factor and hence small frequency band of operation. Therefore, in order for the harvester to load match at multiple frequencies without changing the physical structure of the harvester, one must create additional resonances with some kind of electrical load. One intuitive approach, which will be proven later to be highly effective, is to create an LC resonator at the electrical output as shown in Figure 3-5. Qualitatively speaking, the LC resonator created by L_1 and C_1 will create an additional resonance such that the energy harvesting system becomes a dual-resonance system capable of extracting energy at two frequencies. However, the two resonant frequencies are not simply $\sqrt{\frac{1}{L_M C_K}}$ and $\sqrt{\frac{1}{L_1 C_1}}$. This is due to the interaction between the mechanical and electrical systems, and can be better understood by going back to Equation 3.45, which is rewritten here for convenience as

$$P_L = \frac{\frac{1}{2} G_p^2 R_L |V_F|^2}{(\frac{1}{\omega C_K} - \omega L_M - G_p^2 X_L)^2 + (R_B + G_p^2 R_L)^2} \tag{3.56}$$

From Section 3.2, it is understood that the matched loading is determined in part by

$$\frac{1}{\omega C_K} - \omega L_M - G_p^2 X_L = 0 \tag{3.57}$$

This is the reactive component of load matching for maximum power transfer. The load reactance X_L here is the equivalent impedance of L_1 and C_1 in parallel

$$X_L = \frac{L_1}{1 - \omega^2 L_1 C_1} \tag{3.58}$$

By substituting Equation 3.58 into Equation 3.57, and solving for ω, one can find the two load-matched frequencies. To get a better visual idea of the dynamics, Equation 3.57 is plotted on the bottom figure of Figure 3-6. The blue line indicates the mechanical reactive impedance of the harvester. Its intersection with the red curve, which represents X_L, is the location of the two resonant frequencies. There are three extra points worth pointing out. First, the zero crossing of the blue curve is the original resonant frequency ($\sqrt{\frac{1}{L_M C_K}}$) of the harvester. This shows that the new resonant frequencies are not simply the respective resonant frequencies of the two LC tanks. The second point is the plus infinity to minus infinity segment of the red line is the pole created by L_M and C_K. It is a fictitious line and an artifact of MATLAB, and therefore, the intersection with the red line at this segment does not create an additional resonant frequency. Finally, the peak power at the load-matched frequencies are identical due to the constant matched resistive load R_L in Equation 3.47.

The output power frequency response under constant acceleration, is shown in the top figure of Figure 3-6. The entire simulation was done in MATLAB (Appendix A.1.2) and also based on the Mide V25W harvester. Circuit parameters used are as the following: $R_L = 43.6\ k\Omega$, $L_1 = 500$ H and $C_1 = 4.5$ nF. The two additional reactive components L_1 and C_1 create an additional resonant frequency and creates a dual-resonant energy harvesting system. It should be noted that while the reactive power shown in the bottom-right figure of Figure 3-6 is not consumed in ideal reactive components, it causes losses when using reactive components with losses.

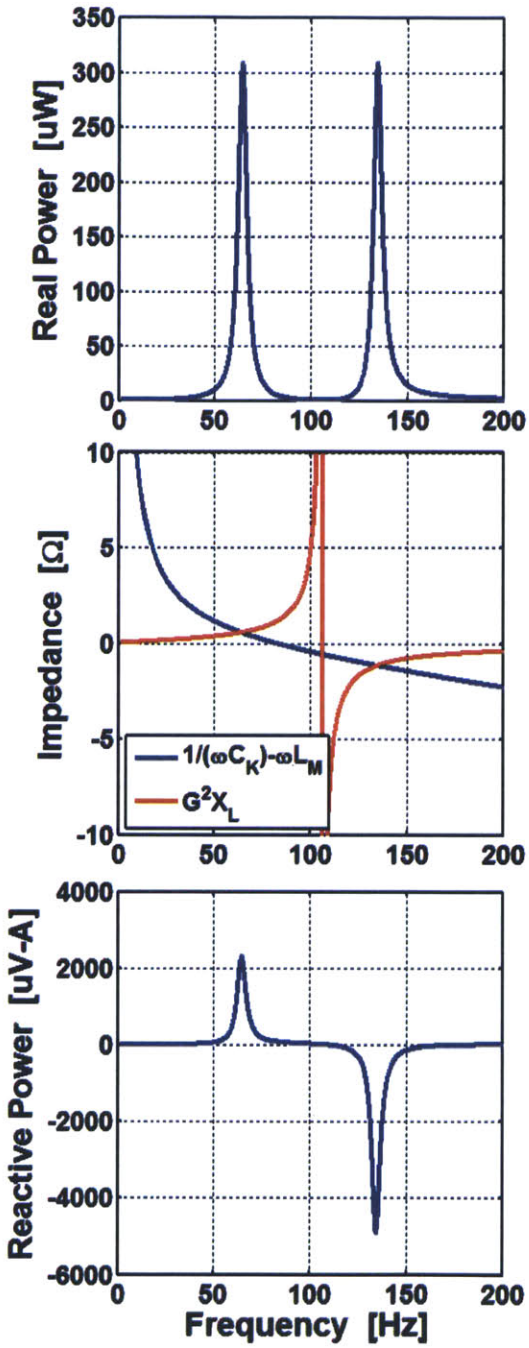

Figure 3-6: The blue curve at the top indicates the dual resonance nature of the LC loaded harvester. In the middle figure, the blue curve represents the internal reactive impedance of the harvester and the red curve indicates the load reactive impedance X_L. The bottom figure indicates the reactive power being exchanged in the circuit. While the reactive power is not consumed in ideal reactive components, it causes losses when using real reactive components. Simulation was carried out under constant acceleration of 0.7 g.

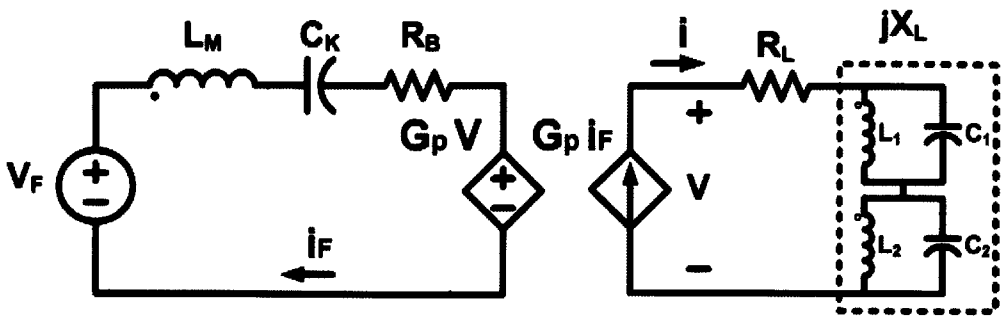

Figure 3-7: Equivalent circuit of a triple-resonance vibration energy harvester.

Triple-resonant Frequency

A triple-resonant energy harvesting system can be built upon the dual-resonant system developed in the previous section by adding an additional resonant frequency to the dual-resonant system. This can be achieved by building two LC resonators in series as shown in Figure 3-7. The two resonators will create two poles located at

$$\omega_{P1} = \sqrt{\frac{1}{L_1 C_1}} \tag{3.59}$$

$$\omega_{P2} = \sqrt{\frac{1}{L_2 C_2}} \tag{3.60}$$

which is shown in the red curve of the bottom figure of Figure 3-8. The MATLAB code can be found in Appendix A.1.3. It should be pointed out that these two poles are simply the poles of the electronics and the actual resonant frequency of the harvesting system lies at the intersections between the red curve and the blue curve. The zero crossing of the blue curve represents the original mechanical resonant frequency. Circuit parameters used are the following: $R_L = 43.6\ k\Omega$, $L_1 = 500$ H $C_1 = 4.5$ nF, $L_2 = 500$ H and $C_2 = 2.5$ nF. As required in Equation 3.47, the optimal load impedance R_L remains constant at 43.6 $k\Omega$ and only depends on the mechanical damping R_B and transformation ratio G_p. The peak power being delivered to the load also remains constant as shown in the top figure of Figure 3-8 and does not change with additional resonant frequencies. The simulation also assumes constant

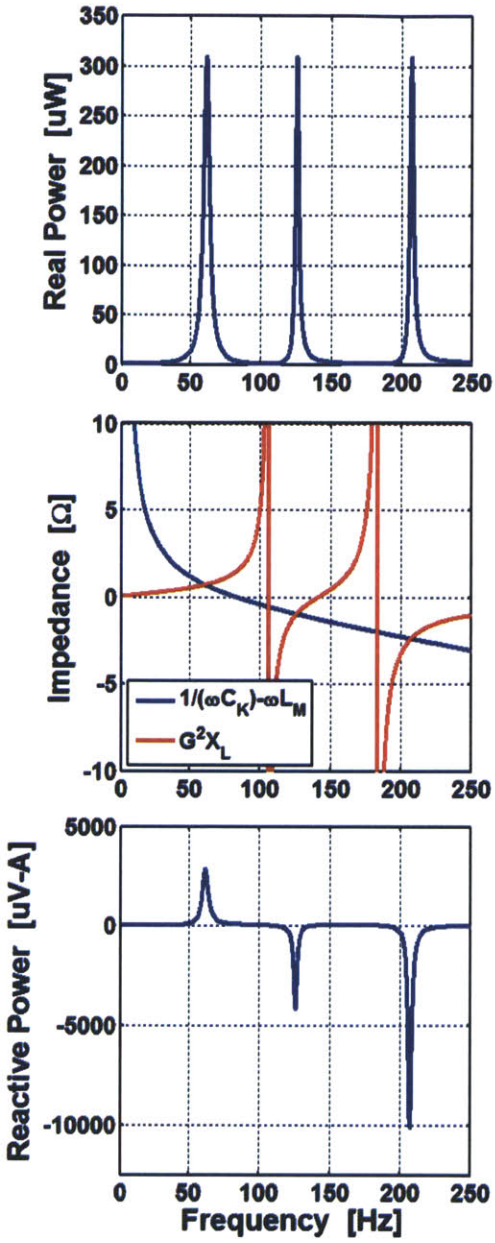

Figure 3-8: The blue curve at the top indicates the triple resonance nature of the LC loaded harvester. In the middle figure, the blue curve represents the internal reactive impedance of the harvester and the red curve indicates the load reactive impedance X_L. The bottom figure indicates the reactive power being exchanged in the circuit. While the reactive power is not consumed in ideal reactive components, it causes losses when using real reactive components. Simulation was carried out under constant acceleration of 0.7 g.

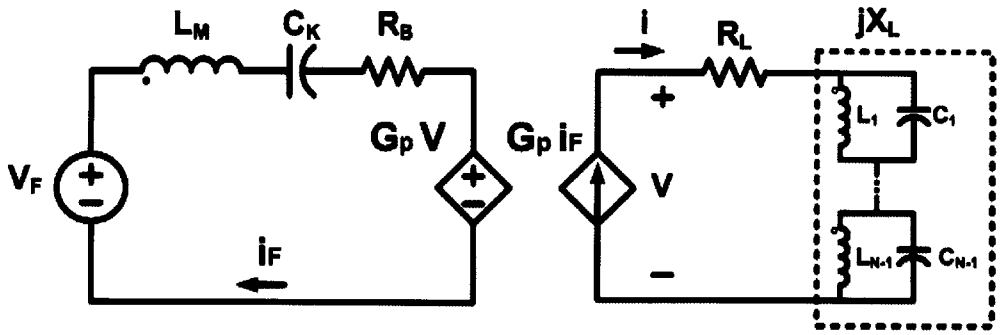

Figure 3-9: Equivalent circuit of a N-resonance vibration energy harvester.

acceleration at 0.7 g. It again should be noted that while the reactive power shown in the bottom-right figure of Figure 3-8 is not consumed in ideal reactive components, it causes losses when using reactive components with losses.

N-resonant Frequency

As expected, the general load circuit schematic for a N-resonant frequency harvester is shown in Figure 3-9 with $(N-1)$ LC tank circuits in series. These circuit are unrealistic to be built with real reactive components, but can all be synthesized with switching power electronics. The one challenge with more and more additional resonances is how to maintain reasonable individual bandwidth for each resonant peak especially for the resonances located in the middle. The resonances on the two sides normally have larger bandwidths due to the fact that the load reactance acts as an equivalent inductor and capacitor at the lowest and highest resonant frequency respectively.

3.4 Chapter Summary

This chapter built the theoretical backbone of impedance matching for multi-frequency vibration energy harvesting. It began with an introduction on the spring-mass-damper model and the equivalent circuit model developed in previous works, and evolved toward finding the optimal impedance for more general vibration conditions.

These include single resonant frequency tuning, dual resonant frequency, triple resonant frequency and finally N-resonant frequency energy harvesting. An interesting phenomenon to be noted is that while the optimal reactance changes for different situations, the optimal resistance remains constant and only depends on the mechanical damping and the electromechanical conversion ratio.

As mentioned multiple times in this chapter, the required reactive components, particularly the inductors, are too large to be implemented with real devices with today's technology and should be synthesized with power factor correction (PFC) power electronics. Details of the architecture, design, and simulation results of the power electronics are shown in the following Chapter.

Chapter 4

Power Electronics

With the theoretical derivations in the previous chapter, it was shown that reactive loading components opened the possibility of harvester tuning and creating additional resonant and load-matching frequencies. However, the large required inductor sizes make them inefficient and hence impractical to be implemented with real reactive components. A possible solution that was proposed is the idea of a power electronics architecture that mimics the voltage and current characteristics of a large reactive component or even more complex impedances. This chapter provides the architecture and design details of the proposed power electronic framework.

The chapter begins with an overview of the previous works conducted by other researchers in the area of energy harvester interfacing power electronics. In the next section, the high level system architecture of the proposed H-bridge power factor correction circuit is outlined. Design details of the power stage and control loop are given in the following sections. At the end of the chapter, a power loss calculation of the printed circuit board version is presented. In addition, the power estimation of a integrated version is also given. It shows great promise.

4.1 Previous Work

The basic idea of the architecture of our power electronics stems from the idea of unity power factor circuits and impedance matching theory. Details of the impedance

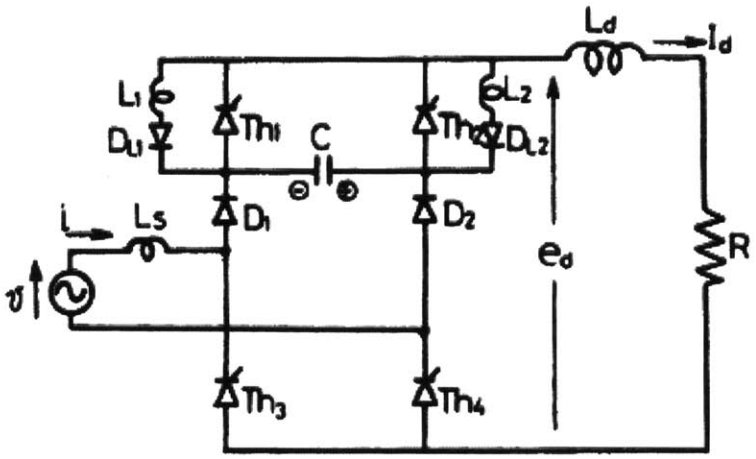

Figure 4-1: Typical unity power factor circuit [6].

matching theory were given in Chapter 3. A unity power factor circuit synthesizes a resistive load with power electronics at the electrical terminals even though a resistor is not present. Our proposed power electronics expands this idea such that more complex loads such as inductors, capacitors and even LC tanks can be synthesized. This electrical load synthesizing circuit enables the frequency tuning and additional resonance creation of energy harvesters. In addition, we will also take a look into the bias-flip inductor concept [7], which has garnered significant research interest in recent years.

4.1.1 Unity Power Factor Circuits

In the 1980s the power electronics community developed utility/dc interfaces that draw a nearly perfect phase-matched sinusoidal current from the utility [19]. These harmonic-free and reactive-power-free interfaces were first conceived as a way to deal with the distortion problems that a large number of conditioned loads and sources would otherwise create. The US Department of Energy (DOE), through its photovoltaic program, was a major promoter of this work, and several of its sponsored projects demonstrated the ability to achieve a total harmonic distortion of five percent or less.

The computer industry was similarly contemplating the use of the harmonic-free

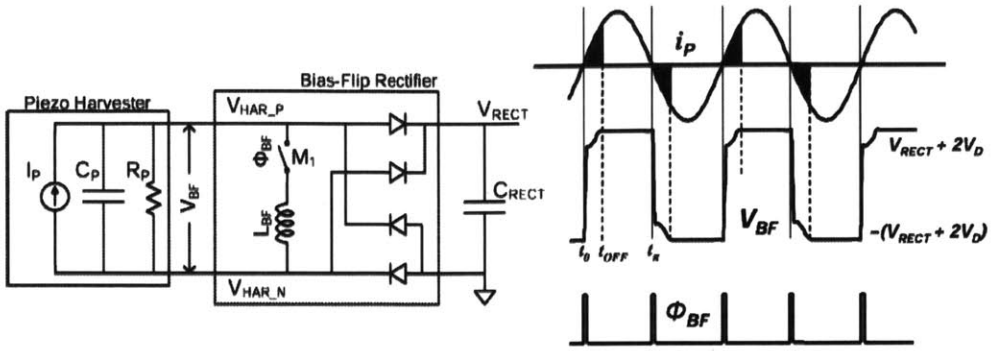

Figure 4-2: A bias-flip rectifier circuit and its associated current and voltage waveforms [7].

interface. It was viewed primarily as a way to extract more power from a standard wall outlet rather than as a solution to a governmental standard that might someday exist. The harmonic-free interface, known as unity-power factor circuits, achieved a power factor very close to unity without significant harmonics and, therefore, permitted a substantial increase in the amount of computing power that can be installed for a given utility service.

As shown in Figure 4-1, these circuits normally consisted of an H-bridge (full-bridge) rectifier while the switches are controlled such that the load voltage and current are kept in phase and hence delivering the maximum power to the load.

4.1.2 Bias-flip Inductors

Ramadass *et al* [7] designed a bias-flip rectifier circuit that could improve the power extraction capability from piezoelectric harvesters over conventional full-bridge rectifiers and voltage doublers by greater than a factor of 4. The inductor used within the bias-flip rectifier was also shared efficiently with a multitude of switching DC-DC converters within the system which ultimately reduced the overall component count. Figure 4-2 shows the circuit implementation of the bias-flip rectifier. Compared to the switch-only rectifier, an additional inductor (L_{BF}) is added in series with the switch M_1. An inductor can passively flip the voltage across a capacitor. So instead of just using a switch, the bias-flip rectifier utilizes an inductor to flip the voltage across C_P.

The voltage and current waveforms associated with this circuit are shown in Figure 4-2. At every half-cycle, when i_P changes direction, the switch M_1 is turned ON briefly to allow the inductor to flip the voltage across C_P. The switch is turned OFF when the current in the inductor reaches zero. If the current flow path in the L_{BF}, C_P network were ideal, the voltage flipping would be perfect. However, the resistances along this path limits the magnitude of the voltage inversion as shown in Figure 4-2. Now, the piezoelectric current only has to charge up C_P from the flipped voltage to $\pm(V_{RECT} + 2V_D)$ before it can flow into the output. This significantly reduces the amount of charge lost. This way the majority of the charge available from the harvester can go into the output capacitor without having to charge or discharge C_P. To derive the amount of output power extractable using a bias-flip rectifier, it is assumed that the resistance along the L_{BF}, C_P path is R_{BF}. This resistance includes the parasitic resistance of the inductor, the switches in series with the inductor and the series resistance along the piezoelectric harvester.

The bias-flip rectifier architecture and the unity power factor inspired architecture were both closely studied and evaluated at the beginning of this thesis. While the bias-flip rectifier presented significant benefits in the implementation of large inductors, it is much harder for the architecture to implement more complex impedances such as the parallel LC tanks shown in Chapter 3. The unity power factor inspired architecture, on the other hand, gives great flexibility in terms of impedance tuning and the possibility of multi-harmonic system implementations. Therefore, the unity power factor architecture was chosen as the basis of our power electronics framework.

4.2 System Architecture

The power-electronic switching circuit used here is inspired by power factor correction (PFC) circuits [19], commonly applied in high-power utility/dc interfaces to make the load current and voltage in-phase. In other words, creating a resistive load with power electronics such that the maximum amount of real power is delivered to the load. The goal here, however, is to make the load current and voltage achieve a more complex

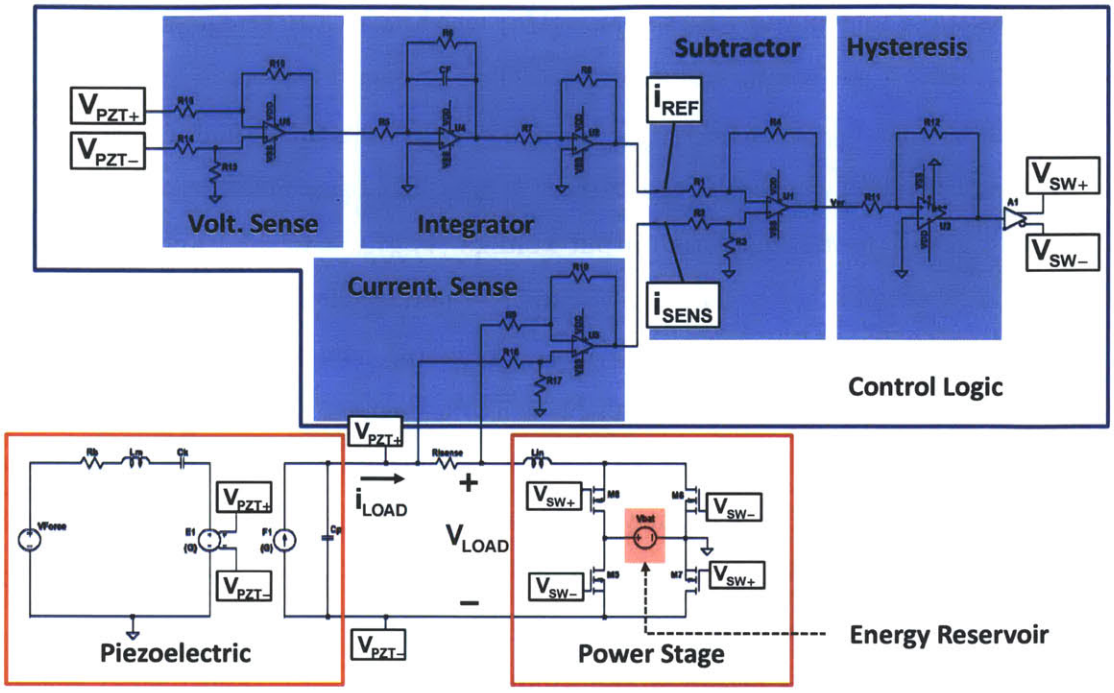

Figure 4-3: System overview of the tunable loading electronics and energy harvester.

relation such that the power electronics present a complex impedance load to the harvester. Analyses in previous research has shown that proper electrical loading can improve system performance [17] [20] [5] [51]. In [20] it is shown that such loading can be implemented with switching power electronics.

The system architecture of our circuit is shown in Figure 4-3. The circuit itself consists of two parts - the power stage (red box) and the control logic (blue box).The orange box shown in Figure 4-3 is the equivalent circuit model of a piezoelectric harvester, which can be replaced with a magnetic or electric harvester model depending on the application.

Without diving into the circuit design details at this point, let's begin with the power flow of the circuit. The kinetic vibration energy is first transduced through the piezoelectric harvester into electrical energy. This electrical power is then delivered to the power stage which synthesizes a complex load such that the output power from the piezoelectric harvester can ultimately be stored in the battery which serves as the energy reservoir. Now, let's take a closer examination of each block. The power

stage consists of four power FETs ($M6 - M8$) which form a H-bridge, a DC voltage source V_{bat} and a smoothing inductor L_{in}. The H-bridge FET configuration makes the voltage across L_{in} to be ($V_{LOAD} \pm V_{bat}$). By controlling the inductor current, the power stage effectively controls load current i_{LOAD}. The basic function of the control logic is to sense the piezoelectric output voltage ($V_{PZT+} - V_{PZT-}$) and determines the reference current I_{REF} that corresponds to the desired loading at that voltage. The reference and actual currents I_{SENS} are compared, and the difference is passed through a hysteresis block to generate the switching signals V_{SW+} and V_{SW-} for the four-FET bridge in the switching network. The control loop in Figure 4-3 is for a inductive or RL load. If a capacitive load is desired, the integrator in the control loop must be replaced with a differentiator. The analog control loop implemented here is meant to be a demonstration of this impedance tuning architecture. A digital control implementation is preferred and could provide easier tunability, more diverse functionality and reduced power consumption.

The major improvement of the electronics in Figure 4-3 compared to previous work [20] is its large inductance implementation capability. This circuit can generate the load voltage-current characteristics of a 30 H inductor. This greatly decreases the power losses and provides dynamic tunability of the complex load. In the following subsections, we will give more details of how different electrical impedances can be synthesized with the same basic architecture. It will start with the simple resistive load, continuing to reactive loads, and end with complex LC tank circuits.

4.2.1 Resistive Load Synthesis

Before implementing large reactive components with the power electronics, the first step was to use the power electronics architecture to synthesize a resistive load, which is effectively doing unity power-factor correction (PFC). By taking out the integrator in the control loop shown in Figure 4-3, a circuit as shown in Figure 4-4 can synthesize a resistor. The desired load current is generated in the control logic and enforced through the hysteresis control that switches the H-bridge.

Figure 4-5 shows the load voltage (V_{LOAD}), load current (i_{LOAD}) and switching

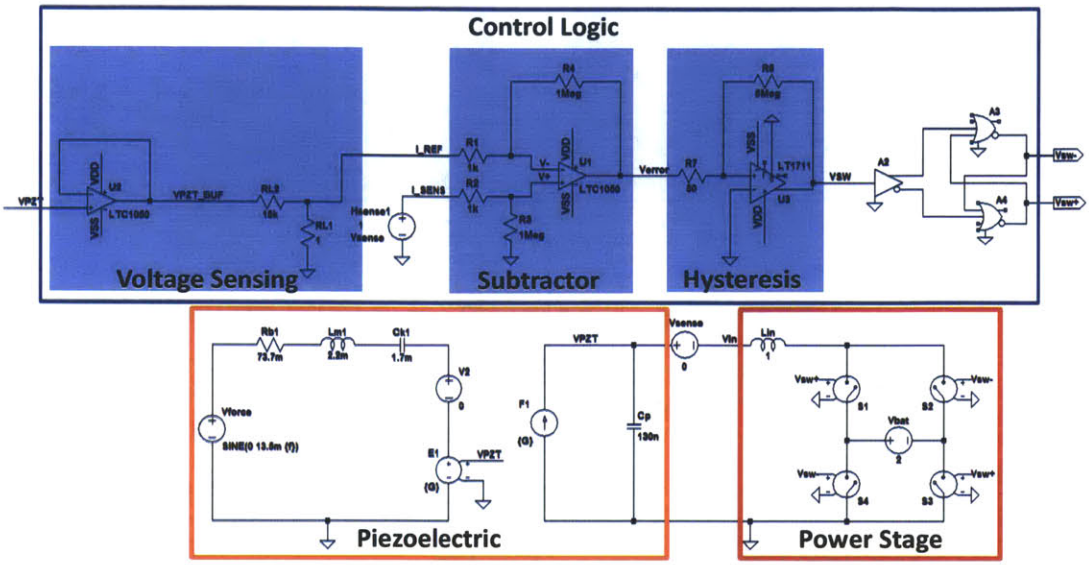

Figure 4-4: Simplified circuit architecture that synthesizes resistive load.

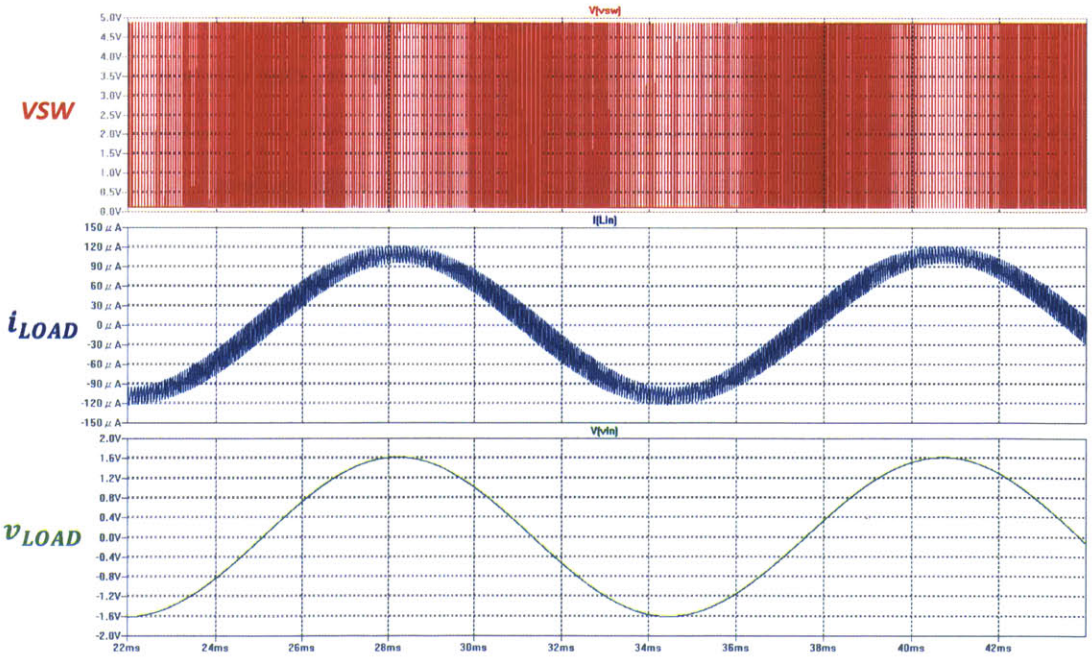

Figure 4-5: SPICE simulated load voltage and current waveforms of a 13.3 kΩ resistor synthesized with proposed power factor correction circuit.

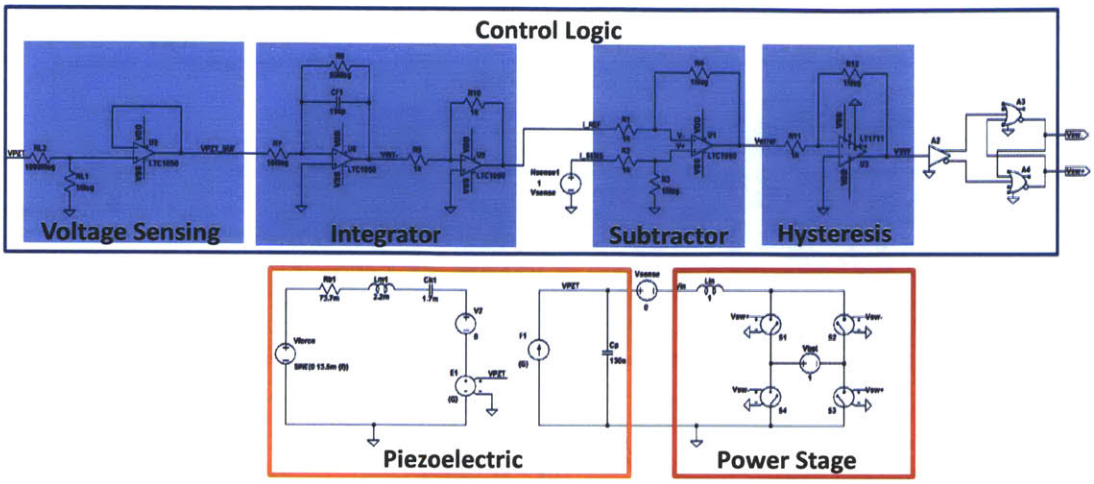

Figure 4-6: Simplified circuit architecture that synthesizes inductive load.

(VSW) waveforms of a synthesized 13.3 kΩ resistor simulated in LTspice. In the figure, it can be observed that V_{LOAD} and i_{LOAD} are in phase, confirming that the average load impedance is resistive. This implies that the output power from the piezoelectric harvester is effectively delivered to the power stage and stored in the battery V_{bat}. Second, the current ripple of i_{LOAD} can be clearly seen. As mentioned in the previous section, the load current ripple is due to the alternating voltage ($V_{LOAD} \pm V_{bat}$) across the smoothing inductor. While, V_{bat} remains constant, V_{LOAD} is an AC voltage and hence causing the current ripple slope and the switching frequency to change with time. This effect can be observed in the top figure of Figure 4-5.

4.2.2 Inductive Load Synthesis

In the previous section, we successfully synthesized a resistor with the proposed power electronics. The circuit is essentially a reproduction of a unity power factor circuit using a hysteresis current control. However, it served as a confidence builder for the more complex load impedances in the following sections. This section will introduce the implementation of an inductive load. Looking at the load voltage and current relationship, an inductive load requires the load voltage to lead the load current by a phase difference of 90 ° and therefore, the control logic in the power electronics needs to create a 90 ° phase difference.

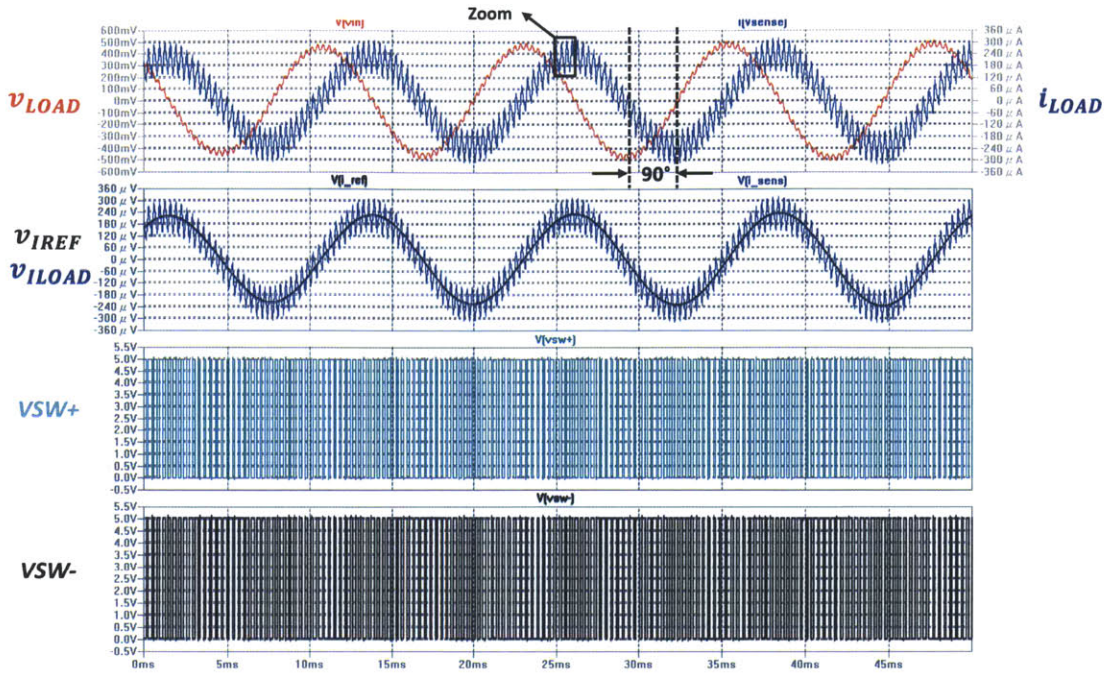

Figure 4-7: SPICE simulated load voltage and current of a 4 H inductor synthesized with proposed power factor correction circuit.

A simplified version of an inductive load version of the power electronics is shown in Figure 4-6. Comparing it to the resistive load version shown in Figure 4-4, there is an additional integrator block embedded inside the control logic. The reason behind this is due to the design of the control logic. As described in the beginning of this section, the control logic senses the piezoelectric output voltage and generates the desired load reference current. Therefore, an integrator would effectively delay the reference current by 90° and create an equivalent inductor at the output of the piezoelectric harvester. Figure 4-7 gives a good illustration of the load voltage, load current and switching waveforms of the synthesized inductor circuit. The first thing that can be noticed is that the load voltage leads the load current by 90°, indicating that the synthesized load is indeed an inductive load. Next, from Figure 4-8, we can find the average magnitudes of the load current and voltage to be 240 μA and 480 mV respectively. Since the resonant frequency of the piezoelectric harvester is 82 Hz, we can find that the synthesized inductor to be 4 H.

A common confusion that is often encountered is the relationship between the

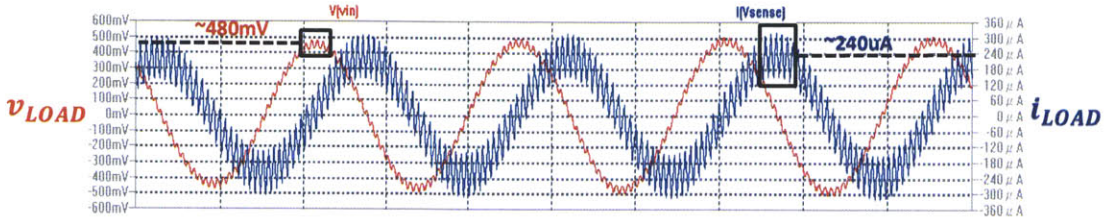

Figure 4-8: SPICE simulated average value of load current and voltage. From these values, it can be shown that the synthesized inductor is 4 H.

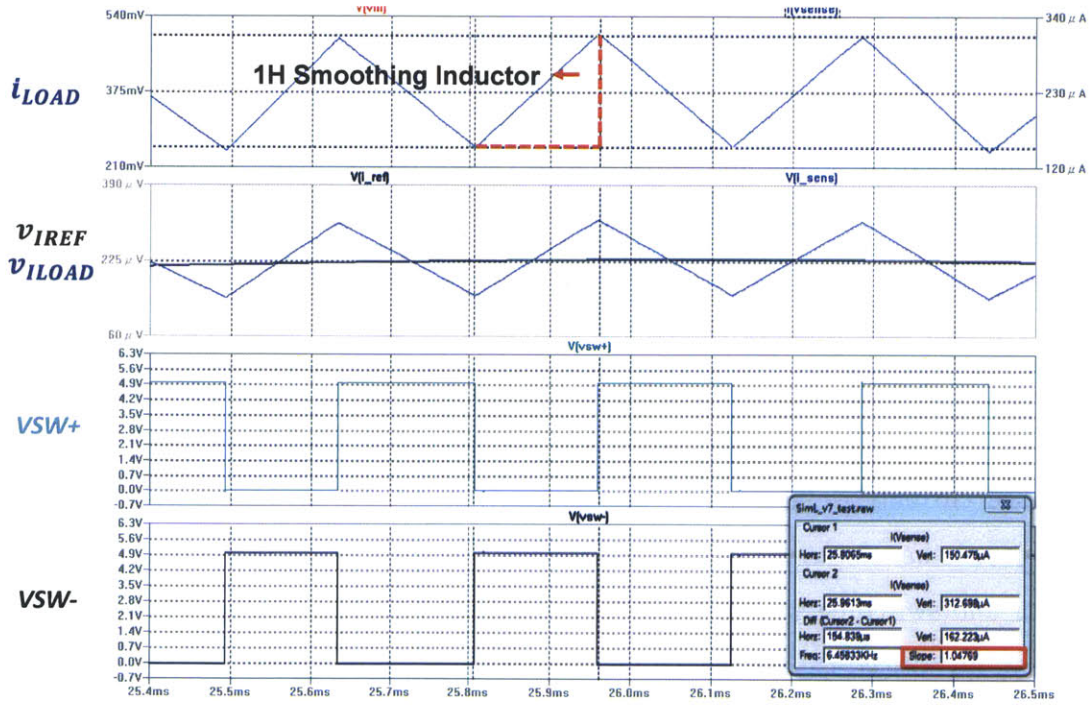

Figure 4-9: SPICE simulated zoomed-in view of the load voltage and current of a 4 H inductor synthesized with proposed power factor correction circuit.

synthesized and smoothing inductor. The synthesized inductor is a non-physical inductor created by the power electronics and can be observed through the load current and voltage relationships. The smoothing inductor, on the other hand, is a physical inductor inside the power electronics. It controls the load current along with the H-bridge switches such that the desired impedance, in this case an inductor, is synthesized. The impact of the smoothing inductor can be observed by looking at the load current ripple as shown in Figure 4-9. By measuring the slope of the current ripple and knowledge of the voltage across the smoothing inductor, the size of the smoothing inductor is confirmed to be 1 H.

In this section, a 4 H inductor was successfully implemented with our power electronics. Since the power electronics contains a smoothing inductor of 1 H, it can be viewed that the power electronics effectively amplified the inductor by 4x. From additional simulations, there are no fundamental limits as to how large of an inductor can be created using this topology. However, it should be kept in mind that the synthesized inductor will always be limited by the series resistance of the smoothing inductor. For the 1 H smoothing inductor used in this circuit, the series resistance was 85 Ω. The inductor used here was the RL-1123 inductor provided by Renco Electronics.

4.2.3 Capacitive Load Synthesis

In this section, a capacitor is successfully synthesized using the proposed power electronics circuit. The circuit architecture is shown in Figure 4-10. Comparing the capacitive circuit in Figure 4-10 and the inductive circuit in Figure 4-6, the difference lies in the control logic where the integrator in the inductor synthesizer circuit is replaced with a low-pass-filter and a differentiator in the capacitor synthesizer circuit. The differentiator is utilized in the capacitor synthesizer circuit to generate the reference load current from the load voltage since the current of a capacitor leads its voltage by 90°. An additional low-pass filter is required here to filter out the high-frequency load voltage ripples such that they do not get amplified through the differentiator.

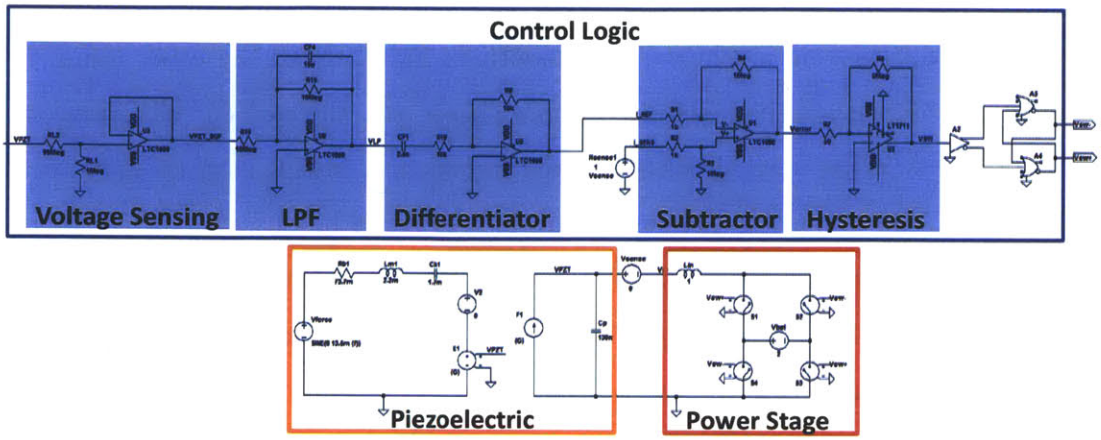

Figure 4-10: Simplified circuit architecture that synthesizes capacitive load.

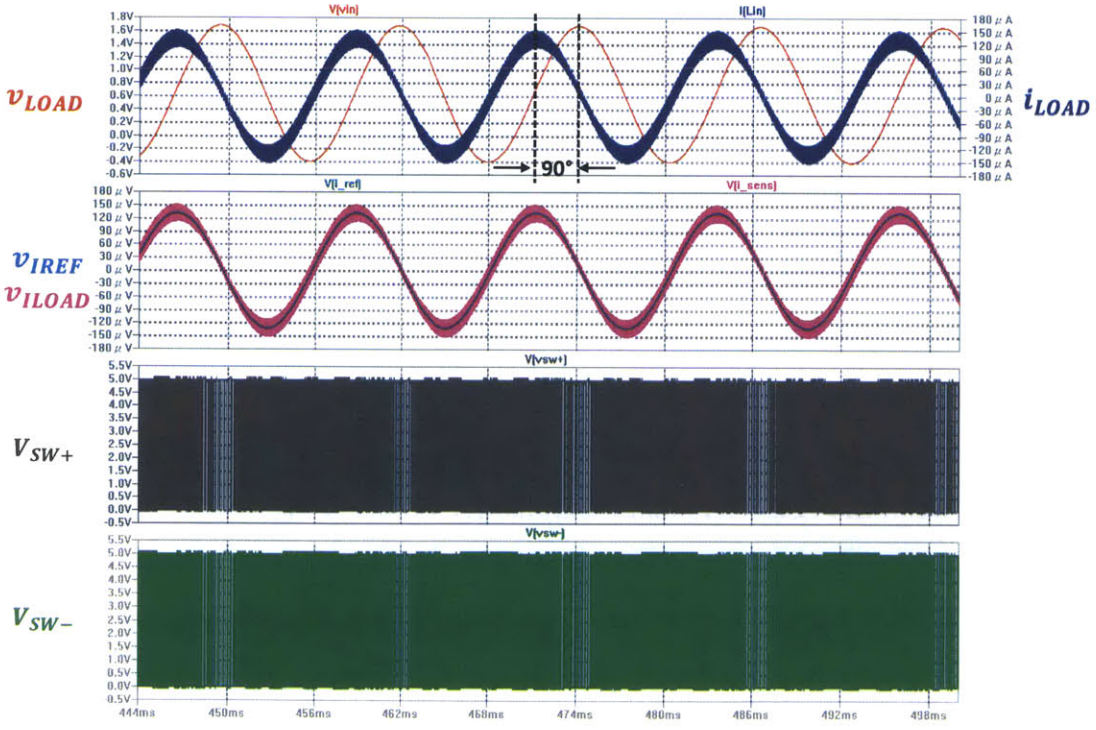

Figure 4-11: SPICE simulated load voltage and current of a 25 F capacitor synthesized with proposed power factor correction circuit.

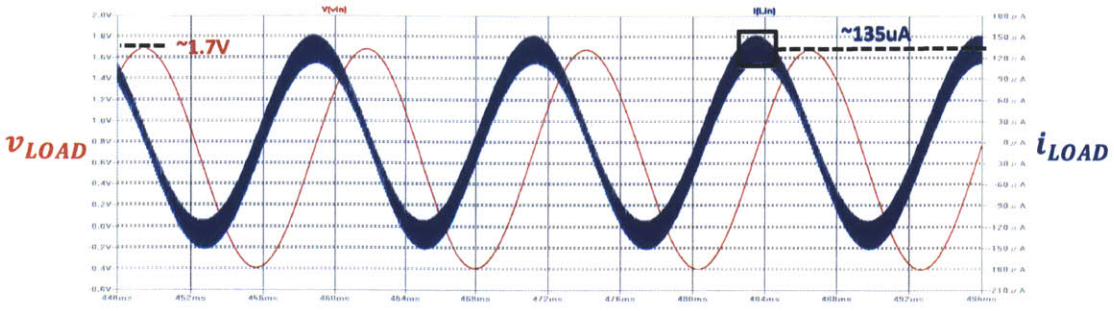

Figure 4-12: SPICE simulated average value of load current and voltage. From these values, it can be shown that the synthesized inductor is 25 F.

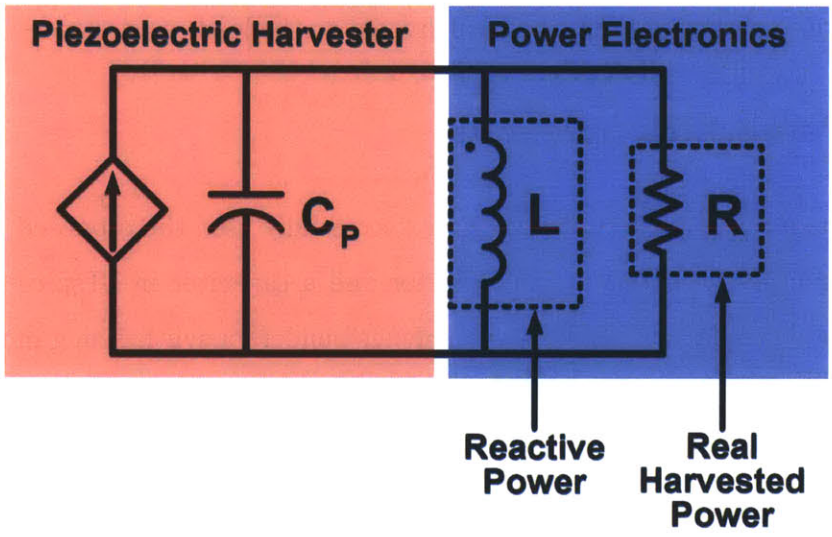

Figure 4-13: Piezoelectric harvester loaded with a impedance consisting of a resistor and inductor in parallel.

The load voltage v_{LOAD}, load current i_{LOAD}, reference current i_{REF} and switching waveforms V_{SW+} and V_{SW-} are shown in Figure 4-11. It is clear from the top two waveforms in Figure 4-11 that i_{LOAD} leads v_{LOAD} by 90° and closely modulates around the reference current i_{REF}. The size of the capacitor being synthesized is 25 F. It is shown in Figre 4-12 by measuring the magnitudes of v_{LOAD} and i_{LOAD}.

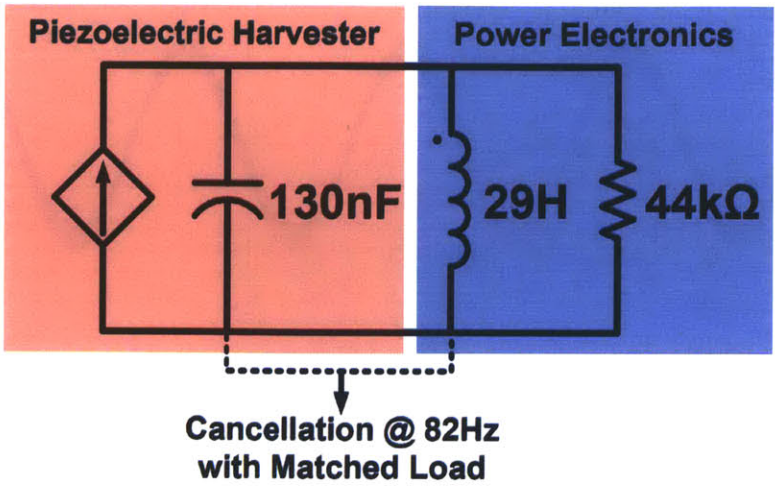

Figure 4-14: Schematic of piezoelectric harvester with matched impedance at resonance. The load inductor cancels the parasitic capacitor at resonance and enables the maximum amount of power being delivered to the load resistance.

4.2.4 Parallel-RL Synthesis

In the previous three subsections, we have successfully used the proposed power electronics to synthesize a resistor, an inductor and a capacitor in LTspice simulation. The successful simulations serve as a confidence builder for synthesizing more complex loads. As we recall from Section 3.3, in order to achieve frequency tuning or create additional resonant frequencies, complex loads with large inductors were required. In this subsection, we will synthesize a parallel-RL circuit as shown in Figure 4-13. For a piezoelectric harvester, having a parallel-RL load has two possible benefits. First, the inductor with the right size could cancel the parasitic capacitance at the resonant frequency and fulfill the piezoelectric harvester's maximum energy transfer potential. For the V25W piezoelectric harvester which has a 130 nF parasitic capacitance and 82 Hz resonant frequency, it requires a 29 H parallel inductor to cancel the parasitic capacitance. The matching resistor size is 44 kΩ. The second potential benefit of this circuit is the capability of creating a second resonance by changing the inductor size. This second resonance enables the energy harvester system to harvest energy from two vibration frequencies at the same time.

Consider next Figure 4-14 to get a better physical understanding of the circuit.

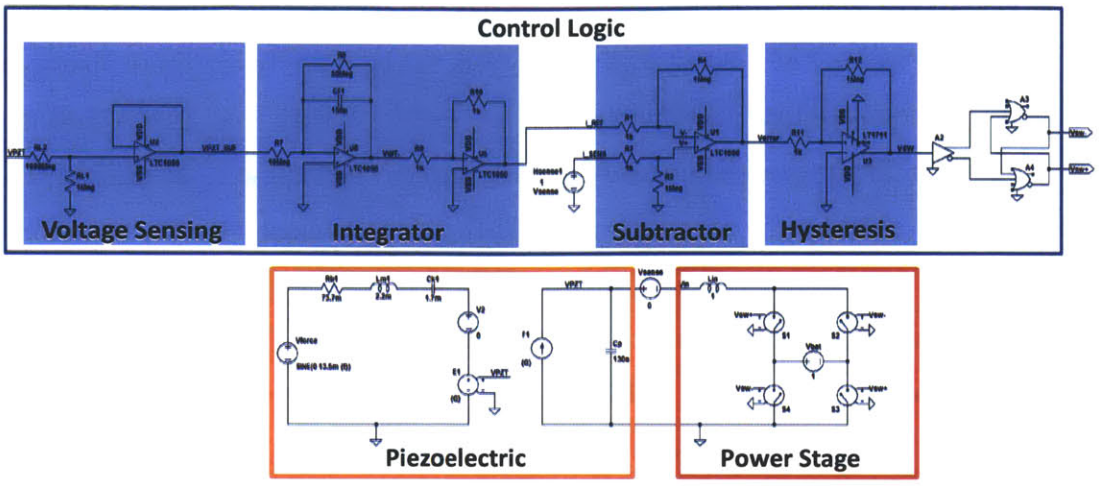

Figure 4-15: Simplified circuit architecture that synthesizes a parallel-RL load.

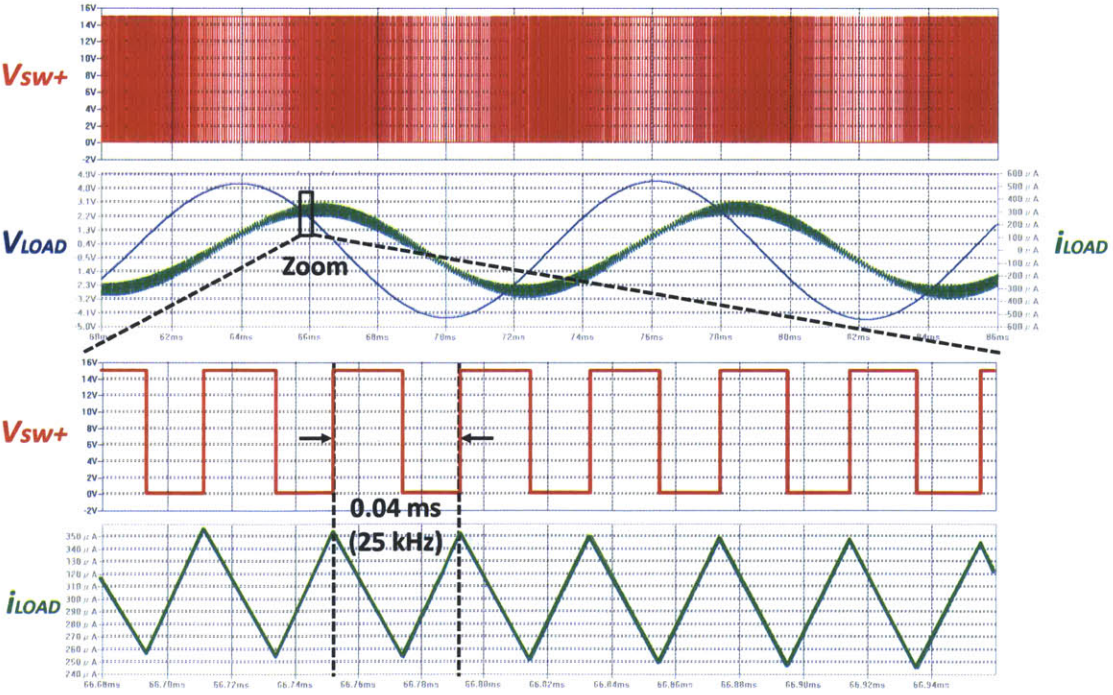

Figure 4-16: Waveforms of the synthesized parallel RL circuit

The resistor and inductor in the circuit are fictitious and are synthesized using the power electronics shown in Figure 4-15 which has the same architecture but different circuit parameters in the control logic compared to the power electronics that synthesized the inductive load in Figure 4-6. The reactive energy that passes into and out from the inductor is actually stored in the battery of the power electronics. The real power absorbed by the resistor is actually the harvested energy and is all stored in the battery.

SPICE-simulation waveforms of the parallel-RL (R = 44 kΩ, L = 29 H) synthesized with power electronics are shown in Figure 4-16. As shown in the high-level schematic of Figure 4-14, this synthesized parallel-RL circuit cancels out C_p at 82 Hz and enables maximum power transfer to the electrical load for a matched load of 44 kΩ. It is important to note that the energy delivered to the equivalent resistor is physically delivered to the reservoir/supply V_{bat} connected to the FET bridge, and that the same reservoir supplies the reactive energy of the equivalent inductor. As expected, the load voltage V_{LOAD} leads the load current i_{LOAD} as shown in Figure 4-16. Also shown in Figure 4-16 is the zoomed view of i_{LOAD} and one of the switching signals V_{SW+}. The load current ripple created by the smoothing inductor L_{in} is observed in the zoomed in view.

4.3 Circuit Block Design

In this section, design details of the power stage and control logic of the proposed power electronics are given. The power stage consists of the smoothing inductor, the power FETs and the gate drivers. The control logic on the other hand includes the voltage sensing, reference current generation, current sensing and hysteresis control.

4.3.1 Power Stage

The first major challenge for the power stage is the smoothing inductor. From the LTspice simulations, it was found that a 1 H inductor was needed in order to provide the appropriate ripple current for the current control. With large inductors, the

largest challenge comes from its large DC resistance. For energy harvesting applications, this becomes more troublesome since the harvested energy is normally quite small and hence any large resistance in the power path will dissipate a significant amount of energy. After surveying commercial parts and the possibility of building the inductor in house, a commercial inductor provided by Rencoh Electronics[1] was chosen. The 1 H inductor made by Rencoh Electronics displayed an 85 Ω DC resistance which translates into a power loss of 0.3 μW when the output power is 300 μW and output voltage is 5 V. This power lost in less than 0.1 % of the output.

The second part of the power stage is the power FETs. The FDV301N digital nMOS provided by Fairchild Semiconductor[2] was chosen due to its low on-state resistance of 5 Ω and low input capacitance of 9.5 pF. In addition, it can withstand a drain-to-source voltage of 25 V. This is necessary for multi-frequency harvesting since the output voltages add up when multiple vibration frequencies excite the harvester at the same time. The final part of the power stage is the gate driver. Since the output power will be delivered to a 5 V DC reservoir, a high-side gate driver is required. The LTC4446[3] gate driver was chosen since it contains both a high-side and low-side gate driver with on-chip timing non-overlapping functions. Two LTC4446 chips were utilized to drive the four power FETs inside the H-bridge. The SPICE model for the LTC4446 were provided by Linear Technology and simulated in LTspice. From a performance point of view, the LTC4446 gate driver is an overkill for the FDV301N FETs, but was chosen due to its ability to drive both the high and low side FETs and to drive the high-side FET with 5 V source voltage. A more matched gate driver can be implemented with a custom made integrated gate driver and FET.

4.3.2 Control Logic

For the control logic, a high accuracy, low offset operational amplifier is required throughout the analog control logic because high accuracy voltage sensing and current

[1]http://www.rencousa.com/
[2]http://www.fairchildsemi.com/
[3]http://www.linear.com/product/LTC4446

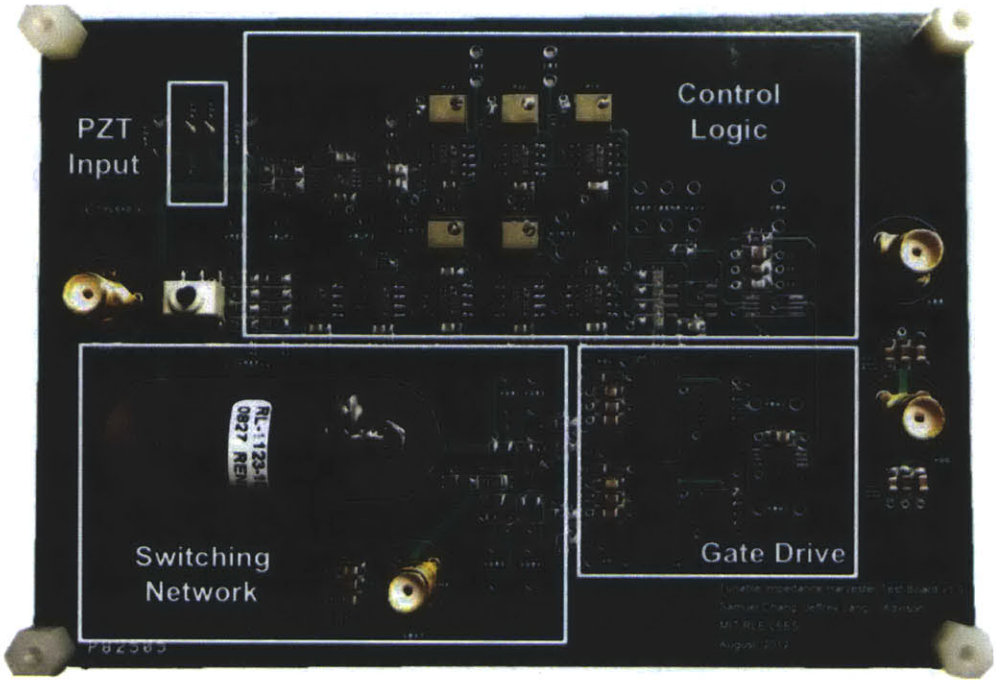

Figure 4-17: Harvester interfacing circuit that synthesizes a parallel RL circuit on a printed circuit board.

sensing are required. The LTC1050[4] high precision operational amplifier is widely used in the control loop to increase the control accuracy. It is a high performance, zero-drift operational amplifier with an offset voltage os 0.5 μV and input noise voltage of 1.6 μV_{P-P}.

For the hysteresis control, the LT1711 rail-to-rail comparator is used to create a hysteresis switching threshold of 5 mV. The size of the hysteresis threshold controls the frequency of the switching while the inductor size and the load DC voltage controls the current ripple slope.

4.4 Printed Circuit Board Design

The full circuit implemented on a printed circuit board is shown in Figure 4-17. The electrical output from the piezoelectric harvester comes in from the upper-left pins and goes through the switching network in the bottom-right. As shown in the switching

[4]http://cds.linear.com/docs/en/datasheet/1050fb.pdf

network box in Figure 4-17, the black round tube is the 1 H smoothing inductor provided by Renco Electronics. The four FDV301N transistors in the H-bridge are closely laid out to the right of the smoothing inductor to shorten the power path.

The two LTC4446 gate drives are placed right next to the transistors to the right. A 5-tap delay line chip, DS1100[5], is added in front of the gate drive to ensure timing synchronization between the two gate drives. The top part of the board is mainly the control logic consisting of operational amplifiers and comparators. The LTC1050 high precision operational amplifiers are widely used in the control loop to increase the control accuracy. Potentiometers are also used in place of fixed value resistors to increase the tunability of the control loop. A mechanical switch, shown to the left of the control logic box in Figure 4-17, is added to the control loop to switch between the piezoelectric harvester input and the test signal from the signal generator to test the control loop. In order to aid the testability of the circuit board, testing nodes (holes) are placed through-out the board. Finally, the board is fabricated by Advanced Circuit[6].

4.5 Efficiency Evaluation

The power electronics proposed here enables the energy harvester to extract more energy from its original resonant frequency and for additional harmonics. However, the power consumed in the electronics, namely the power path, the control logic and the gate switching must be accounted for in order to measure the true benefit. For our PCB implementation, the power losses from each circuit block is shown in Table 4.1 where it is also compared to an integrated circuit (0.18 μm CMOS) power consumption estimation.

The PCB implementation has a total power loss of 63.5 mW which is way beyond the harvested energy of 160 - 300 μW. However, examining closer at the power loss breakdown in Table 4.1, we can immediately notice the dominance of the power loss

[5]http://datasheets.maximintegrated.com/en/ds/DS1100.pdf
[6]http://www.4pcb.com/

Table 4.1: Power Losses Comparison for PCB and IC Implementation

Circuit Block	PCB	0.18μm CMOS
Control Logic	60 mW	<1μW (Digital)
Power Path	20 μW	38 μW
Switching + Gate Drive	3.5 mW	35 μW
Total	63.5 mW	73 μW

in our analog control logic. This power can be greatly reduced with a digital control implemented in integrated circuits such as the MSP430 which can consume less than 1 μW mentioned in Chapter 2. The power losses in the power path, mainly due to the DC resistance of the power FETs and their switching, can also be balanced better by designing custom drivers and FETs that match better. A general rule of thumb for power FET sizing optimization is to have the DC loss and switching loss at the same level. From Table 4.1, we can see that by making the switches smaller and hence decreasing the gate input capacitance the gate switching losses can be greatly decreased and lead to a total power loss improvement.

4.6 Chapter Summary

This chapter presented the core power electronics architecture that synthesizes complex impedance. The architecture presents several ideal characteristics for energy harvesting applications such as embedded voltage rectification and load impedance tunability. This circuit also solves one of the largest challenges for energy harvester resonance tuning - reactive component implementation. Inductive loads as large as 10s of Henries can be implemented using the proposed power factor correction (PFC) circuit.

We started out synthesizing resistive, capacitive and inductive loads with the proposed PFC circuit. Later in the chapter, we also demonstrated the circuit's capability of implementing more complex loads such as parllel-RL and LC tank circuits. These more complex loads will allow additional resonant frequencies to be created and enable the harvester to convert energy from multiple vibration frequencies simultaneously as illustrated in Chapter 6. A parallel-RL circuit will be experimentally demonstrated

to show it's capability to harvester energy from two frequencies.

In the next chapter, the harvester test bench will be introduced. This includes detailed description of the shaker table, harvester mounting process, automated data acquisition, and harvester characterization. A reliable and automated test bench is crucial in performing accurate and repeatable experiments for energy harvesting research. Experimental characterization of the harvester also fine tunes the theoretical model and provides a solid understanding of the energy harvester physics.

Chapter 5

Energy Harvester Test Bench

This chapter gives the detailed experimental setup and device characterization of the piezoelectric harvester. Most vibration energy harvester experiments today are preferred by mounting the harvester on a shaker table as shown in Figure 5-1. The shaker table physically simulates the actual vibration characteristics of the vibration source from which the harvester would be scavenging energy. Details on the making of our shaker table, issues concerning mounting the harvester onto the shaker table, and the setup of the automated data collection are addressed in the first section of this chapter. The next section in this chapter focuses on the electrical model and experimental characterization of the piezoelectric harvester. In the last section of this chapter, which describes the harvester characterization process, the piezoelectric physical model is compared with the SPICE electrical model and the experimental data. The purpose of this chapter is to serve as the foundation of the harvester system experimentation described in Chapter 6.

5.1 Test Bench Setup

The entire test bench used in our harvester experiments is shown in Figure 5-2. Other than regular test equipment such as signal generators, power supplies and oscilloscopes, the test bench consists of the shaker table, the piezoelectric harvester and the automated data collection system. This section will give the design details

Figure 5-1: Typical shaker table for energy harvesting applications. The one shown in the figure is the LDS V406 made by Bruel and Kjaer.

of these test bench components.

5.1.1 Shaker Table

As opposed to the commercial shaker table shown in Figure 5-1, the shaker table used in our experiments was built in-lab with an off-the-shelf speaker and a self-built amplifier as shown in the middle of Figure 5-2. A self-built shaker table is suitable for our energy harvesting application is mainly due to two reasons. First, the vibration force for energy harvesting applications are relatively small (<1g) and second, the harvester mass is relatively light such that the vibration force remains constant through-out the experimentation.

5.1.2 Piezoelectric Harvester Mounting

For the vibration kinetic energy to be optimally delivered to the piezoelectric harvester and hence transduced into electrical energy, the harvester has to be securely mounted

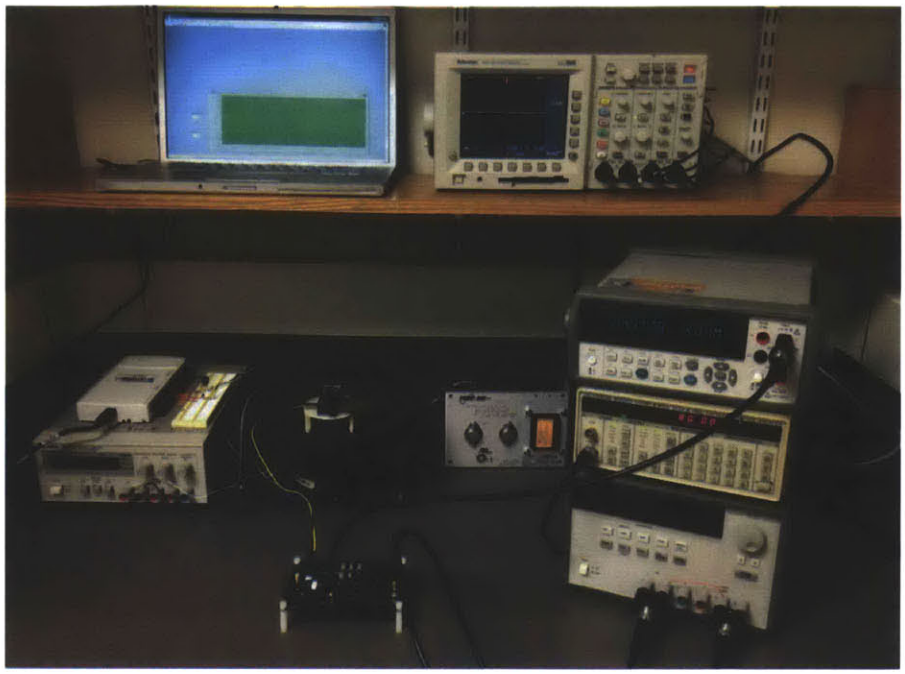

Figure 5-2: Experimental setup of the piezoelectric harvester, shaker table and the power electronics circuit board.

onto the shaker table. While this process may seem trivial, and may vary depending on the shaker table being used, it is a crucial step in harvester characterization and in all experiments that follow. One effective way to evaluate whether the harvester is correctly mounted is the observation of multi-resonant vibration characteristics. If more than one resonance is observed while performing a vibration frequency sweep, it is most likely that the harvester is not securely mounted on the shaker table since most commercial harvesters are high-Q, single-resonance resonators.

In the test-bench setup process of the experiments carried out in this thesis, a significant effort extended to address the harvester mounting issue. The initial harvester clamp design was a simple dual-bar structure which clamped the harvester at the electrical end of the cantilever as shown in Figure 5-3. This clamping led to a dual-harmonic resonance situation as shown in Figure 5-4. The additional resonance was due to the electrical connection port which accidentally became a cantilever itself and hence created additional resonances. These non-ideal resonances can be identified with a simple plastic cable tie by contacting one end of the plastic cable with

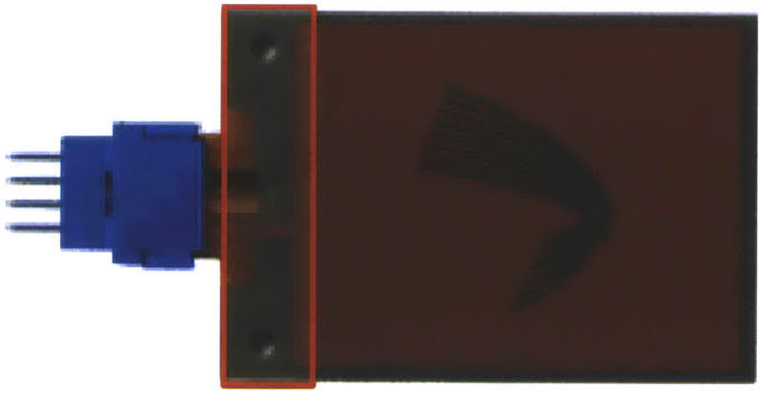

Figure 5-3: First generation harvester mount layout shown in the red box. The mount leaves out the blue electrical output port which creates additional non-ideal mechanical resonances.

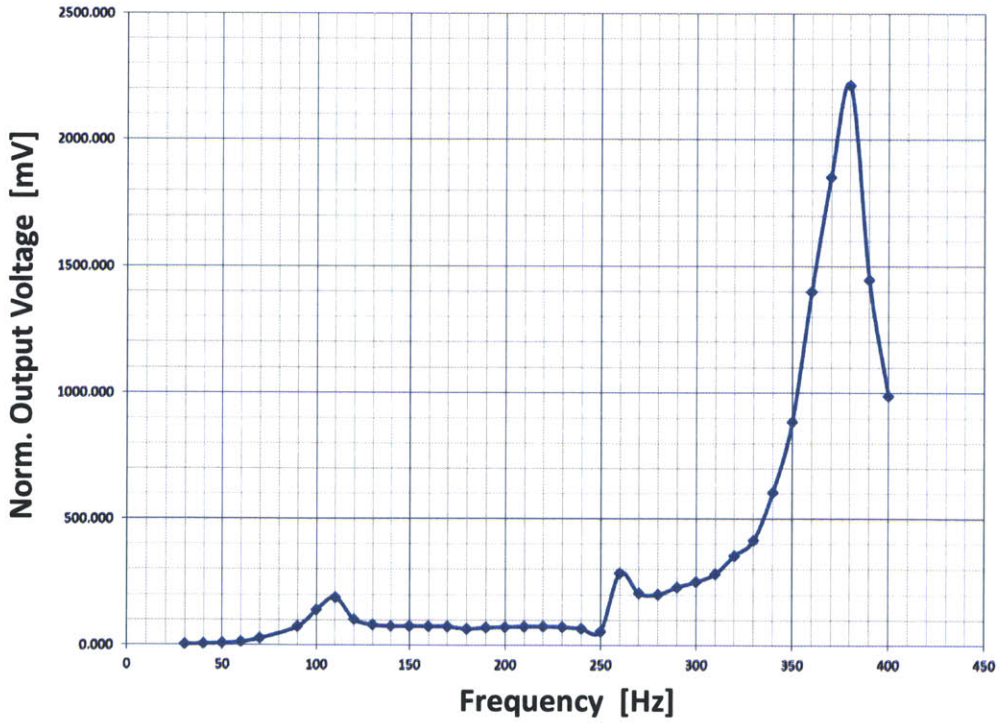

Figure 5-4: Non-ideal multi-resonant vibration characteristics due to improper harvester mounting. Additional resonant mainly due to electrical output port not securely mounted.

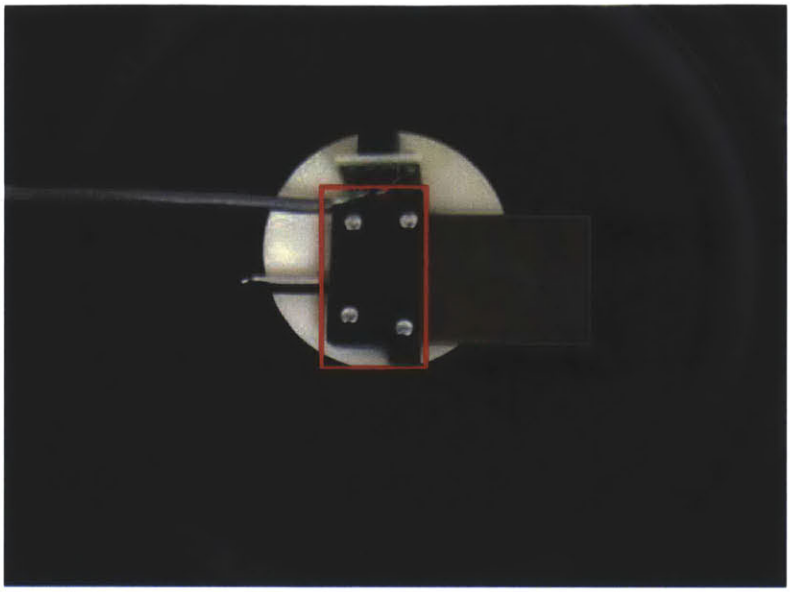

Figure 5-5: Final design of the harvester mount used to secure harvester onto shaker table. The mount is shown in the red box and covers the entire electrical output pin.

various parts of the shaker table and harvester.

With a few generations of iteration, the final design of the harvester mount is shown in Figure 5-5. It clamps down the entire electrical output port such that the piezoelectric cantilever is the only part of the harvester not secured on the shaker table. The securely mounted harvester is nicely characterized and compared with theoretical models as shown in Figure 5-10. Details on the piezoelectric model and the SPICE circuit simulations are given in the Section 5.2.

5.1.3 Automated Data Collection

An automated data collection and signal generation system was implemented with the NI USB-6211 multi-function DAQ shown in Figure 5-6. The box provides 16 analog inputs and two analog outputs with a sampling rate of 250 kS/s, making it ideal for our operational frequency range which is in the tens to hundreds of Hertz. With a USB connection to a computer, a script written in LabVIEW can drive the box to perform data acquisition and signal generation tasks. For our experiments, a LabVIEW program was written to automatically sweep the vibration frequencies over

Figure 5-6: NI USB-6211 multi-function DAQ made by National Instruments. The box provides automated signal generation and data acquisition for the harvester system experiments.

a given range. During the sweep, the program also records the output voltage from the piezoelectric harvester and the acceleration magnitude from the accelerometer mounted on the shaker table. It is important to record the acceleration data since shaker tables are not ideal and the acceleration varies when the load or vibration frequency changes.

5.2 Piezoelectric Harvester Characterization

In this section, the V25W piezoelectric harvester is characterized with the spring-mass-damper model and the equivalent circuit model which were given in detail in Section 3.1 and 3.2 respectively. These two models are also compared and confirmed with experimental results. Two separate experiments were carried out. The first was a open circuit voltage measurement experiment which swept the vibration frequency in order to characterize the unloaded harvester resonant frequency and quality factor. The second was a electrical loading experiment which loaded the harvester with various resistances to find the optimal matching resistance while shaking the harvester

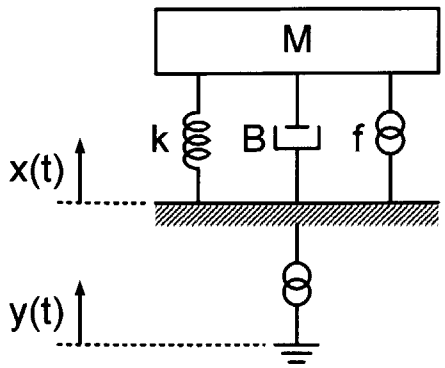

Figure 5-7: Spring-mass-damper model.

at its resonant frequency.

5.2.1 Open Circuit Voltage Characterization

The spring-mass-damper model as shown in Figure 5-7 characterizes the electromechanical dynamics of any vibration energy harvester. The parameters that need to be characterized through experimentation are namely the effective mass M, the spring constant k, the damping factor B and the conversion ratio G_P. The conversion ratio G_P is the relationship between the input force and output voltage where

$$f = G_P \cdot V \tag{5.1}$$

The first parameter that can be calculated is the effective mass M. By measuring the dimensions of the piezoelectric harvester, the effective mass can be obtained. Next, with the Equation 5.2 and assuming the system having a high quality factor, the spring constant k can be determined by measuring the resonant frequency ω_n of the piezoelectric harvester and the prior calculation of the effective mass M.

$$k = \omega_n^2 \cdot M \tag{5.2}$$

The damping factor B can also be obtained with the measurement of the quality factor Q of the harvester, since

Table 5.1: Piezoelectric Harvester Parameter

	Value	Units
Effective Mass M	2.2e-3	[kg]
Spring Constant k	18592	[N/m]
Damping Factor B	0.08	[N·s/m]
Conversion Ratio G	1.3e-3	[N/V]
Resonance Frequency ω_n	515.2	[rad/s]
Quality Factor	14.2	

$$B = \frac{M \cdot \omega_n}{Q} \tag{5.3}$$

Finally, the conversion ratio G_P can be obtained through the measurement of the acceleration and the output voltage of the harvester. These four parameters are fine tuned in a MATLAB program which can be found in Appendix A.2. The resulting parameters are shown in Table 3.1 and shown here again.

The equivalent circuit model of a piezoelectric harvester [50] is shown in Figure 5-8. Here the vibration kinetic force is represented as a voltage source, and the spring, mass and the damper of the piezoelectric are modeled as an equivalent capacitor C_K, an inductor L_M, and a resistor R_B. In addition, the piezoelectric coupling is modeled as an equivalent transformer with a transformer ratio G. These parameters can be obtained through translating the parameters found in Table 3.1 with Equations 3.30, 3.31 and 3.32 which are rewritten for ease of understanding.

$$L_M \equiv M \cdot \frac{J_v}{J_i} \tag{5.4}$$

$$R_B \equiv B \cdot \frac{J_v}{J_i} \tag{5.5}$$

$$C_K \equiv \frac{1}{k} \cdot \frac{J_i}{J_v} \tag{5.6}$$

In this model, the driving vibration is assumed to be perpendicular to the piezoelectric layers in such a manner that the piezoelectric material experiences a one-dimensional state of stress along the cantilever extended direction. The vibration force and velocity are expressed as a voltage source V_F and current i where

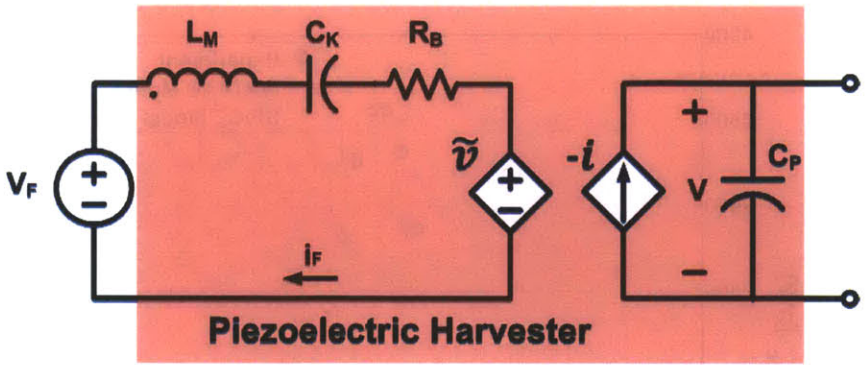

Figure 5-8: Piezoelectric harvester equivalent circuit model.

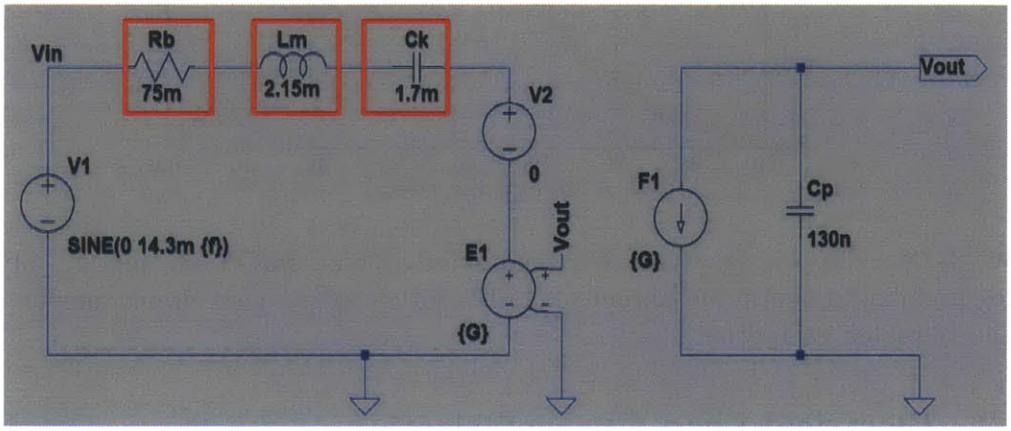

Figure 5-9: Piezoelectric harvester equivalent circuit model implemented in LTSpice.

$$V_F = J_v \cdot M \frac{d^2y}{dt^2} \tag{5.7}$$

The proof mass is assumed to be the point at the center of mass and the piezoelectric losses are assumed to be negligible. The piezoelectric parasitic capacitance is shown as C_p with a value of 130 nF, which can be obtained from the harvester data sheet. The model in Figure 5-8 is implemented in LTSpice and shown in Figure 5-9. With the two models implemented, MATLAB and LTSpice, a vibration frequency sweep experiment which measures the open circuit voltage of the piezoelectric harvester is carried out and the results are shown in Figure 5-10. The simulations and experiments were carried out under the same 0.7 g vibration acceleration across all frequencies.

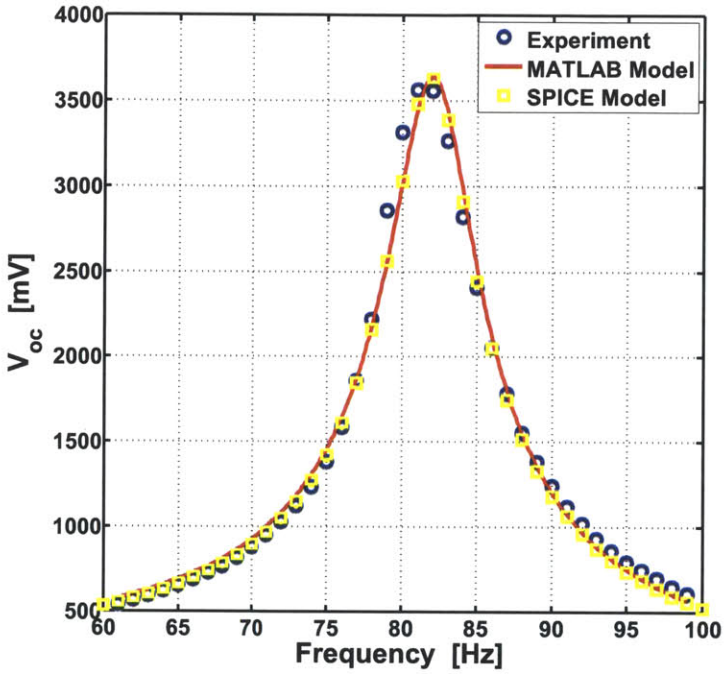

Figure 5-10: Piezoelectric harvester characterization: MATLAB model, SPICE model, and experimental measurements of the piezoelectric open circuit output voltage nicely match each other.

5.2.2 Electrical Load Characterization

The second experiment carried out is to find the optimal resistive load for the harvester. From a circuit point of view, this value is often known as the matched load. However, this is not accurate especially for piezoelectric harvesters which have large parasitic capacitances. A matched load would have to also include the matched reactance that cancels out the parasitic capacitance. Since we are only trying to confirm our models with our experiment, finding the matched resistive load is a good experiment for this purposes.

As shown in Figure 5-11, the experimental data and the MATLAB code which implements the spring-mass-damper model match nicely with one another. The MATLAB code can be found in Appendix A. At resistances smaller than 10 kΩ, the output open circuit voltage increases linearly with the resistance and therefore, the output power increases linearly. When the resistance reaches around 40 kΩ, the rate of voltage increase rapidly slows down and the voltage quickly becomes a constant value.

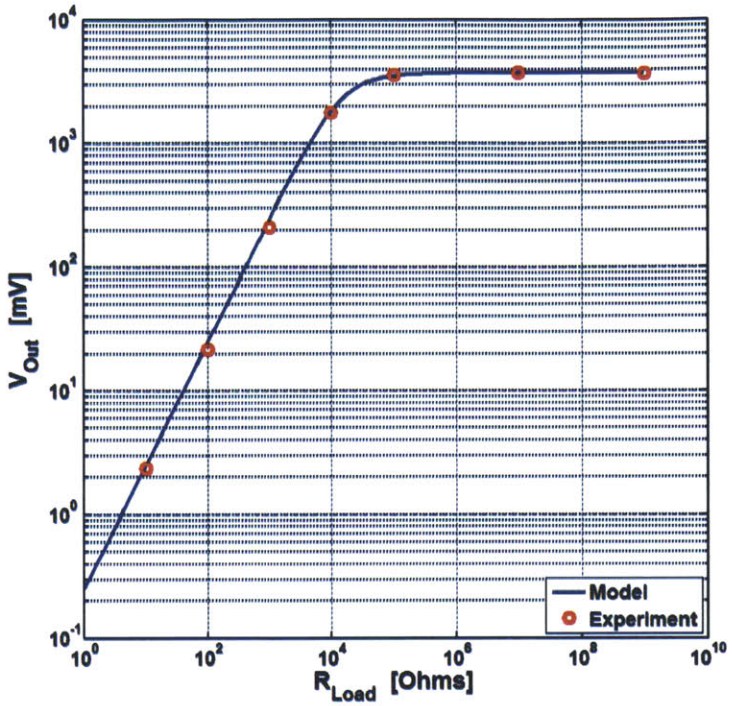

Figure 5-11: Output voltage versus resistive load plot. As can seen from the plot, the maximum output power is achieved at the turning point of the curve which is around 40kΩ.

The maximum output power is hence the turning point of the curve shown in Figure 5-11 which is 46.5 kΩ. At this load resistance level, the harvester delivers the maximum amount of power to the electrical load under the condition that no internal reactance is canceled out. The important point here is that the simulation nicely matches the experiment.

5.3 Chapter Summary

In this chapter, the setup of the experimental test bench and the characterization of the harvester were described in detail. In order to perform accurate experiments, it is extremely important to have a secure and characterized shaker table especially if the shaker table is self-built. For a commercial shaker table, it is still important to measure the acceleration of the shaker table such that the mechanical power driving the harvester is measured and remains constant throughout the experimentation. A

secure mounting of the harvester on the shaker table is also of great importance. Insecure mounting not only results in decreased output power, but also increases the possibility of creating additional non-ideal mechanical resonances. This chapter provided means of detection and solutions for non-ideal non-ideal harvester mounting.

Another important part of our test bench is performing quick vibration frequency analyses with the implementation of an automated DAQ system. The system performs automated vibration frequency sweeps while automatically recording the output electrical voltages. The USB control box communicates between a computer which contains the LabVIEW program and the energy harvester system. This system greatly decreased the time of performing frequency analyses of the energy harvesting system.

In the final part of this chapter, the V25W piezoelectric harvester was characterized using the spring-mass-damper model, the equivalent model and experimental data. Harvester parameters such as the spring constant, effective mass, damping ratio and electromechanical conversion ratio are obtained. Accurate matching between the models and the experiment shown that the models nicely characterize the piezoelectric harvester and provide a solid foundation for understanding and experimentation of more complex harvester systems. Experimental results of the power electronics working with the harvester are given in the following chapter.

Chapter 6

Harvesting Simulation and Experiments

This chapter is divided into two parts. The first part shows the experimental results of a parallel RL electrical load synthesized with the power electronics architecture proposed in Chapter 4. Two experiments were demonstrated. The first is maximum power transfer and second is dual-resonant energy harvesting. The good matching between the experimental results, the SPICE simulations and the spring-mass-damper model implemented in MATLAB serves as a foundation for the implementation of more complex loads with the same power electronics architecture.

The second section of this chapter utilizes the power electronics to analyze the more complex LC tank circuit which enables maximum power transfer to be achieved at two desired harmonics. From the closely matched experiment and simulation from the first part, a LC tank circuit implemented in the proposed power electronics architecture should also display similar experimental results to its simulation. While experiments were not carried out for the LC tank circuit due to the scope and time constraints of this thesis, it is a promising area for future research.

6.1 Harvesting Experiments

This section shows the experimental test results of the impedance tuning power electronics proposed in the previous chapter. Two experiments will be demonstrated in this chapter. The first is maximum power transfer and second is dual-resonant energy harvesting. For the piezoelectric harvester to deliver the maximum amount of power to the electrical load, and in this case a DC source, the parasitic capacitance C_p and the internal damping resistance R_B must be matched with the electrical load impedance Z_L. In this experiment, we use the power electronics to synthesize parallel RL load that matches the piezoelectric harvester internal impedances.

Built on the foundation of the first experiment, the second experiment demonstrates the power electronics capability of creating a second resonant frequency and effectively harvesting energy from two frequencies simultaneously. The experimental results closely match the expected simulation results when non-ideal losses such as switching and DC losses are taken into account. Discussions on the experimental results compared to the simulation are given for both experiments. This section shows that the impedance tuning theory in Chapter 3 and the circuit architecture in Chapter 4 can be nicely proved and demonstrated in experimentation.

6.1.1 Maximum Power Transfer

As mentioned in Chapter 2, a piezoelectric harvester contains a large parallel parasitic capacitance C_p that limits the amount of output power that can be delivered to the electrical load. Therefore, a piezoelectric harvester cannot provide its maximum output power potential unless the parasitic capacitor is canceled out by a parallel inductor.

In this section, the power electronics developed in Chapter 4 is used to synthesize a parallel RL load that cancels out the parasitic capacitance and delivers the maximum amount of power to the electrical load. The target parallel RL circuit is shown in Figure 6-1 with an 29 H inductor and 44 kΩ resistor. While the inductor cancels the capacitor at the resonant frequency of 82 Hz, it should be noted that they do

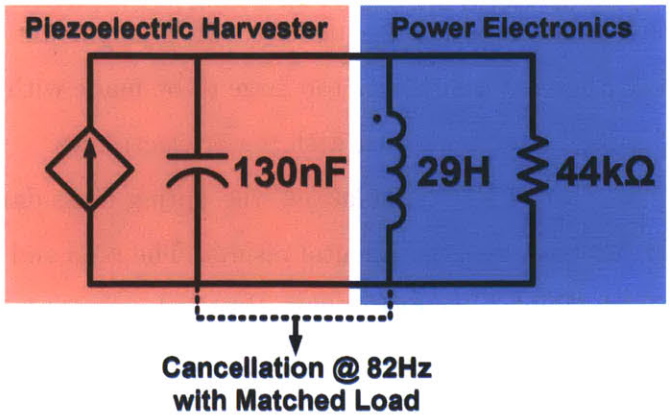

Figure 6-1: Schematic of piezoelectric harvester with matched impedance at resonance. The load inductor cancels the parasitic capacitor at resonance and enables the maximum amount of power being delivered to the load resistance.

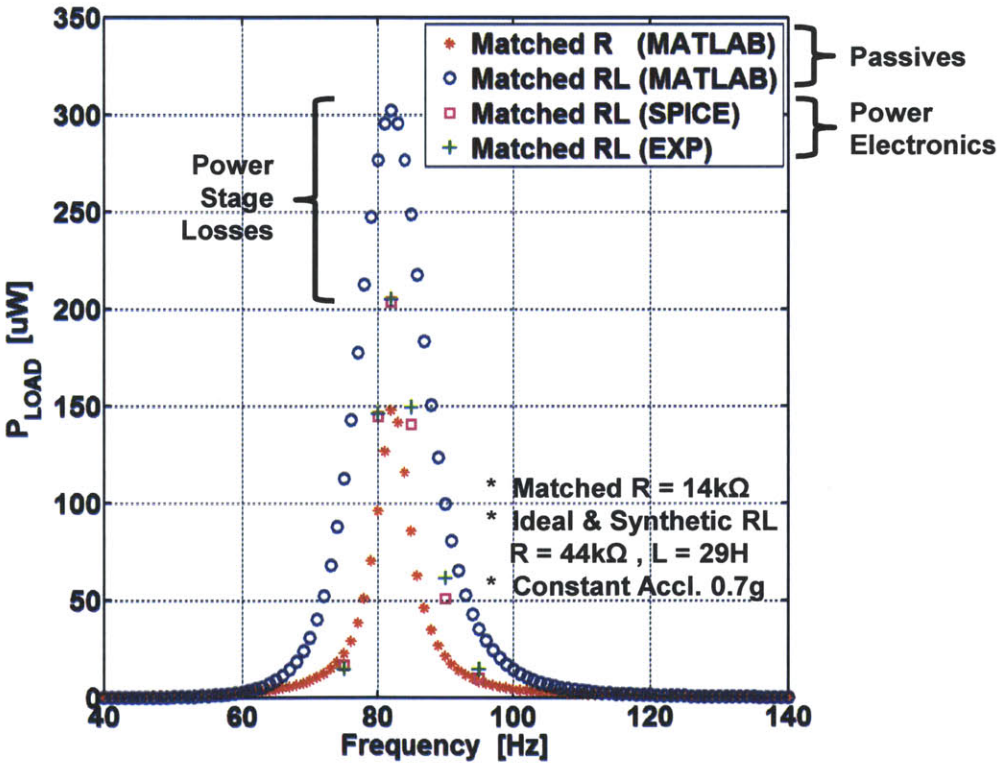

Figure 6-2: Simulated and experimental results of a RL-loaded piezoelectric harvester that enables maximum power transfer to the electrical load. The red star curve indicates the harvester loaded with a real 14 kΩ resistor, and the blue circle curve shows the harvester loaded with a real 44 kΩ resistor and 29 H inductor. The purple square curve is the harvester loaded with power electronics synthesized RL load. The green crosses are the experimental results. Constant acceleration of 0.7 g was used in the simulations and experiment.

not cancel out each other at other frequencies. It is important to note that the inductance of the synthesized inductor is too large to be made with coils and provide good efficiency. It must be implemented with power electronics.

Figure 6-2 shows the SPICE simulation, the spring-mass-damper model programmed in MATLAB and the experimental results. The blue and red curves shown in Figure 6-2 are both simulations of the piezoelectric harvester loaded with passive components where the red curve is loaded with a resistor (14 kΩ) and the blue curve is loaded with a resistor (44 kΩ) and inductor (29 H) in parallel. The 14 kΩ resistor used in the red curve draws the greatest power from the piezoelectric harvester without canceling out C_p. The blue curve on the other hand, implements Figure 4-13 in which the inductor cancels out C_p at the harvester resonant frequency and the resistor is a matched load chosen to maximize the power delivered to the resistor. From Figure 6-2, it is shown that the output power doubles with the cancellation of C_p.

The purple square curve represents the LTspice simulation results of the power electronics synthesized parallel-RL. While the blue curve and the purple curve implement the same load, the purple curve has additional power losses due to the gate switching and DC resistive (85 Ω) losses of the smoothing inductor. All of the simulations in Figure 6-2 are done under the condition of constant acceleration of 0.7 g. Finally, the green crosses in Figure 6-2 represent the experimental results. It can be noted that the SPICE-simulated (purple) and experimental (green) results match well which indicates the high accuracy of the simulation. The ideal (blue) and power-electronic (purple) power differ due to parasitic gate capacitance in the bridge FETs.

6.1.2 Dual-resonant Energy Harvesting

The second experiment carried out is the demonstration of a dual-resonant energy harvesting system. Using the same power electronics circuit in the previous section, this experiment synthesizes the parallel RL circuit shown in Figure 6-3. The syn-

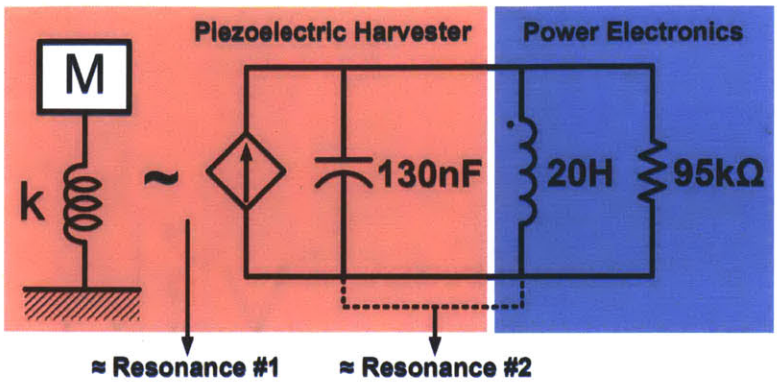

Figure 6-3: Schematic of piezoelectric harvester with a parallel RL load. The load inductor couples with the parasitic capacitor and creates an additional resonance in addition to the original mechanical resonant frequency.

Table 6.1: Dual-resonant Harvester Output Power

Vibration Frequency [Hz]	Output Power [μW]
82	158
98	61
82 + 98	219

thesized inductor is now 20 H. Instead of cancelling out the parasitic capacitor C_p, it forms a LC tank with C_p and introduces a second resonant pole pair to the system. It should be noted that the spring-mass pole pair and the LC pole pair differ slightly with the actual location of the isolated resonant frequencies because the mechanical and electrical parts of the harvester interact with each other. Details of this phenomenon were given in Section 3.3.2.

Figure 6-4 shows the simulated and experimental results of an arrangement in which the harvester capacitance and power-electronic inductor create a second resonance at 98 Hz to improve harvesting at that frequency. Here the blue and red curves are MATLAB simulations using real passive resistors and inductors while the purple curve is the LTspice simulation of the power electronics. Here the red curve indicates the output power of a harvester loaded with the optimal 14 kΩ resistance, and the blue and purple curve simulate the parallel-RL circuit shown in Figure 6-3. The green curve indicates the experimental results. It can be noted that the SPICE-simulated (purple) and experimental (green) results match well which again indicates the high

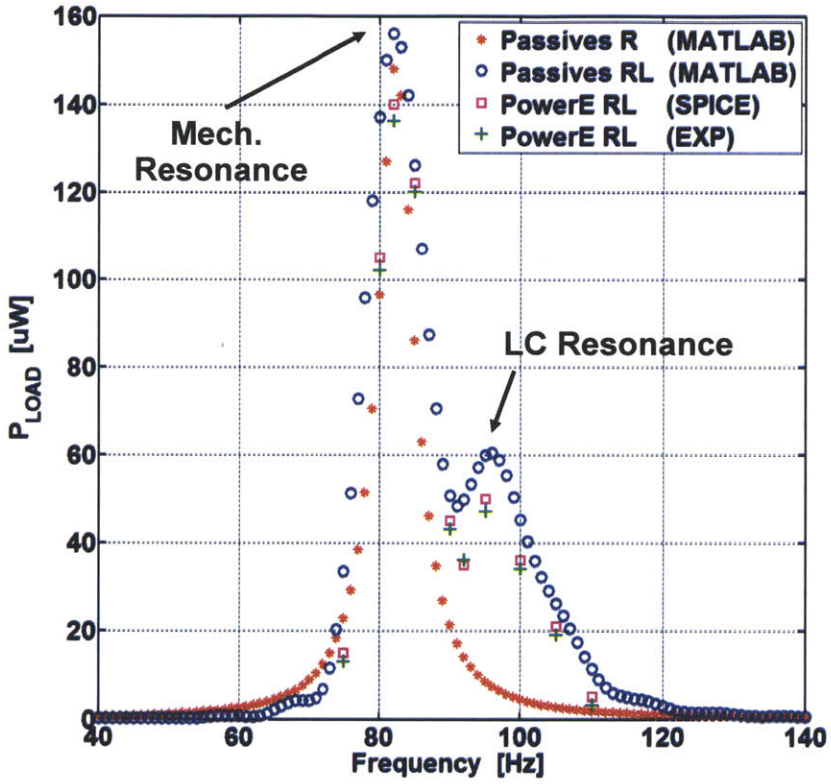

Figure 6-4: Simulated and experimental results of a RL-loaded piezoelectric harvester that creates an additional resonant frequency. The red curve indicates the harvester loaded with a real 14 kΩ resistor, and the blue curve shows the harvester loaded with a real 95 kΩ resistor and 20 H inductor. The purple square curve is the harvester loaded with power electronics synthesized RL load. The green cross is the experimental results. Constant acceleration of 0.7 g was used in the simulations and experiment.

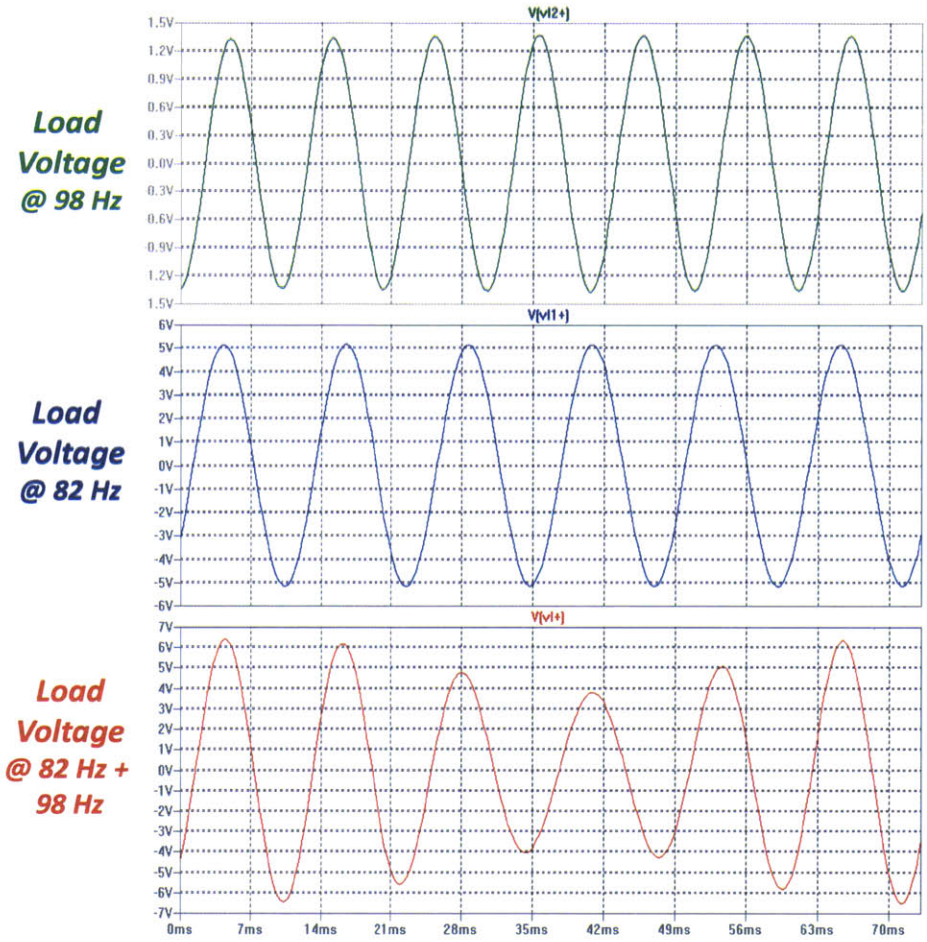

Figure 6-5: Simulated transient voltage waveforms of the dual resonant harvester. It can be clearly seen in the figure that the harvesting system has two resonant frequencies at 82 Hz and 98 Hz. In addition, the output voltages and hence power add up when both vibration frequencies stimulate at the same time. Constant acceleration of 0.7 g is applied throughout the simulations.

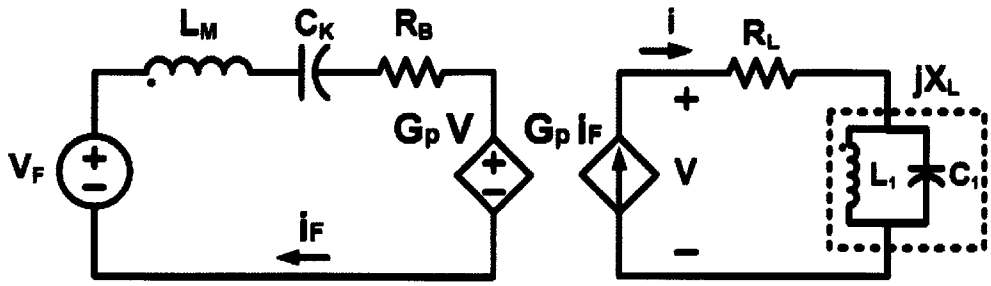

Figure 6-6: Equivalent circuit of a dual-resonance vibration energy harvester.

accuracy of the simulation.

The resistor and inductor sizes were chosen to create a second resonance at 98 Hz and deliver the equal amount of output power at the original 82 Hz mechanical resonance. Nonetheless, in using the load inductor to create a second resonance, its function of compensating the piezoelectric capacitance is lost, so overall energy harvesting suffers. This smaller output power at the second resonance is due to the fact that the inductor only cancels the parasitic capacitance at the original resonant frequency of 82 Hz. This non-ideal situation will be addressed in the next section with a series resistance and parallel LC simulation.

When the dual-resonant harvester is excited with its two resonant frequencies simultaneously, the output voltage transient wave forms are shown in Figure 6-5. It can be clearly seen from Figure 6-5 that the harvester is a dual-resonant system. The two resonant frequencies are 82 Hz and 98 Hz respectively. The total output power of the simulations are shown in Table 6.1 where the dual frequency energy harvesting capability of the system is demonstrated.

6.2 Harvesting Simulations

In the previous section, we discovered that while the parallel-RL structure enables maximum power transfer and provides the possibility for improved dual-frequency energy harvesting, these two energy harvesting benefits cannot be achieved at the same time as shown in the output power frequency response in Figure 6-4. In this

Table 6.2: Dual-resonant Harvester Output Power

Vibration Frequency [Hz]	Output Power [μW]
65	298
134	301
65 + 134	599

section, we will use the proposed power electronics to implement the multi-resonant harvesting system shown in Chapter 3. This configuration shown in Figure 3-9 and reproduced in Figure 6-6 for the dual-resonant harvester case, enables the harvester to achieve maximum energy transfer at two resonant frequencies.

Using the power electronics structure shown in Figure 4-15 to implement the electrical load shown in Figure 6-6, we obtain the output power frequency response shown in Figure 6-7. The figure shows that the MATLAB model and SPICE simulations match closely. When exciting the energy harvester simultaneously with its two resonant frequencies (65 Hz and 134 Hz) each with the same acceleration of 0.7 g, we can see the additive relationship between the acceleration and the output voltage from Figure 6-8. In addition, from the simulations shown in Figure 6-9, we can compare exciting the system with its single frequencies to dual-frequency excitation, and can see that the output voltages of the individual waveforms add up to the combined waveform. The output powers hence experimentally add up as shown in Table 6.2.

The same power electronics can also synthesize a triple-resonant system as presented in Figure 6-10. The SPICE simulations match closely with the MATLAB simulations as shown in Figure 6-11. The simulations assume a constant acceleration of 0.7 g while generating the output power frequency response. Figure 6-12 shows the triple-resonant harvester being excited by three resonant frequencies (61 Hz, 125 Hz and 206 Hz) at the same time and with the same acceleration of 0.7 g. From the figure we can see the linear relationship between the acceleration and the output voltage. In addition, from the simulations shown in Figure 6-13, we can see that the output voltages of the individual waveforms add up to the combined waveform. The output powers hence experimentally add up together as shown in Table 6.3.

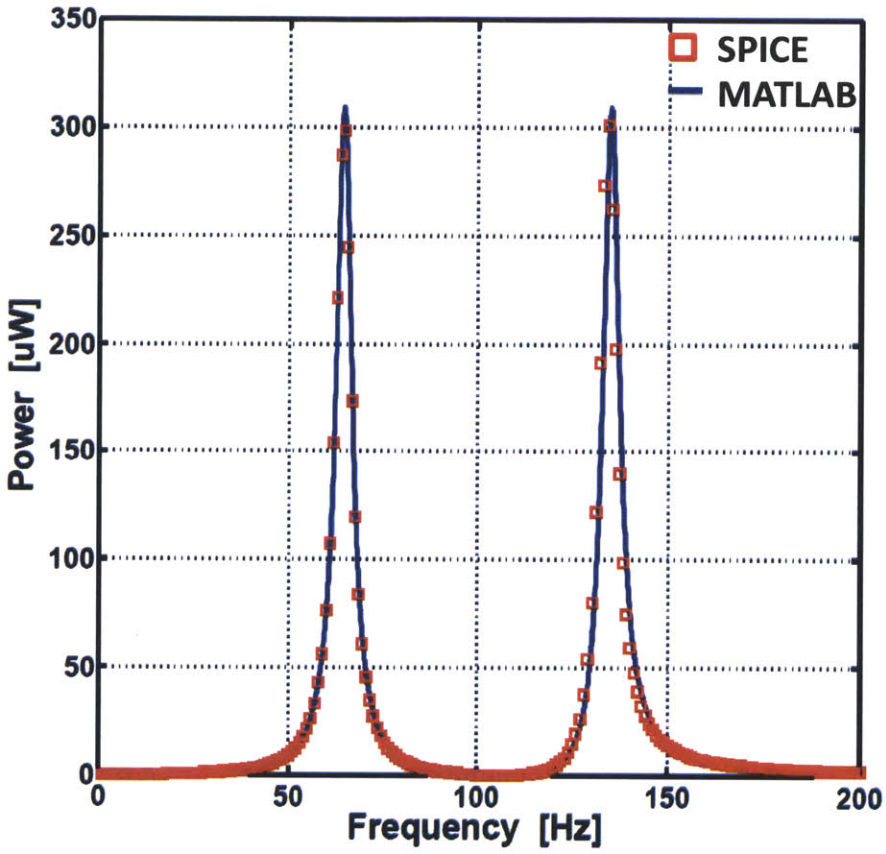

Figure 6-7: SPICE simulation and MATLAB model of the dual-resonant harvester match. Constant acceleration of 0.7 g is applied throughout the simulations.

Table 6.3: Dual-resonant Harvester Output Power

Vibration Frequency [Hz]	Output Power [μW]
61	298
125	274
206	287
61 + 125 + 206	859

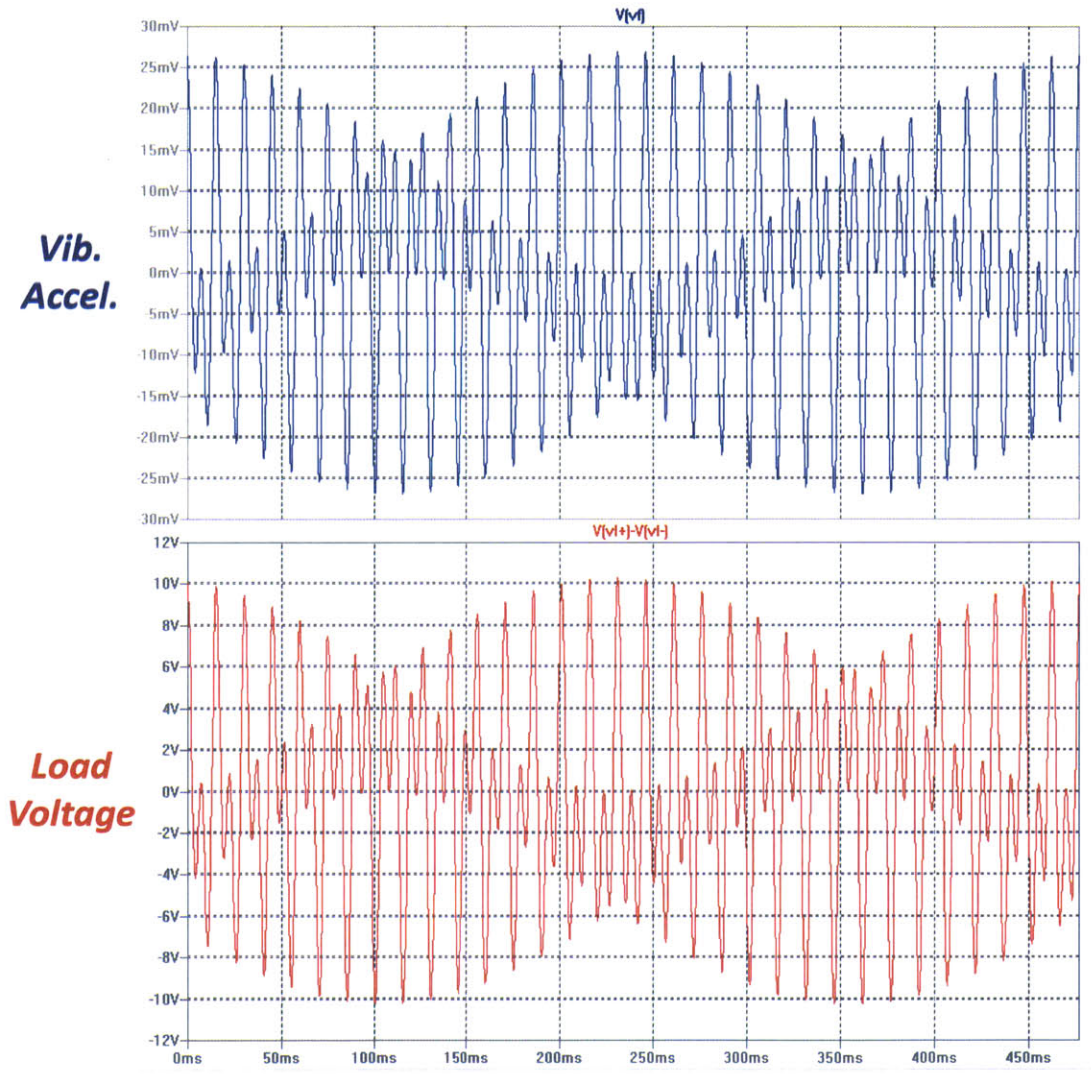

Figure 6-8: Load voltage and vibration acceleration waveforms of the synthesized parallel LC tank circuit. The figures show the system being excited by vibration frequencies of 134 Hz, 65 Hz simultaneously. Constant acceleration of 0.7 g is applied throughout the simulations.

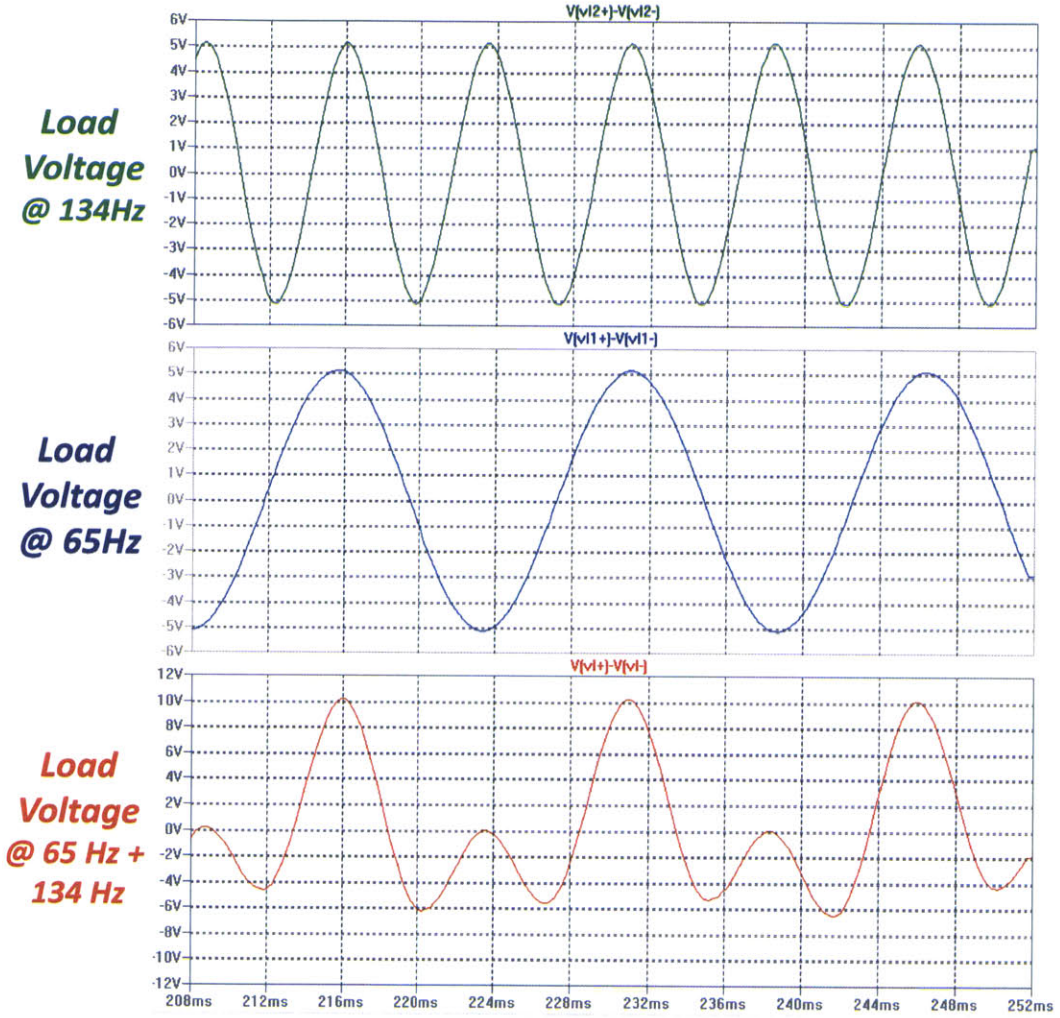

Figure 6-9: Load voltage waveforms of the synthesized parallel LC tank circuit. The figures show the system being excited by vibration frequencies of 134 Hz, 65 Hz and with both frequencies together. Output voltages of the individual waveforms add up to the combined waveform. Constant acceleration of 0.7 g is applied throughout the simulations.

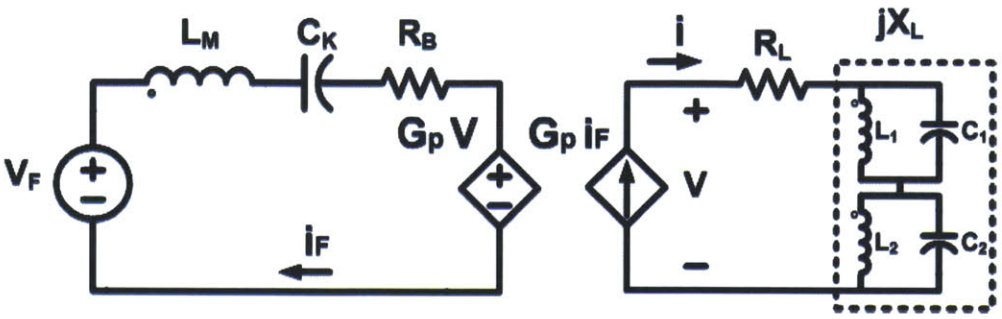

Figure 6-10: Equivalent circuit of a triple-resonance vibration energy harvester.

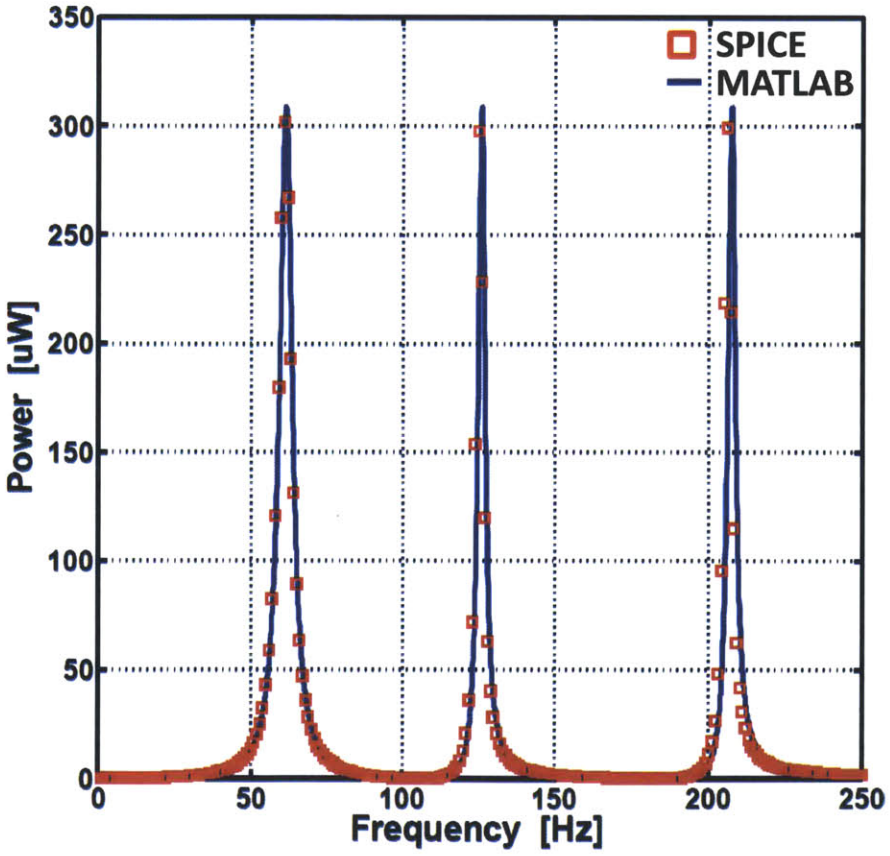

Figure 6-11: SPICE simulation and MATLAB model of the triple-resonant harvester match. Both simulations assume constant driving acceleration of 0.7 g.

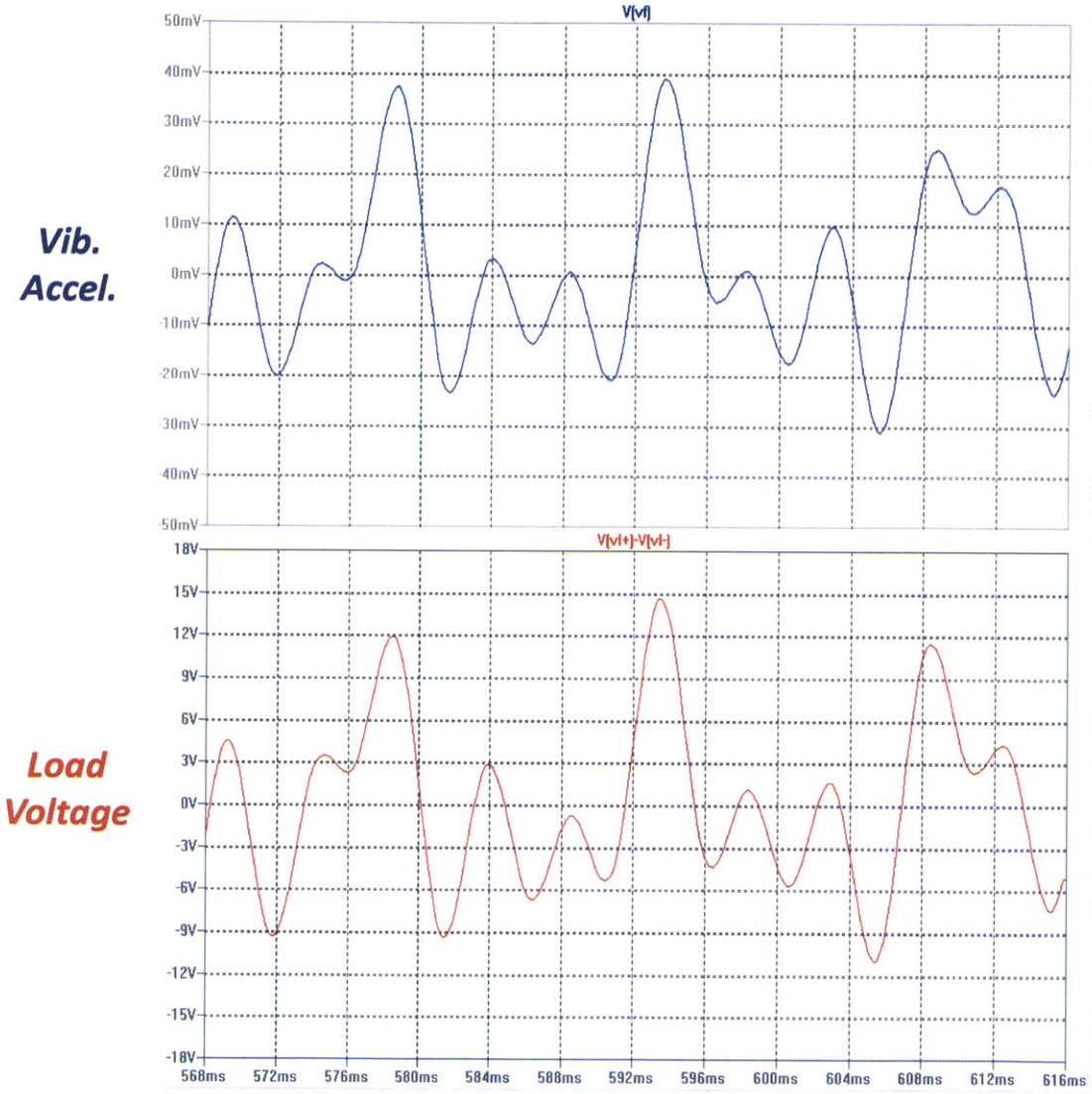

Figure 6-12: Load voltage and vibration acceleration waveforms of the synthesized parallel LC tank circuit. The figures show the system being excited by vibration frequencies of 134 Hz, 65 Hz simultaneously. Constant acceleration of 0.7 g is applied throughout the simulations.

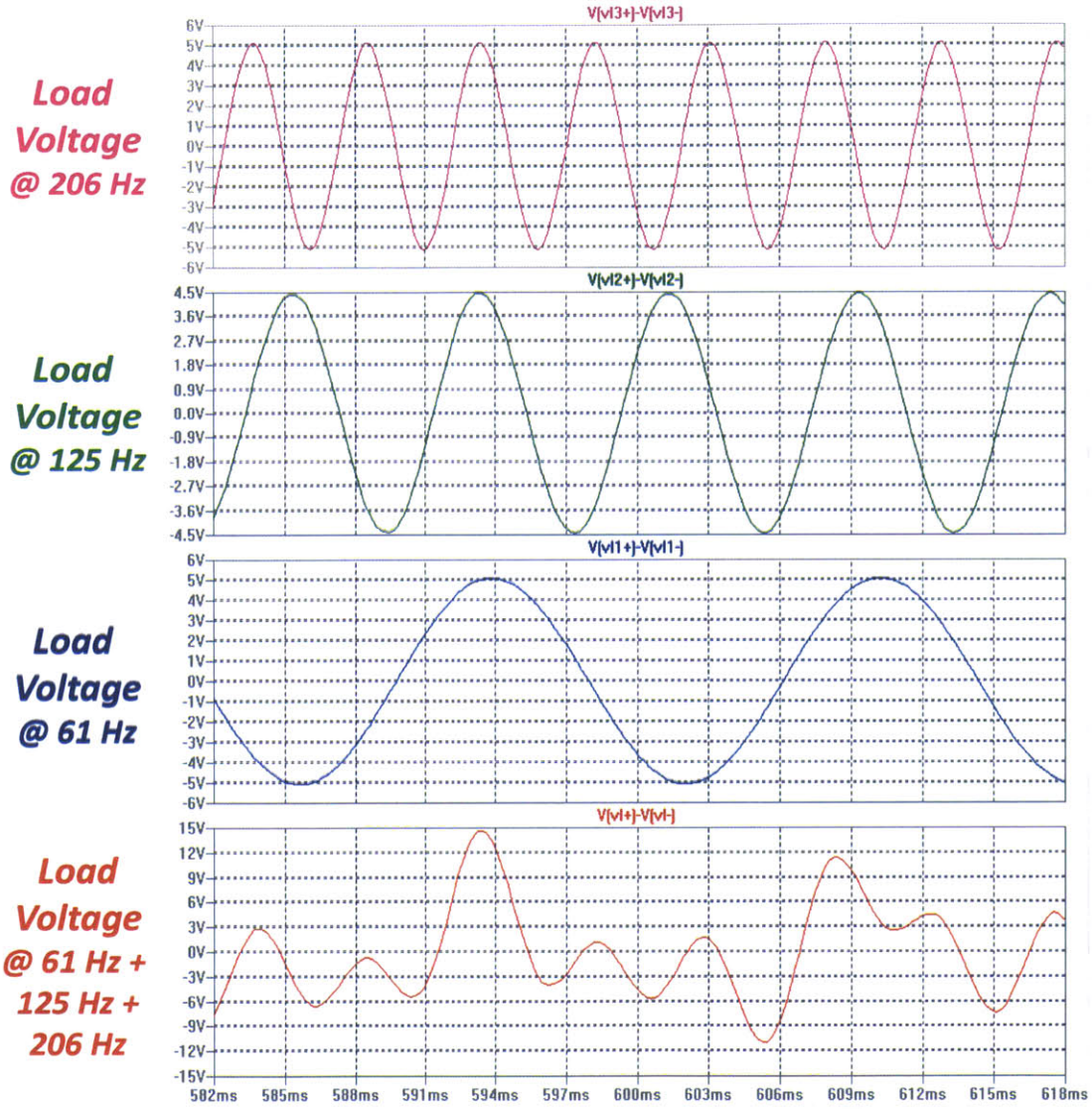

Figure 6-13: Load voltage waveforms of the synthesized parallel LC tank circuit. The figures show the system being excited by vibration frequencies of 61 Hz, 125 Hz and 206 Hz and with all frequencies together. Constant acceleration of 0.7 g is applied throughout the simulations. Output voltages of the individual waveforms add up to the combined waveform.

6.3 Chapter Summary

This chapter showed the experimental results of a parallel RL electrical load synthesized with our proposed power electronics and simulation results of the more complex LC tank electrical load. The first section utilized two experiments to demonstrate the power electronics system proposed in Chapter 4. The first experiment demonstrated the power electronics' capability to cancel the piezoelectric parasitic capacitance and deliver maximum power to the electrical load. The second experiment on the other hand, created a dual-resonant energy harvesting system. It should be noted that both experiments were performed with the exact same power electronics circuit and PCB hardware. This proves that the PCB is tunable and provides great design flexibility. In addition, the close matching between the simulation and the experiment justifies the accuracy of our simulations and experiments.

In the second section, simulations of the more complex LC tank load is carried out. The LC tank load addresses the non-ideality of using a RL load to create additional resonances. Namely, not allowing maximum power transfer to be achieved at all resonant frequencies. Simulation results show that a constant matched resistance in series with a LC tank circuit permits maximum power transfer and multi-resonant harvesting to be achieved simultaneously. This complex load can also be implemented with the same board with adjustments to the control logic which determines the I-V characteristics of the electrical load. A digital control logic would be an ideal next generation improvement, since it decreases the power loss and increases the ease of impedance tuning.

Chapter 7

Summary, Conclusion, and Future Work

The final chapter of this thesis summarizes the discoveries and innovations of this thesis and also paves the way for future research improvements that can be done. At the beginning, the summaries of each chapter will be given followed by the conclusion of the thesis. In the conclusion section, we will present the complete design methodology of building a multi-harmonic energy harvesting system. Finally, the thesis will conclude with future improvements in the field of vibration energy harvesting and some final words on the incredible journey of this thesis.

7.1 Summary and Conclusions

Chapter 1 begins with an introduction to the general idea of energy harvesting and slowly evolves toward harvesting energy from ambient vibration sources. The major drive behind the research interest in vibration energy harvesting stems from the rapid development of low power microelectronics and the need to power devices where traditional power lines have limited access. However, major technical challenges such as how to increase the extracted power from the ambient vibration source and how to deal with non-ideal vibration characteristics such as frequency shifts have limited its application range in everyday life. This thesis addresses these two challenges by

electrically tuning the harvester with power electronics. Both a theoretical model and an experimental demonstration is developed in the process.

Chapter 2 gives the background and previous research done in the area of vibration energy harvesting. Within vibration energy harvesting, there are three major energy conversion methods: electromagnetic, electrostatic and piezoelectric. Details of the conversion physics are given in Section 2.3. Taking the piezoelectric harvester for an example, this thesis proposed a simplified model which describes the electromechanical physics as

$$f = G_p \cdot v \tag{7.1}$$

$$G_p \cdot u = i \tag{7.2}$$

This simplified model is derived from the basic coupling coefficient and physical parameters of the piezoelectric and can be found in Section 2.3. It should be noted that Equations 7.1 and 7.2 only describes the electromechanical energy conversion part of the harvester. In Section 2.4, an overview of the challenges and previous works by other researchers on harvesting energy from non-ideal sources is given. This serves as a starting foundation of previous knowledge for this thesis. Finally, since this thesis will take an electrical circuit approach to address the challenges in energy harvesting, previous works on harvester interfacing circuits are given in Section 2.5.

Chapter 3 provides the theoretical backbone of impedance matching for vibration energy harvesting. The spring-mass-damper model and the equivalent circuit model developed in previous works is first introduced in Section 3.1 and 3.2. Building upon these two models, Section 3.3 further evolves toward finding the optimal impedance for more general vibration conditions. These include single resonant frequency tuning, dual resonant frequency, triple resonant frequency and finally N-resonant frequency energy harvesting. An interesting phenomenon to be noted is that while the optimal reactance changes for different situations, the optimal resistance remains constant and only depends on the mechanical damping and the electromechanical conversion ratio.

An important discovery in this chapter is that the required reactive components, namely the inductor, are too large to be implemented with real devices with today's technology and have to be synthesized with power factor correction (PFC) power electronics. Details of the architecture, design, and simulation results of the power electronics are shown in the following chapter.

Chapter 4 presents the core power electronics architecture that synthesizes complex impedance. In Section 4.1, the chapter first gives the background on impedance synthesizing circuits including power factor correction circuits and bias-flip inductors. Due to the need to synthesize complex impedances, a circuit architecture based on the power factor correction circuit is presented in Section 4.2. Detailed syntheses of a resistive, inductive and capacitive impedances were also shown in Section 4.2. The architecture presents several ideal characteristics for energy harvesting applications such as embedded voltage rectification and load impedance tunability. This circuit also solves one of the largest challenges for energy harvester resonance tuning: reactive component implementation. Inductive loads as large as 10s of Henries can be implemented using the proposed power electronics structure. This chapter also shown the circuit's capability of implementing more complex loads such as parllel-RL and LC tank circuits in Section 4.2. These more complex loads allow additional resonant frequencies to be created and enable the harvester to convert energy from multiple vibration frequencies simultaneously. A parallel-RL circuit will be experimentally demonstrated to show it's capability to harvester energy from two frequencies. A printed circuit board demonstration of this circuit was built and the details of the design can be found in Section 4.4 with efficiency evaluations shown in Section 4.5.

In Chapter 5, the setup of the experimental test bench and the characterization of the harvester were described in great detail. In order to perform accurate experiments, it is extremely important to have a secure and characterized shaker table especially if the harvester is self-built. For a commercial shaker table, it is still important to measure the acceleration of the shaker table such that the mechanical power driving the harvester is measured and remains constant throughout the experimentation. A secure mounting of the harvester on the shaker table is also of great importance.

Insecure mounting not only results in decreased output power, but also increases the possibility of creating additional non-ideal mechanical resonances. Another important part of our test bench is performing quick vibration frequency analyses with the implementation of an automated DAQ system. The system performs automated vibration frequency sweeps while automatically recording the output electrical voltages. The USB control box communicates between a computer which contains the LabVIEW program and the energy harvester system. This system greatly decreased the time of performing frequency analyses of the energy harvesting system. Design details of the test bench setup are given in Section 5.1. In Section 5.2, the V25W piezoelectric harvester was characterized using the spring-mass-damper model, the equivalent model and experimental data. Harvester parameters such as the spring constant, effective mass, damping ratio and electromechanical conversion ratio are obtained. Accurate matching between the models and the experiment shown that the models nicely characterize the piezoelectric harvester and provide a solid foundation for understanding and experimentation of more complex harvester systems. Experimental results of the power electronics working with the harvester are given in the following chapter.

Finally, in Chapter 6, we showed the experimental results of a parallel RL electrical load synthesized with our proposed power electronics and simulation results of the more complex LC tank electrical load. The first section utilized two experiments to demonstrate the power electronics system proposed in Chapter 4. The first experiment demonstrated the power electronics' capability to cancel the piezoelectric parasitic capacitance and deliver maximum power to the electrical load. The second experiment on the other hand, created a dual-resonant energy harvesting system. It should be noted that both experiments were performed with the exact same power electronics circuit and PCB hardware. This proves that the PCB is tunable and provides great design flexibility. In addition, the close matching between the simulation and the experiment justifies the accuracy of our simulations and experiments. In the second section, simulations of the more complex LC tank load is carried out. The LC tank load addresses the non-ideality of using a RL load to create additional

resonances. Namely, not allowing maximum power transfer to be achieved at all resonant frequencies. Simulation results show that a constant matched resistance in series with a LC tank circuit permits maximum power transfer and multi-resonant harvesting to be achieved simultaneously. This complex load can also be implemented with the same board with adjustments to the control logic which determines the I-V characteristics of the electrical load. A digital control logic would be an ideal next generation improvement, since it decreases the power loss and increases the ease of impedance tuning.

7.2 Design Review

In this thesis, we presented a energy harvesting system design methodology which includes an impedance matching theory and a power electronics architecture whose goal is to enhance the harvester's energy harvesting capability. The impedance matching theory expands the well known single resonance spring-mass-damper model to a multi-resonant impedance matching model. By connecting LC tank circuits to the harvester output, additional resonant frequencies are created and hence enabling the energy harvesting system to harvest energy from multi-harmonic vibration sources. However, the required inductor in the LC tanks circuits are often too large (>10 H) to be implemented with discrete components. Our proposed power electronics circuit addresses this issue by synthesizing these complex impedances with a power factor correction (PFC) circuit. This circuit mainly consists of a H-bridge, which contains four FETs, and a control loop that orders the FETs to turn on and off at the right time such that the load voltage and current display the characteristics of the desired complex load impedance. To get a better understanding of the design process, here we present a design example of a dual-resonant energy harvester.

Assuming the harvester designer encounters a vibration source that displays two simultaneous resonant frequencies ω_1 and ω_2. In addition, we also assume that the acceleration of the two resonant frequencies are relatively the same. This additional assumption is important since a regular single resonant harvester would be sufficient

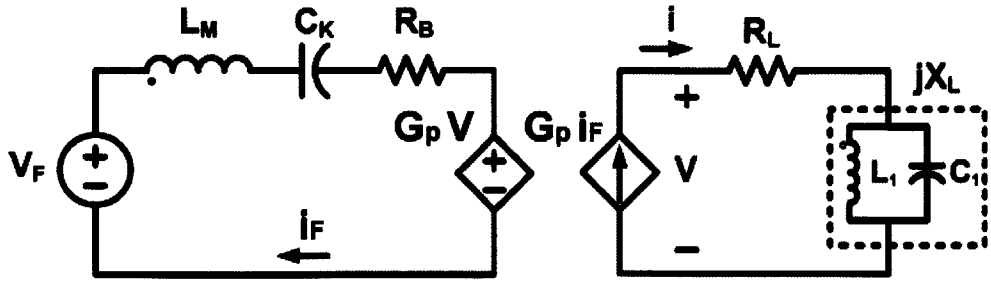

Figure 7-1: Equivalent circuit of a dual-resonance vibration energy harvester.

for a vibration source that is dominated by one frequency. From Section 3.3.2 we know that a dual-resonant harvester can be created by attaching a LC tank to the output of the energy harvester as shown in Figure 7-1. The usable output power P_L is the power delivered to the load resistance R_L was shown in Equation 3.56 and repeated here:

$$P_L = \frac{\frac{1}{2}G_p^2 R_L |V_F|^2}{(\frac{1}{\omega C_K} - \omega L_M - G_p^2 X_L)^2 + (R_B + G_p^2 R_L)^2} \tag{7.3}$$

Recalling from the optimal matching conditions given in Section 3.2 Equation 3.46 and 3.47, P_L is maximized when

$$X_L = \frac{1}{G_p^2}(\frac{1}{\omega C_k} - \omega L_M) \tag{7.4}$$

$$R_L = \frac{R_B}{G_p^2} \tag{7.5}$$

At this matching condition, the maximum power can be expressed as

$$P_L = \frac{|V_F|^2}{8R_B} \tag{7.6}$$

$$= \frac{M^2\omega^4|Y|^2}{8B} \tag{7.7}$$

From this expression, we understand that in order to extract the maximum amount

of power, we want the proof mass M to be as large as possible. The maximum proof mass is normally bounded by the physical design space on the vibration surface so a maximum value can be determined straight forward. The damping factor B on the other hand is inversely proportional to the quality factor. While it may seem desired to minimize B and hence maximizing the quality factor, this will make the bandwidth of the harvesting system too small and extremely difficult to match the resonant frequency of the harvester to the vibration frequency. An ideal quality factor range is around 10 to 100. Therefore, the values of L_M and R_B can be obtained by determining the maximum proof mass M and damping factor B through the following equations:

$$L_M \equiv M \cdot \frac{J_v}{J_i} \tag{7.8}$$

$$R_B \equiv B \cdot \frac{J_v}{J_i} \tag{7.9}$$

In addition, if we assume that the R_L is ideally matched, the coupling factor G_p is desired to be as large as possible and is determined by the harvester topology. Next, let us determine the values of the load inductor L_1 and capacitor C_1. From Equation 3.57, we know that the resonant frequencies ω_1 and ω_2 of a dual-resonant harvesting system are the roots of the following equation:

$$\omega^2 + \frac{G^2 X_L}{L_M} \cdot \omega - \frac{1}{L_M C_K} = 0 \tag{7.10}$$

where X_L is the equivalent impedance of L_1 and C_1 in parallel

$$X_L = \frac{L_1}{1 - \omega^2 L_1 C_1} \tag{7.11}$$

Substituting Equation 7.11 into Equation 7.10, we have three parameters C_K, L_1 and C_1 to tune in order to match the roots ω_1 and ω_2. In the process, it is desired to have L_1 as small as possible in order to make the power electronics design easier. After this entire design process, a first-pass value for all the design parameters of a dual-

resonant energy harvesting system as shown in Figure 7-1 can be determined. The complex load impedance $R_L + jX_L$ can then be synthesized using power electronics.

7.3 Future Improvements

In this thesis, the theory of impedance matching for multi-resonant energy harvesting is well developed. However, due to the limited amount of time, only two experiments were carried out to demonstrate the theory and the power electronics. A great amount of future improvements can be made in the power electronics in three directions.

First, a digital control algorithm for the power electronics is highly desired and necessary for the proposed architecture to be practical since the current control burns more power than the power extracted from the vibration source itself. The digital control also will allow dynamic tuning and easier reconfiguration when the vibration conditions change.

A second area that warrants improvement is the integration of the power stage. A custom chip would allow power FET and gate drive sizing optimization. Optimal switching techniques such as zero-voltage switching (ZVS) can also be implemented to improve efficiency. These circuit optimization will greatly decrease the amount of power loss suffered while using a PCB implementation.

Finally, the third area is an overall system expansion that allows the power electronics to be suitable for not only piezoelectric harvesters, but all energy conversion methods. In theory, the piezoelectric harvester has the toughest power electronics to implement due to its large parasitic capacitance, but electromagnetic harvesters also bring challenges such as low output voltage levels and small output impedances. These design challenges also need to be addressed if the same power electronics is to be applied to other energy harvesting methods.

7.4 Final Words

It's been a long and fruitful journey exploring the area of energy harvesting in the past five and a half years. The journey started out with a crazy challenge of building a harvester on a moth to a more fundamental research of harvester impedance matching theory and power electronics implementation. I feel truly blessed to have the opportunity to work on both electromagnetic and piezoelectric harvesters and also their interfacing power electronics. While many problems have been solved and better understood, vibration energy harvesting is still looking for its break-out application. Nonetheless, the theory developed in this thesis outlined the fundamental limits of multi-frequency vibration energy harvesting and the power electronics architecture provides a possible solution for future designers to synthesize complex impedances and build multi-resonant energy harvesters.

Appendix A

Code Scripts

A.1 Harvester Impedance Matching

The harvester impedance matching code, used in Section 3.3, is implemented in MATLAB and shown in the following. This code calculates both the real and reactive power of the harvester and also the harvestser internal impedance. The first subsection gives the code for single resonant frequency shifting impedance matching and the following two subsections give the code for dual and triple resonant frequency impedance matching.

A.1.1 Single Resonance Tuning

```
% Single Resonance Tuning 05/20/2013

clear all
close all
load SPICE_RLC_v1.mat

% ----------
% Parameters
% ----------

C = 1.7e-3;      % [F]
L = 2.2e-3;      % [H]
```

```
R = 73.7e-3;      % [Ohm]
G = 1.3e-3;       % [N/V]
V = 13.5e-3;      % [V]
Z_R = R/G^2;      % [Ohm] Internal Resistance
f = linspace(1,250,2501);    % [Hz]
w = 2*pi*f;       % [rad/s]
ZI_C = -1/14.4e-9./w;    % Capacitive Load
ZI_L = w*260;             % Inductive Load

% ----------
% Output Power
% ----------

Pout = 0.5*Z_R*G^2*V^2*w.^2 ./ ((1/C-w.^2*L).^2 + w.^2.*(R+G^2*Z_R)^2) * 1e6;
Pout_C = 0.5*Z_R*G^2*V^2*w.^2 ./ ((1/C-w.^2*L-w.*ZI_C*G^2).^2 + w.^2.*(R+G^2*Z_R)↩
    ^2) * 1e6;
Pout_L = 0.5*Z_R*G^2*V^2*w.^2 ./ ((1/C-w.^2*L-w.*ZI_L*G^2).^2 + w.^2.*(R+G^2*Z_R)↩
    ^2) * 1e6;
Pout_XL = 0.5.*ZI_L.*G^2*V^2.*w.^2 ./ ((1/C-w.^2*L-w.*ZI_L*G^2).^2 + w.^2.*(R+G^2*↩
    Z_R)^2) * 1e6;
Pout_XC = 0.5.*ZI_C.*G^2*V^2.*w.^2 ./ ((1/C-w.^2*L-w.*ZI_C*G^2).^2 + w.^2.*(R+G^2*↩
    Z_R)^2) * 1e6;

SPICE_Pout = SPICE(:,2)*1e6;
SPICE_Pout_C = SPICE(:,3)*1e6;
SPICE_Pout_L = SPICE(:,4)*1e6;


subplot(3,1,1)
plot(f,Pout,'b','Linewidth',3)
grid on
ylabel('Real Power  [uW]','Fontsize',22,'fontweight','b')
set(gca,'FontSize',18,'FontWeight','bold','LineWidth',2,'XLim',[50 125],'YLim',[0 ↩
    350]);
axis square

subplot(3,1,2)
plot(f,Pout_C,'m','Linewidth',3)
grid on
hold on
plot(f,Pout_L,'r','Linewidth',3)
ylabel('Real Power  [uW]','Fontsize',22,'fontweight','b')
set(gca,'FontSize',18,'FontWeight','bold','LineWidth',2,'XLim',[50 125],'YLim',[0 ↩
    350]);
axis square
```

```
subplot(3,1,3)
plot(f,Pout_XL,'r','Linewidth',3)
grid on
hold on
plot(f,Pout_XC,'m','Linewidth',3)
xlabel('Frequency  [Hz]','Fontsize',22,'fontweight','b')
ylabel('Reactive Power  [uV-A]','Fontsize',22,'fontweight','b')
set(gca,'FontSize',18,'FontWeight','bold','LineWidth',2,'XLim',[50 125],'YLim'↩
    ,[-1200 1200]);
axis square
```

A.1.2 Dual-resonance Tuning

```
% Dual Resonance Tuning 05/20/2013

clear all
close all

% ----------
% PZT Constants
% ----------

Cm = 1.7e-3;          % [F]
Lm = 2.2e-3;          % [H]
Rm = 73.7e-3;         % [Ohm]      Internal Resistance
G = 1.3e-3;           % [N/V]
V = 13.5e-3;          % [V]
ZR = Rm/G^2;          % [Ohm]      Effective Real Impedance
f = linspace(1,300,3001);      % [Hz]
w = 2*pi*f;           % [rad/s]

% ----------
% Load Parameters
% ----------

L1 = 500;             % [H]    Load Inductor
C1 = 45e-10;          % [F]    Load Capacitance

% ----------
% Calculation
% ----------

ZI = (w*L1) ./ (1-w.*w*L1*C1);                                          ↩
    % [Ohm] Effective Imaginary Impedance
P = (0.5*ZR*G^2*V^2) ./ ((1./w/Cm-w*Lm-G*G*ZI).^2 + (Rm+G^2*ZR)^2) * 1e6;   ↩
    % [uW] Output Power
P_XL = (0.5*ZI*G^2*V^2) ./ ((1./w/Cm-w*Lm-G*G*ZI).^2 + (Rm+G^2*ZR)^2) * 1e6;  ↩
    % [uW] Output Power


% ----
% Plot
% ----
```

```
figure(1)
subplot(3,1,1)
plot(f,P,'b','Linewidth',3)
grid on
ylabel('Real Power  [uW]','Fontsize',22,'fontweight','b')
set(gca,'FontSize',18,'FontWeight','bold','LineWidth',2,'XLim',[0 200],'YLim',[0 ↩
    350]);
axis square

subplot(3,1,2)
plot(f,1./w/Cm-w*Lm,'b','Linewidth',3)
grid on
hold on
plot(f,G*G*ZI,'r','Linewidth',3)
ylabel('Impedance  [{\Omega}]','Fontsize',22,'fontweight','b')
hleg1 = legend('1/(\omega{C_{K}})-\omega{L_{M}}','{G^{2}}{X_{L}}');
set(hleg1,'Location','SouthWest','Fontsize',16)
set(gca,'FontSize',18,'FontWeight','bold','LineWidth',2,'XLim',[0 200],'YLim',[-10 ↩
    10]);
axis square

subplot(3,1,3)
plot(f,P_XL,'b','Linewidth',3)
grid on
xlabel('Frequency  [Hz]','Fontsize',22,'fontweight','b')
ylabel('Reactive Power  [uV-A]','Fontsize',22,'fontweight','b')
set(gca,'FontSize',18,'FontWeight','bold','LineWidth',2,'XLim',[0 200]);
axis square
```

A.1.3 Triple-resonance Tuning

```
% Triple Resonance Tuning 05/20/2013

clear all
close all

load Tripleharmonic_SPICE.mat
Tripleharmonic_SPICE_f = Tripleharmonic_SPICE(:,1);
Tripleharmonic_SPICE_P = Tripleharmonic_SPICE(:,2);

% ---------------
% PZT Constants
% ---------------

Cm = 1.7e-3;          % [F]
Lm = 2.2e-3;          % [H]
Rm = 73.7e-3;         % [Ohm]      Internal Resistance
G = 1.3e-3;           % [N/V]
V = 13.5e-3;          % [V]
ZR = Rm/G^2;          % [Ohm]      Effective Real Impedance
f = linspace(1,300,3001);      % [Hz]
w = 2*pi*f;           % [rad/s]

% ------------------
% Load Parameters
% ------------------

L1 = 500;             % [H]    Load Inductor
C1 = 45e-10;          % [F]    Load Capacitance
L2 = 250;             % [H]    Load Inductor
C2 = 30e-10;          % [F]    Load Capacitance

% ------------
% Calculation
% ------------

ZI = (w*L1) ./ (1-w.*w*L1*C1) + (w*L2) ./ (1-w.*w*L2*C2);      % [Ohm] Effective ↩
    Imaginary Impedance
P = (0.5*ZR*G^2*V^2) ./ ((1./w/Cm-w*Lm-G*G*ZI).^2 + (Rm+G^2*ZR)^2) * 1e6;      % [uW↩
    ] Output Power
P_XL = (0.5*ZI*G^2*V^2) ./ ((1./w/Cm-w*Lm-G*G*ZI).^2 + (Rm+G^2*ZR)^2) * 1e6;      % ↩
    [uW] Output Power
```

```
% ----
% Plot
% ----

figure(1)
subplot(3,1,1)
plot(f,P,'b','Linewidth',3)
grid on
ylabel('Real Power  [uW]','Fontsize',22,'fontweight','b')
set(gca,'FontSize',18,'FontWeight','bold','LineWidth',2,'XLim',[0 250],'YLim',[0 ↩
    350]);
axis square

subplot(3,1,2)
plot(f,1./w/Cm-w*Lm,'b','Linewidth',3)
grid on
hold on
plot(f,G*G*ZI,'r','Linewidth',3)
ylabel('Impedance  [{\Omega}]','Fontsize',22,'fontweight','b')
hleg1 = legend('1/(\omega{C_{K}})-\omega{L_{M}}','{G^{2}}{X_{L}}');
set(hleg1,'Location','SouthWest','Fontsize',16)
set(gca,'FontSize',18,'FontWeight','bold','LineWidth',2,'XLim',[0 250],'YLim',[-10 ↩
    10]);
axis square

subplot(3,1,3)
plot(f,P_XL,'b','Linewidth',3)
grid on
xlabel('Frequency  [Hz]','Fontsize',22,'fontweight','b')
ylabel('Reactive Power  [uV-A]','Fontsize',22,'fontweight','b')
set(gca,'FontSize',18,'FontWeight','bold','LineWidth',2,'XLim',[0 250],'YLim'↩
    ,[-12500 5000]);
axis square
```

A.2 Harvester Characterization

The harvester characterization code, used in Section 5.2.2, is implemented in MATLAB and shown in the following. It takes in the experimental results and the SPICE simulation results of the equivalent circuit model. This code also computes the output power with the spring-mass-damper model under the Model Equations section.

```
% ------------------------------
% PZT RC Model Matching - Voc
% ------------------------------

clear all
close all
load Vout_Open_Mass.mat
load LTSpice_PZT_2.mat

f = data(:,1);
fmax = max(f);
fmin = min(f);
fmodel = fmin : 0.1 : fmax;
w = 2*pi*fmodel;
voc_exp = data(:,2)/2*1000;     % Convert p-p to amplitude

fspice = LTSpice(:,1);
voc_spice = LTSpice(:,2)*1000;


% ----------------
% Experiment Data
% ----------------
fn = 81.2;          % [Hz]      Resonant Frequency
wn = 2*pi*fn;       % [rad/s]   Resonant Frequency
Q = 14;             %           Quality Factor
A = 0.7*9.8;        % [m/s^2]   Acceleration


% ----------------
% PZT Parameters
% ----------------
m = 2.2e-3;         % [kg]      Effective Mass
G = 1.3e-3;         % [N/V]     Coupling Factor
Cp = 130e-9;        % [F]       Capacitance
```

```
Rp = 1e6;              % [Ohm]      Parallel Resistance
k = wn^2*m;            % [N/m]       Spring Constant
B = m*wn/Q;            % [N*s/m]     Damping Factor


% ----------------
% Model Equation
% ----------------
voc_mod = A.*G./Cp./sqrt(((wn^2-w.^2)+G^2/Cp/m+wn/Q/Rp/Cp).^2+(w.*wn./Q-(wn^2-w.^2)↩
    ./w./Rp./Cp).^2)*1000;


% ----
% Plot
% ----
plot(f,voc_exp,'o','MarkerSize',10,'MarkerEdgeColor','b','LineWidth',3)
xlabel('Frequency   [Hz]','fontsize',22,'fontweight','bold')
ylabel('V_{oc}   [mV]','fontsize',22,'fontweight','bold')
set(gca,'FontSize',18,'FontWeight','bold','LineWidth',2);
axis square
grid on
hold on
plot(fmodel,voc_mod,'linewidth',3,'color','r')
plot(fspice,voc_spice,'s','MarkerSize',10,'MarkerEdgeColor','y','LineWidth',3)
legend('Experiment','MATLAB Model','SPICE Model')
% title('PZT Modeling - Open Circuit Voltage','FontSize',22,'FontWeight','bold')
```

Bibliography

[1] S. Roundy, P. Wright, and J. Rabaey, "A study of low level vibrations as a power source for wireless sensor nodes," *Computer Communications*, vol. 26, no. 11, pp. 1131 – 1144, 2003.

[2] R. Amirtharajah and A. Chandrakasan, "Self-powered signal processing using vibration-based power generation," *IEEE J. Solid-State Circuits*, vol. 33, no. 5, pp. 687 695, may. 1998.

[3] S. Chang, F. Yaul, A. Dominguez-Garcia, D. Otten, and J. Lang, "Harvesting energy from moth vibrations during flight," in *Proc. PowerMEMS 2009*, Dec. 2009.

[4] B. Yen and J. Lang, "A variable-capacitance vibration-to-electric energy harvester," *Circuits and Systems I: Regular Papers, IEEE Transactions on*, vol. 53, no. 2, pp. 288 – 295, feb. 2006.

[5] D. Zhu, M. Tudor, and S. P. Beeby, "Strategies for increasing the operating frequency range of vibration energy harvesters: a review," *Meas. Sci. Technol.*, vol. 21, no. 2, p. 022001, 2010.

[6] T. Kataoka, K. Mizumachi, and S. Miyairi, "A pulsewidth controlled ac-to-dc converter to improve power factor and waveform of ac line current," *Industry Applications, IEEE Transactions on*, vol. IA-15, no. 6, pp. 670–675, 1979.

[7] Y. Ramadass and A. Chandrakasan, "An efficient piezoelectric energy harvesting interface circuit using a bias-flip rectifier and shared inductor," *IEEE J. Solid-State Circuits*, vol. 45, no. 1, pp. 189 –204, 2010.

[8] R. Xia, C. Farm, W. Choi, and S.-G. Kim, "Self-powered wireless sensor system using mems piezoelectric micro power generator," in *Sensors, 2006. 5th IEEE Conference on*, oct. 2006, pp. 6 –9.

[9] D. Arnold, "Review of microscale magnetic power generation," *IEEE Trans. Magn.*, vol. 43, no. 11, pp. 3940 –3951, 2007.

[10] S. Beeby, R. Torah, M. Tudor, P. Glynne-Jones, T. O'Donnell, C. Saha, and S. Roy, "A micro electromagnetic generator for vibration energy harvesting," *J. Michromech. and Microeng.*, vol. 17, no. 7, p. 1257, 2007.

[11] F. Khan, F. Sassani, and B. Stoeber, "Copper foil-type vibration-based electromagnetic energy harvester," *Journal of Micromechanics and Microengineering*, vol. 20, no. 12, p. 125006, 2010.

[12] J. Kymissis, C. Kendall, J. Paradiso, and N. Gershenfeld, "Parasitic power harvesting in shoes," in *Proc. Symp. Wearable Comp.*, Oct. 1998, pp. 132 –139.

[13] Y. Jeon, R. Sood, J. h. Jeong, and S.-G. Kim, "Mems power generator with transverse mode thin film pzt," *Sens. Actuators A, Phys.*, vol. 122, no. 1, pp. 16 – 22, 2005.

[14] S. Anton and H. Sodano, "A review of power harvesting using piezoelectric materials," *Smart Mater. Struct.*, vol. 16, no. 3, p. R1, 2007.

[15] S. Roundy, P. Wright, and K. Pister, "Micro-electrostatic vibration-to-electricity converters," *Proc. IMECE*, vol. 2002, no. 36428, pp. 487–496, 2002.

[16] Y. Suzuki, D. Miki, M. Edamoto, and M. Honzumi, "A mems electret generator with electrostatic levitation for vibration-driven energy-harvesting applications," *J. Michromech. and Microeng.*, vol. 20, no. 10, p. 104002, 2010.

[17] A. Cammarano, S. Burrow, D. Barton, A. Carrella, and L. Clare, "Tuning a resonant energy harvester using a generalized electrical load," *Smart Mater. Struct.*, vol. 19, no. 5, p. 055003, 2010.

[18] S. Chang, M. Ocalan, J. Pabon, and J. Lang, "Harvesting energy from multi-frequency vibrations with a tunable electrical load," in *Proc. PowerMEMS 2012*, Dec. 2012.

[19] M. F. Schlecht and B. A. Miwa, "Active power factor correction for switching power supplies," *Power Electronics, IEEE Transactions on*, vol. PE-2, no. 4, pp. 273 - 281, oct. 1987.

[20] T. Toh, P. Mitcheson, L. Dussud, S. Wright, and A. Holmes, "Electronic resonant frequency tuning of a marine energy harvester," in *Proc. PowerMEMS 2011*, Nov. 2011.

[21] H. Kloub, D. Hoffmann, B. Folkmer, and Y. Manoli, "A micro capacitive vibration energy harvester for low power electronics," *PowerMEMS 2009*, pp. 165 168, December 2009.

[22] T. Sterken, K. Baert, R. Puers, G. Borghs, and R. Mertens, "A new power mems component with variable capacitance," in *Mircoelectronics Symposium and Exhibition*, Kohala Coast, HI, USA, Feb. 2003, pp. 27–34.

[23] C. Williams and R. Yates, "Analysis of a micro-electric generator for microsystems," *Sens. Actuators A, Phys.*, vol. 52, no. 1-3, pp. 8 – 11, 1996.

[24] J. Gieras, J.-H. Oh, M. Huzmezan, and H. Sane, "Electromechanical energy harvesting system," *Patent Publication*, 2007.

[25] X. Wu, J. Lin, S. Kato, K. Zhang, T. Ren, and L. Liu, "A frequency adjustable vibration energy harvester," in *Proc. PowerMEMS 2008 + microEMS2008*, Nov. 2008.

[26] G. Piazza, R. Abdolvand, G. Ho, and F. Ayazi, "Voltage-tunable piezoelectrically-transduced single-crystal silicon micromechanical resonators," *Sens. Actuators A, Phys.*, vol. 111, no. 1, pp. 71 – 78, 2004.

[27] D. Scheibner, J. Mehner, D. Reuter, U. Kotarsky, T. Gessner, and W. Dtzel, "Characterization and self-test of electrostatically tunable resonators for frequency selective vibration measurements," *Sens. Actuators A, Phys.*, vol. 111, no. 1, pp. 93 – 99, 2004.

[28] K. Lee, L. Lin, and Y.-H. Cho, "A closed-form approach for frequency tunable comb resonators with curved finger contour," *Sens. Actuators A, Phys.*, vol. 141, no. 2, pp. 523 529, 2008.

[29] C. Peters, D. Maurath, S. Wolfram, and M. Yiannos, "Novel electrically tunable mechanical resonator for energy harvesting," in *Proc. PowerMEMS 2008 + microEMS2008*, Nov. 2008.

[30] V. Challa, M. Prasad, Y. Shi, and F. Fisher, "A vibration energy harvesting device with bidirectional resonance frequency tunability," *Smart Mater. Struct.*, vol. 17, no. 1, p. 015035, 2008.

[31] T. Remtema and L. Lin, "Active frequency tuning for micro resonators by localized thermal stressing effects," *Sens. Actuators A, Phys.*, vol. 91, no. 3, pp. 326 – 332, 2001.

[32] R. Syms, "Electrothermal frequency tuning of folded and coupled vibrating micromechanical resonators," *J. Microelectromech. Syst.*, vol. 7, no. 2, pp. 164 –171, Jun. 1998.

[33] W.-J. Wu, Y.-Y. Chen, B.-S. Lee, J.-J. He, and Y.-T. Peng, "Tunable resonant frequency power harvesting devices," in *Proc. SPIE*, vol. 6169, 2006, pp. 55 –62.

[34] S. Shahruz, "Design of mechanical band-pass filters for energy scavenging," *J. Sound and Vib.*, vol. 292, no. 3-5, pp. 987 – 998, 2006.

[35] M. Ferrari, V. Ferrari, M. Guizzetti, D. Marioli, and A. Taroni, "Piezoelectric multifrequency energy converter for power harvesting in autonomous microsystems," *Sens. Actuators A, Phys.*, vol. 142, no. 1, pp. 329 – 335, 2008.

[36] H. Xue, Y. Hu, and Q.-M. Wang, "Broadband piezoelectric energy harvesting devices using multiple bimorphs with different operating frequencies," *IEEE Trans. Ultrason., Ferroelect., Freq. Contr.*, vol. 55, no. 9, pp. 2104 2108, 2008.

[37] M. Soliman, E. Abdel-Rahman, E. El-Saadany, and R. Mansour, "A wideband vibration-based energy harvester," *J. Michromech. and Microeng.*, vol. 18, no. 11, p. 115021, 2008.

[38] T. Petropoulos, E. Yeatman, and P. Mitcheson, "Mems coupled resonators for power generation and sensing," in *Micromechanics Europe*, Sept 2004.

[39] D. Spreemann, Y. Manoli, B. Folkmer, and D. Mintenbeck, "Non-resonant vibration conversion," *J. Michromech. and Microeng.*, vol. 16, no. 9, p. S169, 2006.

[40] S. Burrow, L. Clare, A. Carrella, and D. Barton, "Vibration energy harvesters with non-linear compliance," in *Proc. SPIE*, 2008.

[41] A. Hajati, S. Bathurst, H. Lee, and S. Kim, "Design and fabrication of a nonlinear resonator for ultra wide-bandwidth energy harvesting applications," in *Micro Electro Mechanical Systems (MEMS), 2011 IEEE 24th International Conference on*, jan. 2011, pp. 1301 –1304.

[42] T. Galchev, E. Aktakka, H. Kim, and K. Najafi, "A piezoelectric frequency-increased power generator for scavenging low-frequency ambient vibration," in *Micro Electro Mechanical Systems (MEMS), 2010 IEEE 23rd International Conference on*, jan. 2010, pp. 1203 –1206.

[43] R. Ramlan, M. Brennan, B. Mace, and I. Kovacic, "Potential benefits of a non-linear stiffness in an energy harvesting device," *Nonlinear Dyn.*, vol. 59, pp. 545–558, 2010, 10.1007/s11071-009-9561-5.

[44] H. Sodano, D. Inman, and G. Park, "Generation and storage of electricity from power harvesting devices," *J. Intell. Mater. Syst. Struct.*, vol. 16, no. 1, pp. 67 –75, Jan. 2005.

[45] E. Halvorsen, L. Blystad, S. Husa, and E. Westby, "Simulation of electromechanical systems driven by large random vibrations," in *Proc. MEMSTECH*, May 2007, pp. 117–122.

[46] E. Halvorsen, "Energy harvesters driven by broadband random vibrations," *J. Microelectromech. Syst.*, vol. 17, no. 5, pp. 1061 1071, oct. 2008.

[47] L. Tvedt, D. S. Nguyen, and E. Halvorsen, "Nonlinear behavior of an electrostatic energy harvester under wide- and narrowband excitation," *J. Microelectromech. Syst.*, vol. 19, no. 2, pp. 305 –316, 2010.

[48] Y. Ramadass and A. Chandrakasan, "A battery-less thermoelectric energy harvesting interface circuit with 35 mv startup voltage," *IEEE J. Solid-State Circuits*, vol. 46, no. 1, pp. 333 –341, 2011.

[49] E. Carlson, K. Strunz, and B. Otis, "A 20 mv input boost converter with efficient digital control for thermoelectric energy harvesting," *IEEE J. Solid-State Circuits*, vol. 45, no. 4, pp. 741 –750, 2010.

[50] L. Pinna, R. Dahiya, and M. Valle, "Spice model for piezoelectric bender generators," in *Electronics, Circuits, and Systems, 2009. ICECS 2009. 16th IEEE International Conference on*, dec. 2009, pp. 587 –590.

[51] I. Cassidy and J. Scruggs, "Statistically linearized optimal control of an electromagnetic vibratory energy harvester," *Smart Materials and Structures*, vol. 21, no. 8, p. 085003, 2012.